ABSTRACT

Title of Dissertation:	UNCOVERING THE MOLECULAR BASIS OF ACTIVITY-DEPENDENT RETINOFUGAL SYNAPSE PLASTICITY
	Chenghang Zhang, Doctor of Philosophy, 2023
Dissertation directed by:	Assistant Professor Colenso M. Speer, Department of Biology

Activity-dependent synapse plasticity is important for the establishment of neuron wiring in the central nervous system, particularly in the context of sensory processing. In the visual system, image-forming and non-image-forming retinal input into the brain is a popular model for studying activity-dependent plasticity due to the well-characterized neural activity and bulk-level innervation pattern. However, investigation of synaptic connection during early development has been impeded by the limited resolution of conventional fluorescent microscopy or lack of profile tagging in electron microscopy (EM) images. To overcome these challenges, we employed volumetric STochastic Optical Reconstruction Microscopy, immunohistochemistry synaptic protein labeling, and anterograde retinal tract tracing to investigate the activity-dependent retinogeniculate and retinohypothalamic synapse plasticity. Through our findings, we uncover the developmental pattern of retinofugal innervation and shed light on the impact of spontaneous activity on retinal synapse maturation at the synaptic level.

During the first postnatal week in mice, the dorsal lateral geniculate nucleus (dLGN) initially receives overlapping input from the two eyes before the binocular innervation segregated. The changes in individual synapse properties during the eye-specific segregation process have remained unknown. In Chapter 2, we uncovered eye-specific differences in presynaptic vesicle pool size and vesicle association with the active zone at the earliest stages of retinogeniculate refinement but found no evidence of eye-specific differences in subsynaptic domain number, size, or transsynaptic alignment across development. Genetic disruption of spontaneous retinal activity decreased retinogeniculate synapse density, delayed the emergence of eye-specific differences in vesicle organization, and disrupted subsynaptic domain maturation. These results suggest that activity-dependent eye-specific presynaptic maturation underlies synaptic competition in the mammalian visual system.

The dLGN relays visual information from the retina to the visual cortex through parallel processing pathways. In adult mice, such processing is achieved through spatial clustering of several retinal ganglion cells (RGCs) boutons to integrate convergent or divergent visual information. It is unknown whether such RGC synapse clustering occurs during the early developmental stage. In Chapter 3, we identified a subset of complex retinogeniculate synapses with larger presynaptic vesicle pools and multiple AZs that simultaneously promote the clustering of like-eye synapses (synaptic stabilization) and prevent synapse formation from the opposite eye (synaptic punishment). In mutant mice with disrupted spontaneous retinal wave activity, complex synapses are formed but fail to drive eye-specific synaptic clustering and punishment. These results reveal the early formation of a unique synaptic subset that regulates activity-dependent eye-specific synaptic competition and may serve as substrates for later synapse clustering formation.

A subset of RGCs that express the photopigment melanopsin (OPN4) innervate the suprachiasmatic nucleus (SCN), which serves as the central pacemaker responsible for controlling circadian rhythm in mammals. The function of OPN4 is important for SCN photoentrainment, but its impact on retinal synapse maturation during early development is unknown. In Chapter 4, we found that OPN4 plays an important role in retinal synapse formation and activation in the SCN during the early developmental stage. Loss of OPN4 leads to reduced retinal synapse density, and increased variability in the ratio of synapses with few or no docking vesicles, but has not effect on total vesicle pool volume. Meanwhile, the subsequent maturation of retinohypothalamic tract (RHT) synapses after the first postnatal week shows diminished reliance on OPN4 function and further compensates for the early defects in the absence of OPN4. This study reveals a moderate influence of OPN4 on early RHT synapse development and sheds light on the role of photopigment in regulating SCN synapse plasticity.

This dissertation introduces a novel approach using super-resolution fluorescent imaging in the thalamus and hypothalamus tissue. Our work has yielded insights into the activity-dependent maturation in synapse properties and spatial distribution in the dLGN, as well as the impact of OPN4 on retinohypothalamic synapses in the SCN. By revealing the synapse development at the molecular level, our study demonstrates presynaptic mechanisms that underlie activity-dependent retinal synapse plasticity during the early developmental stage. Furthermore, our application of super-resolution fluorescent microscopy highlights its potential as a valuable tool for future in situ studies on brain development.

UNCOVERING THE MOLECULAR BASIS OF ACTIVITY-DEPENDENT RETINOFUGAL SYNAPSE PLASTICITY

by

Chenghang Zhang

Dissertation submitted to the Faculty of the Graduate School of the
University of Maryland, College Park, in partial fulfillment
of the requirements for the degree of
Doctor of Philosophy
2023

Advisory Committee:
Assistant Professor Colenso M. Speer, Chair
Professor Joshua H. Singer
Associate Professor Daniel A. Butts
Professor Pamela A. Abshire
Associate Professor Jason W. Triplett

© Copyright by
Chenghang Zhang
2023

Acknowledgments

I would like to express my appreciation to Dr. Colenso Speer, my advisor, for his dedication and invaluable guidance throughout my study and research over the past years. From patiently teaching me basic tissue dissection to showing me the mindset and passion for scientific research, Colenso has consistently demonstrated his generosity in sharing his time and intelligence, for which I am truly grateful for his ongoing support. I am also deeply grateful to all my lab mates, whose expertise and assistance have significantly contributed to my laboratory work and daily experiences. Furthermore, I would like to thank my Advisory Committee and the dedicated faculty and staff from the biophysics and neuroscience programs at UMD. Their continuous support and guidance have played a pivotal role in my academic journey.

Lastly, I would like to express my deepest gratitude to my parents and my girlfriend (now fiancé), Meng Wang, for their unwavering love and encouragement throughout my life journey. Their sacrifices and understanding have allowed me to focus on my studies and pursue my academic aspirations with determination.

Throughout the process of constructing this acknowledgment, I have realized that my willingness to express my gratitude to those who have supported me is strongly hindered by my English writing ability… Nonetheless, I hope this humble expression of thanks reveals my sincere appreciation for each individual who has played a part in my academic journey.

Table of Contents

Acknowledgements ii
Table of Contents iii
List of Figures v
Chapter 1: Introduction: mechanism underlying activity-dependent retinofugal synapse plasticity 1
Section 1: Local signaling regulates dLGN synapse plasticity 1
Section 2: Activity-dependent synapse clustering during dLGN development 5
Section 3: Activity-dependent presynaptic plasticity in dLGN 8
Section 4: Conclusion 11

Chapter 2: The synaptic basis of activity-dependent eye-specific competition 12

Section 1: Abstract 12
Section 2: Introduction 12
Section 3: Results 15
Subsection 1: Spontaneous retinal activity regulates eye-specific density 15
Subsection 2: Spontaneous retinal activity regulates eye-specific presynaptic vesicle organization 15
Subsection 3: Synapses with larger presynaptic vesicle pools are more abundant after eye-specific competition 21
Subsection 4: Subsynaptic domain development is independent of eye-of-origin 24
Section 4: Discussion 27
Subsection 1: Molecular mechanisms underlying eye-specific presynaptic vesicle pool maturation 28
Subsection 2: Changes in SSD organization during eye-specific segregation 30
Subsection 3: Relationship between synapse development and axon refinement 32
Section 5: Limitations of the study 34
Section 6: Acknowledgment 35
Section 7: Author contributions 36

Chapter 3: Eye-specific synaptic clustering through activity-dependent stabilization and punishment mechanisms in the developing visual system 37
Section 1 Abstract 37
Section 2 Introduction 37
Section 3 Results 40
Subsection 1 A unique set of complex synapses shows eye-specific differences during retinogeniculate segregation 40
Subsection 2 Complex synapses undergo eye-specific vesicle pool maturation 44
Subsection 3 Complex synapses are loci for synaptic clustering 46
Subsection 4 Complex synapses mediate distance-dependent synaptic stabilization and punishment underlying eye-specific competition 50
Section 4 Discussion 55
Section 5: Acknowledgment 61

Section 6: Author contributions 61

Chapter 4: The influence of melanopsin on retinohypothalamic synapse development in the suprachiasmatic nucleus 62
Section 1: Abstract 62
Section 2: Introduction 62
Section 3: Result 64
Subsection 1: Deletion of OPN4 results in reduced retinal synapse density in the SCN 64
Subsection 2: OPN4 KO has a limited effect on RHT synapse vesicle pool organization 66
Section 4: Discussion 67
Section 5: Author contributions 70

Chapter 5: Conclusion 71
Appendices A 75
Animals 75
Eye injections 76
Tissue collection 76
Immunohistochemistry 77
Postfixation, dehydration, and embedding in epoxy resin 78
Ultrasectioning 78
Imaging chamber preparation 79
Imaging setup 79
Automated image acquisition 80
Image processing 81
Cell body filter 82
Eye-specific synapse identification and quantification 82
VGluT2 population analysis 84
Analysis of vesicles associated with the AZ 84
SSD analysis based on voxel intensity distributions 85
SSD analysis based on single molecule localization distributions 86
Complex synapse identification and quantification 88
Statistical analysis 89

Appendices B 90
Bibliography 104

List of Figures

Figure 2.1 Spontaneous retinal activity regulates eye-specific synapse density 16
Figure 2.2 Spontaneous retinal activity regulates eye-specific presynaptic vesicle organization..... 19
Figure 2.3 Synapses with larger presynaptic vesicle pools are maintained after eye-specific competition 22
Figure 2.4 Subsynaptic domain maturation is independent of eye-of-origin 24
Figure 3.1 A unique set of complex synapses shows eye-specific differences during retinogeniculate segregation 42
Figure 3.2 Complex synapses undergo eye-specific vesicle pool maturation 45
Figure 3.3 Complex synapses are loci for synaptic clustering..... 48
Figure 3.4 Complex synapses mediate distance-dependent synaptic stabilization and punishment underlying eye-specific competition 52
Figure 4.1 Deletion of OPN4 results in reduced retinal synapse density in the SCN. 65
Figure 4.2 OPN4 KO has mild effect on RHT synapse vesicle pool organization..... 66
Figure 7.1 High efficiency eye-specific synapse labeling and normal dLGN cytoarchitectural development in β2KO mice, related to Figure 2.1 90
Figure 7.2 Developmental maturation of VGluT2 cluster signal intensity and within-shell VGluT2 properties during eye-specific competition, related to Figure 2.2 92
Figure 7.3 Identification of small versus large VGluT2 cluster populations during eye-specific segregation, related to Figure 2.3 94
Figure 7.4 Activity-dependent SSD development from localization-based analysis, related to Figure 2.4. 96
Figure 7.5 Eye-specific differences in simple synapse density in the first postnatal week, related to Figure 3.1..... 98
Figure 7.6 Complex synapses undergo eye-specific vesicle pool maturation, related to Figure 3.2 99
Figure 7.7 Complex synapses are loci for synaptic clustering, related to Figure 3.3 100
Figure 7.8 Complex synapses mediate distance-dependent synaptic stabilization and punishment underlying eye-specific competition, related to Figure 3.4 102

Chapter 1: Introduction: mechanism underlying activity-dependent retinofugal synapse plasticity

During development, the wiring of the visual circuitry in the brain relies on spontaneous retinal activity and visual experience. In the thalamus, the dorsal lateral geniculate nucleus (dLGN) initially receives overlapping inputs from both eyes, which are later refined into segregated regions. While it is known that this process of eye-specific segregation is driven by spontaneous retinal activity ("retinal waves"), the mechanisms underlying this refinement at the synaptic and molecular level remain poorly understood.

In the introduction chapter, we will examine previous studies on the impact of synchronized or asynchronized retinal activity on eye-specific axon development and synapse refinement through spatially constricted signaling pathways (section 1). We will also explore how local synapse modulation can lead to the spatial redistribution of retinogeniculate synapses and impact the convergence of retinal input onto dLGN relay neurons (section 2). Additionally, we will review the activity-dependent presynaptic mechanisms that affect individual synapse maturation and elimination (section 3).

Section 1: Local signaling regulates dLGN synapse plasticity

In mice, numerous experimental findings have demonstrated that pharmacological or genetic disruption of retinal waves results in failed eye-specific segregation in the dLGN, implying that spontaneous retinal activity during the first postnatal week is correlated with the refinement of eye-specific synapses (for review, see Kirkby et al., 2013).

Retinal waves cause synchronized firing of RGCs within the same eye and asynchronized input between eyes. Given this characteristic, it is natural to expect eye-specific plasticity to follow a

Hebbian rule, where "neurons that fire together, wire together". It indicates an instructive role of retinal waves in eye-specific synapse refinement (Arroyo & Feller, 2016). In the dLGN, a single relay neuron can initially receive input from both eyes and synapses from one eye can prevail over the other due to its stronger synchrony with surrounding RGCs. Synapses with synchronized input can be strengthened by spike-timing-dependent plasticity, where correlated inputs on postsynaptic neurons are more likely to win the competition (Feldman, 2012; Miller et al., 2000). Similarly, in vivo, electrophysiology recording in *Xenopus laevis* tadpole tectal neurons has demonstrated that repeated activation of synapse within a critical time window (20ms) before a spike leads to synapse potentiation (L. I. Zhang et al., 1998). Supporting this idea, optogenetic manipulation of retinal activity reveals that the relative timing of binocular input can solely regulate eye-specific domains during development (J. Zhang et al., 2012).

However, in the mouse, dLGN direct evidence of Hebbian plasticity is difficult to obtain due to challenges in manipulating retinal activity precisely or recording in dLGN relay neurons *in vivo* during early development. It has been suggested that retinal waves may play a permissive rather than instructive role in eye-specific plasticity and that other genetic or molecular cues are also important in guiding synapse refinement. Indeed, Hebbian plasticity only predicts a "winner takes all" outcome, which cannot explain some more complex experimental observations. In experiments where the glutamatergic vesicle release in a subset of ipsilateral-projecting RGCs is silenced, the ipsilateral region in dLGN remains normal in size but contralateral RGCs are not excluded from this region (Koch et al., 2011). Similarly, when a subset of ipsilateral-projecting RGCs are misrouted away to the contralateral dLGN, the remaining ipsilateral RGC axons occupy a smaller territory and fail to expel contralateral RGCs (Rebsam et al., 2009). These results suggest

that activity-dependent activation of molecular cues may also regulate eye-specific synapse development in the dLGN, following a non-Hebbian plasticity pattern.

Although direct observation of synapse maturation is lacking (see chapter 2), axon development may offer insight into the mechanisms of eye-specific refinement. In *Xenopus laevis* tadpoles, the occasionally misrouted retinotectal axons to the ipsilateral side provide an opportunity to have a single fiber asynchronized with surrounding axons. When visual stimulation in the ipsilateral eye is synchronized with the other eye, the misrouted axon has fewer but more stable branches. In contrast, asynchronized inputs up-regulate axon dynamics, leading to an expanded axon territory (Munz et al., 2014). Meanwhile, using in vivo imaging in zebrafish larvae, researchers have discovered that when axons are silenced, they are unable to inhibit the formation of highly dynamic filopodia or arrest the growth of established branches, resulting in a larger arbor territory (Fredj et al., 2010). These findings suggest that synchronized input leads to stronger synapses that halt the elongation of axon branches and stabilize the axon arbor, while asynchronous input causes more exploratory growth of axon branches and larger territories occupied by the axon arbor.

Disrupted axon branch expansion is also observed in mice. Knocking out the β2 subunit of the nicotinic acetylcholine receptor (β2KO) in mice leads to a failed eye-specific segregation due to partially disrupted correlation among RGC input (Rossi et al., 2001; C. Sun et al., 2008). Similar to tadpoles, axon imaging in β2KO mice shows larger territories occupied by a single RGC axon (Dhande et al., 2011). Interestingly, it is not the number of branching sites but the average length of branches that leads to a larger axon territory. This implies that disturbed correlation in retinal waves may result in fewer and weaker retinogeniculate synapses, causing elongated axon branches and intermixed ipsilateral and contralateral regions in dLGN. Chapter 2 in this dissertation bridges

the gap between abnormal retinal activity and enlarged axon arbor by demonstrating that β2KO mice have fewer retinogeniculate synapses and disrupted vesicle docking to the active zone.

Given that axon development is correlated with synaptic strength regulation, it remains unclear how synchronized or asynchronized inputs affect synapse formation and elimination. A subsequent investigation of Munz et al delves deeper into the development of RGC axons in response to stimulation from each eye (Rahman et al., 2020). They found that the loss of branches in the misrouted tadpole ipsilateral axon is induced by activation of either eye, while branch addition is induced exclusively by activation of the contralateral eye. This suggests that intra-eye synchronized firing, which leads to stronger synapses and stabilized axon arbors, also sends non-cell-autonomous signals to impact nearby axons and increases their exploratory growing dynamics.

One of the local non-cell-autonomous effects is the elimination of weaker synapses in the vicinity of strong synapses. The tyrosine kinase JAK2 is a possible candidate for this signal. In a study of the mouse cingulate cortex, it was found that activation of synapses can trigger the JAK2-STAT1 signaling pathway, leading to the elimination of nearby inactive synapses (Yasuda et al., 2021). Both JAK2 and STAT1 are required for this punishment signal. A similar phenomenon is observed in neuromuscular junctions, where active synaptic sites in proximity cause local suppression of neurotransmitter release and synapse elimination (Balice-Gordon & Lichtman, 1994).

In addition, synchronized input may facilitate the stabilization of nearby axons from the same eye through the cyclase AMP (cAMP) signal. Louail et al. investigated the role of cAMP by using electroporation to reduce the cAMP level in a few RGCs in one eye, which resulted in disrupted eye-specific segregation and reduced axon arbor area of cAMP intact axons from the same eye (Louail et al., 2020). It suggests that cAMP plays a crucial role in sending non-cell-autonomous

signals to co-stabilize nearby axons. Supporting this idea, previous studies have found that the expression of adenylyl cyclase 1 (AC1) and cAMP responsive element (CRE) peak in dLGN in the first postnatal week, both of which are required for normal eye-specific segregation (Pham et al., 2001; Ravary et al., 2003). Interestingly, the effect of reduced axon arbor area was not observed in cAMP-reduced RGCs themselves, indicating the involvement of multiple factors in regulating axon development during refinement.

Taken together, recent studies have shown that in addition to Hebbian plasticity, molecular signaling plays a crucial role in regulating eye-specific segregation. These signaling pathways are triggered by synchronized retinal activity and have a localized impact on nearby axonal development. In chapter 2 of this dissertation, we showed that the development of retinogeniculate synapses is indeed regulated by potentially strong synapses nearby, where synapses from the same eye are stabilized and clustered together, while synapses from different eyes get destabilized with lower spatial correlation.

Section 2: Activity-dependent synapse clustering during dLGN development

As spatially localized signals play an important role in regulating eye-specific synapse development, how does this mechanism relate to the function of the dLGN to relay visual information to the visual cortex? In adult dLGN, RGC inputs are found as bouton clustering where several RGC form spatially clustered terminals as glomerulus. Such RGC synapse clustering offers a structure basis of parallel visual information processing where relay neurons integrate convergent or divergent visual features from RGCs (Liang et al., 2018). Compared with simple synapses where a vesicle pool is associated with one AZ, clustered synapses can represent complex and fuzzy local arrangements (Morgan et al., 2016) with a notably larger vesicle pool size (Monavarfeshani et al., 2018).

Bouton clustering is a common feature well-studied in hippocampal and cortical neurons (for review, see Kastellakis & Poirazi, 2019). It is also observed in the visual system, including the hamster LGN (Ling et al., 1998) and the adult cat visual cortex, where ~80% of neurons have clustered bouton inputs, including both excitatory and inhibitory neurons (Binzegger et al., 2007). Bouton clustering provides a conducive environment for signal integration. Studies using electrophysiology recording have shown that burst synaptic input is more likely to activate sets of synapses that are spatially close to each other in hippocampal dendrites (Kleindienst et al., 2011). In cultured hippocampal neurons, clustered synapses tend to have homogeneous synapse weights (Lee et al., 2016). Model simulation for spatially clustered synapses has revealed that synapse clustering leads to higher storage capacity for memory (Poirazi & Mel, 2001). And supralinear responses from synapse clustering may act as coincidence detectors via the initiation of fast dendritic spikes or may detect asynchronized bursts (Kastellakis & Poirazi, 2019).

The initial formation of bouton clustering is activity-dependent. In hippocampal neurons, NMDA receptors can trigger ryanodine-sensitive calcium release, further activating biochemical signaling that spread locally to facilitate synaptic clustering (Lee et al., 2016). Also, NMDA receptors may activate MAPK signaling to drive dendrite stabilization and synapse clustering under patterned activity (Wu et al., 2001). In the retina, B6 and B7 bipolar cells (BCs) innervate #10 RGC, with B6 more likely to exhibit bouton clustering. Suppression of presynaptic activity disrupts the bouton clustering formation (Morgan et al., 2011). Moreover, synapse clustering may be due to selective synaptogenesis. During motor learning, new spines are formed near preexisting synaptic clusters with correlated activity associated with the task (Fu et al., 2012; Hedrick et al., 2022). The neural simulation also indicates that activity-dependent transformation from NMDA-only silent synapses

through AMPA insertion near mature spines is essential for the formation of synapse clustering (Poirazi & Mel, 2001).

In mouse dLGN, complex synapses with larger vesicle pool sizes, which share similarities with bouton clustering, were first observed at P14 (Monavarfeshani et al., 2018). It has been suggested that the adhesion molecule LRRTM1 is required in the development of these synapses. Interestingly, LRRTM1 is known to be associated with excitatory synaptic function in the dLGN and directly linked to AMPA receptors (AMPARs). These findings support that locally complex synapse formation after eye-opening may be closely correlated with AMPAR activation and the onset of glutamatergic retinal waves and visual experience (Hong et al., 2014). During this developmental stage, there is a reduction in the number of RGC inputs onto each relay neuron, and the AMPA/NMDA current ratio increases, indicating synaptic strengthening through the insertion of AMPARs into the synapses (C. Chen & Regehr, 2000). Interestingly, the genetic deletion of the AMPAR auxiliary subunit CKAMP44, which prevents AMPAR insertion, does not affect eye-specific segregation (Hetsch et al., 2022), suggesting that bouton clustering and eye-specific refinement may utilize different mechanisms for plasticity.

However, the lack of observed bouton clustering during the first postnatal week in dLGN may be due to the limited resolution in synapse identification (Bickford et al., 2010). Furthermore, the fact that disrupted retinal activity in later stages failed to maintain eye-specific segregation (Demas et al., 2006; Kerschensteiner, 2016; J. Zhang et al., 2012) suggests a shared molecular mechanism between early eye-specific and later dLGN refinement. In Chapter 3 of this dissertation, we reported the presence of complex synapses featuring one large vesicle pool associated with multiple AZs during the first postnatal week, indicating the existence of preliminary bouton clustering in the dLGN. These complex synapses stabilize simple synapses nearby from the same

eye. And the ability for complex synapses to form local synapse clustering shows eye-specific modulation, where co-stabilization of synapse clustering was found for complex synapses from the same eye and de-clustering for opposite eyes. This suggests that the complex synapses play an important role in eye-specific refinement and may serve as substrates for future RGC synapse clustering maturation.

Section 3: Activity-dependent presynaptic plasticity in dLGN

Various signaling pathways have been identified that participate in eye-specific refinement, and most involved molecular cues regulate synaptic plasticity through presynaptic signaling. In chapter 2 of this dissertation, we observed that disrupted retinogeniculate refinement in mutant mice is linked with abnormal vesicle docking to the AZs. Therefore, comprehending the presynaptic mechanisms of synapse plasticity is essential for understanding activity-dependent eye-specific plasticity.

AC1 is one of the key molecules involved in activity-dependent eye-specific refinement. In mouse dLGN, AC1 expression reaches its peak during the first postnatal week and is necessary for normal retinothalamic mapping. Studies have shown that knocking-out AC1 leads to reduced calcium-stimulated AC activity, enlargement of RGC axon arbors, and disrupted eye-specific segregation (Ravary et al., 2003). Research has reported that the AC/PKA signaling pathway can regulate synaptic vesicle mobility (Chenouard et al., 2020). In hippocampal neurons, the AC/PKA signaling pathway activator, forskolin, can mimic the vesicle recruitment near the AZ induced by long-term potentiation (LTP) (Rey et al., 2020). These suggest that AC1/PKA signaling pathway can influence eye-specific competition by modulating presynaptic protein organization. Interestingly, the AC1/PKA signaling pathway may affect vesicle docking through RIM proteins (Lu et al., 2006). RIM proteins are known to tether Ca^{2+} channels to presynaptic AZs. Deletion of RIM leads

to a decrease in presynaptic Ca^{2+} transients and defects in neurotransmitter release (Han et al., 2011). In cortical synapses, knocking-out subunits in RIM1 results in fewer vesicles and a greater average distance from vesicles to AZs (Lichter et al., 2022). In mouse dLGN, deletion of RIM1 causes segregation defects through reduced RGC presynaptic release probability and defects in axon refinement (Assali et al., 2017). Furthermore, studies on β2KO mice have suggested that the deficiency in eye-specific segregation observed in these mice was not worsened by additional knockout of AC1 (Dhande et al., 2012), suggesting that inadequate activation of AC1 in RGCs may underlie the failed refinement in β2KO mice. This can further impair RIM function, disrupting the recruitment of vesicles around the AZ, which is consistent with our findings in chapter 2 of this dissertation.

Eye-specific segregation is also regulated by serotonin (5-HT). A subset of ipsilateral-projecting RGCs (iRGCs) expresses 5-HT transporter (Sert or 5-HTT) and knocking out 5-HTT or disrupting 5-HT degradation results in defects in eye-specific segregation (Salichon et al., 2001; Upton et al., 1999). Intriguingly, 5-HTT knockout mice exhibit a dLGN phenotype similar to that of ET33::VGluT2 flox/flox mice (Koch et al., 2011), in which refinement of the ipsilateral patch seems to be normal at the bulk level, but the contralateral projections fail to retract from the ipsilateral region. These findings suggest that 5-HTT is involved in activity-dependent eye-specific segregation.

The 5-HT-1B receptor, which is expressed in RGCs and dLGN cells (Salichon et al., 2001; Upton et al., 1999), can inhibit glutamate release in the retinotectal pathway (Mooney et al., 1994). However, the molecular mechanism underlying this process in dLGN development is not yet known. In cultured cells, the function of AC1 is inhibited by activation of the 5-HT-1B receptor (Lin et al., 2002). It is possible that 5-HTT in iRGCs may internalize 5-HT and relieve the function

of the 5-HT-1B receptor (Assali et al., 2014; García-Frigola & Herrera, 2010), which further regulates AC1 function in cAMP production. Eventually, the 5-HTT expressed in iRGCs may cause different levels of cAMP in contralateral-projecting RGCs (cRGCs) and iRGCs. Given that cAMP mediates non-cell-autonomous co-stabilization signals in neighboring RGCs (Louail et al., 2020; also see section 1), 5-HT may act as an activator of such local signals. In other words, 5-HT internalization by 5-HTT may lead to a local reduction in 5-HT that can impact nearby axons regardless of their eye-of-origin. In ET33 VGluT2 flox/flox mice or 5-HTT KO mice, the failed pruning of cRGCs in the ipsilateral region might be caused by the loss of 5-HTT internalization function. The defective equivalent level of cAMP between iRGCs and cRGCs in the ipsilateral region of dLGN leads to co-stabilization and failed cRGC axon retraction. It should be noted that ET33::VGluT2 flox/flox mice still have functional 5-HTT, and the 5-HT-1B receptor is also expressed in relay neurons in dLGN. Therefore, the influence of 5-HTT on synaptic plasticity is likely dependent on neuronal activity.

Additionally, activation of the 5-HT-1B receptor has been found to stimulate the ERK signaling pathway (Lin et al., 2002), which in turn is linked to the activation of the cAMP-response element-binding protein (CREB). In the dLGN, CRE-mediated gene expression occurs transiently and reaches its peak at P4. Disruptions to CREB function lead to impaired eye-specific segregation (Pham et al., 2001). CREB function continues until a later age when visual experience triggers an increase in the protein level of CREB (Krahe et al., 2012). Neural activity can potentially regulate CREB levels through the function of L-type Ca channels (Dilger et al., 2015). However, additional evidence is needed to confirm whether the CRE/CREB signaling pathway is involved in the regulation of eye-specific plasticity by 5-HT.

The studies discussed above indicate that cAMP plays an important role as a secondary messenger in regulating eye-specific segregation. In addition to its function in dLGN, an increase in cAMP levels in the retina can lead to altered retinal wave activity, resulting in an enlarged territory occupied by that eye in the dLGN (Stellwagen & Shatz, 2002). However, despite the altered territory, the retinal input from both eyes still segregates. This phenotype differs from that observed in AC1 knockout mice (Nicol et al., 2006; Ravary et al., 2003), indicating that the impact of cAMP in retina waves affects binocular mapping in the dLGN through a different mechanism than AC1 (Fassier & Nicol, 2021). This idea is further supported by evidence that knocking out AC1 has no significant effect on retinal wave properties (Dhande et al., 2012).

Section 4: Conclusion

This chapter provides an overview of the current understanding of the molecular mechanisms involved in eye-specific segregation in the dLGN. Three key aspects are explored, including the impact of RGC activity on local axon development, early RGC bouton clustering, and presynaptic plasticity that underlies eye-specific refinement. These changes are influenced by shared molecular cues and are important for the co-stabilization of RGC axons. Also, early activity-dependent bouton clustering links presynaptic redistribution and eye-specific segregation, suggesting a complex molecular signaling system that affects different aspects of synaptic refinement. It would be of great interest to investigate how retinal activity precisely regulates various aspects of the complex molecular system to ultimately determine the final wiring patterns in the dLGN.

Chapter 2: The synaptic basis of activity-dependent eye-specific competition

This chapter is a reprint of our published manuscript "the synaptic basis of activity-dependent eye-specific competition" in Cell Reports, 2023 by Chenghang Zhang, Swapnil Yadav, and Colenso M. Speer (C. Zhang et al., 2023). Additional figures were added to the appendices as supplemental figures. The contribution of each author was listed in section 7.

Section 1: Abstract

Binocular vision requires proper developmental wiring of eye-specific inputs to the brain. In the thalamus, axons from the two eyes initially overlap in the dorsal lateral geniculate nucleus and undergo activity-dependent competition to segregate into target domains. Here we combined eye-specific tract tracing with volumetric super-resolution imaging to measure the nanoscale molecular reorganization of developing retinogeniculate eye-specific synapses in the mouse brain. We uncovered eye-specific differences in presynaptic vesicle pool size and vesicle association with the active zone at the earliest stages of retinogeniculate refinement, but found no evidence of eye-specific differences in subsynaptic domain number, size, or transsynaptic alignment across development. Genetic disruption of spontaneous retinal activity decreased retinogeniculate synapse density, delayed the emergence eye-specific differences in vesicle organization, and disrupted subsynaptic domain maturation. These results suggest that activity-dependent eye-specific presynaptic maturation underlies synaptic competition in the mammalian visual system.

Section 2: Introduction

The refinement of eye-specific projections to the dorsal lateral geniculate nucleus (dLGN) of the thalamus is a classic model system for investigating the role of spontaneous neural activity in synaptic competition during mammalian brain development (Guido, 2018; Kirkby et al., 2013;

Litvina & Chen, 2017; Shatz, 1990). In the mouse, retinal ganglion cell (RGC) axons from the left and right eyes innervate the dLGN and then segregate into eye-specific domains prior to eye-opening (Godement et al., 1984). Eye-specific segregation is regulated by cholinergic spontaneous activity in the eyes ("retinal waves") during the first postnatal week (Ackman & Crair, 2014; Arroyo & Feller, 2016) and pharmacological disruptions of retinal waves cause defects in eye-specific axon segregation (Blank et al., 2011; Cook et al., 1999; Failor et al., 2015; Huberman et al., 2002, 2003; Penn et al., 1998; Pfeiffenberger et al., 2005; Rebsam et al., 2009, 2012; Rossi et al., 2001; Shatz & Stryker, 1988; Speer et al., 2014; Stellwagen & Shatz, 2002). Similar activity-dependent defects have been shown following genetic deletion of the β2 subunit of the nicotinic acetylcholine receptor ($\beta2NAChR^{-/-}$) which disrupts cholinergic retinal waves and arrests eye-specific segregation (Dhande et al., 2011; Grubb et al., 2003; Muir-Robinson et al., 2002; Rossi et al., 2001; Stafford et al., 2009; C. Sun et al., 2008; H. P. Xu et al., 2015, 2016; H. ping Xu et al., 2011).

Activity-dependent anatomical defects in eye-specific refinement are routinely studied by imaging bulk-labeled RGC axons using anterograde tracers or fluorescent protein expression (Kirkby et al., 2013). Additionally, single axon labeling experiments demonstrate that axonal refinement proceeds by the addition of branches in the correct target termination zone together with the elimination of small side branches (Campbell & Shatz, 1992; Dhande et al., 2011; D. Sretavan & Shatz, 1984; D. W. Sretavan & Shatz, 1986a, 1986b, 1987). The results of these experiments have established our current understanding of activity-dependent binocular competition with little information regarding synaptic molecular development and remodeling. Direct analysis of eye-specific synaptic competition has been hindered by difficulties in identifying immature retinogeniculate synapses based on ultrastructural features in electron microscopy (EM) images

(Bickford et al., 2010). At the same time, the diffraction limit of conventional light microscopy precludes fluorescence imaging analysis of synaptic organization at the nanoscale (Sigal et al., 2015). Thus, although eye-specific segregation is a longstanding model system for exploring activity-dependent circuit refinement, the synaptic basis of eye-specific retinogeniculate competition is unknown.

To address this gap, we combined eye-specific anterograde tracing with volumetric super-resolution microscopy and pre/postsynaptic immunolabeling in situ to measure nanoscale structural properties of 82,892 retinogeniculate synapses during eye-specific competition in the first postnatal week in the mouse (P2-P8). To determine the impact of disrupted spontaneous retinal activity on eye-specific refinement, we compared normal development in wild-type (WT) mice with disrupted refinement in β2NAChR$^{-/-}$ transgenic mice (hereafter referred to as β2KO). During retinogeniculate development in WT animals, we measured early (P2-P4) eye-specific differences in the maturation of presynaptic vesicle pool size and association with the active zone (AZ) that were correlated with the future outcome of eye-specific competition. Compared to WT, β2KO mice showed no developmental changes in retinogeniculate synapse density and lacked early eye-specific differences in vesicle association with the AZ. In contrast to activity-dependent and eye-specific vesicle pool development, we found no evidence for eye-specific differences in the number of Bassoon or Homer1 subsynaptic domains (SSDs), SSD properties, or transsynaptic SSD alignment across all developmental ages (P2-P8) in either WT or β2KO mice.

Section 3: Results

Subsection 1: Spontaneous retinal activity regulates eye-specific density

To identify eye-specific synapses, we injected fluorescent anterograde tracer (cholera toxin subunit beta - Alexa Fluor 488, hereafter referred to as CTB) into the right eye and imaged both the contralateral and ipsilateral regions within the left dLGN before (P2), during (P4), and toward the close (P8) of eye-specific segregation (Figures 2.1A and 7.1A, also see chapter 2). We used a serial-section single-molecule localization imaging approach based on STochastic Optical Reconstruction Microscopy (STORM) to collect three-dimensional super-resolution fluorescence imaging volumes (~45K μm^3 each) from each dLGN sample (Figures 2.1B and 7.1A) (Vatan et al., 2021). To label retinogeniculate synapses, we immunostained tissue with antibodies against the presynaptic proteins vesicular glutamate transporter 2 (VGluT2, expressed in RGC terminals) (El-Danaf et al., 2015; Fujiyama et al., 2003; Hammer et al., 2014; Land et al., 2004) and Bassoon together with the postsynaptic protein Homer1 (Figure 2.1B).

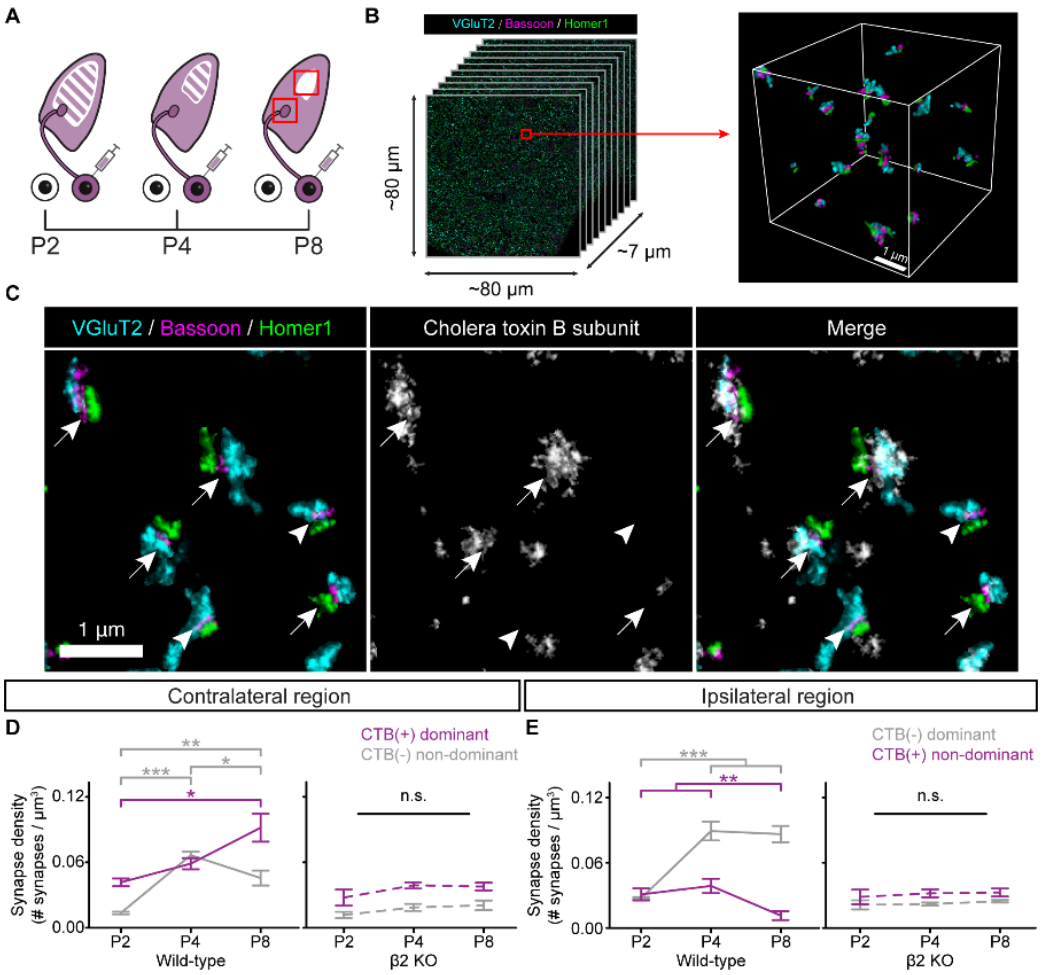


Figure 2.1 Spontaneous retinal activity regulates eye-specific synapse density

(A) Overview of the experimental design. CTB was injected to the right eye and eye-specific synapse development was imaged in two regions of interest (red boxes).

(B) Volumetric super-resolution imaging approach. Individual STORM image stacks (left panel) were ~45K µm^3 for each region of interest, genotype, and biological replicate (N=3 animals). Retinogeniculate synapses were identified in 3D volumetrically aligned image stacks (right panel shows a representative volume of ~104 µm^3 within a P8 contralateral ROI).

(C) Four color super-resolution images of eye-specific retinogeniculate synapses. Representative maximum-intensity Z-projection (700 nm) STORM images of synaptic proteins (left panel), CTB signals (middle panel), and merged (right panel) images from P8 WT dLGN in the contralateral ROI. Each imaging volume contained CTB(+) synapses from contralateral axons (arrows) and CTB(-) synapses from ipsilateral axons (arrowheads).

(D) Quantification of eye-specific synapse density in the contralateral ROI. Synapse development trajectories differ between CTB(+) dominant-eye (purple line, left panel) and CTB(-) non-dominant-eye projections (gray line, left panel). Overall synapse density is reduced in β2KO mice and there were no differences in eye-specific densities (dashed lines, right panel). Error bars reflect means ± SEM, N = 3 biological replicates. Statistical analysis was performed using a one-way ANOVA with a post-hoc Tukey's test: *P < 0.05, **P < 0.01, ***P < 0.001. Statistical comparisons over development for each eye-of-origin are shown in their corresponding colors (purple or gray). 'n.s.' indicates no significant differences were detected across developmental ages.

(E) Eye-specific synapse density in the ipsilateral ROI. Results are presented as in (D).

The 4-color (Bassoon, Homer1, VGluT2, and CTB) volumetrically aligned image stacks were thresholded and fluorescent signals in STORM images were identified as protein clusters based on size and signal density criteria (see Appendices A). Retinogeniculate synapses were then identified by the ordered relationship of VGluT2-Bassoon-Homer1 signals in 3D images (Figures 2.1, B and 2.1C). In this experimental design, CTB colocalization with presynaptic vesicle pools marked right-eye CTB(+) synapses while left-eye synapses were CTB(-) (Figure 2.1C). To confirm that anterograde tracing with CTB labels the majority of synapses from the injected eye, we performed control experiments using binocular CTB injections to label all retinogeniculate synapses and then quantified their association with CTB signals. At P2 the majority (~85%) of VGluT2(+) presynaptic clusters were CTB(+) following binocular injections and this further increased from P4 (~94%) to P8 (~98%) demonstrating high-efficiency CTB labeling of retinogeniculate synapses by anterograde tract tracing (Figure 7.1B).

Using monocular CTB injections to differentiate left versus right eye retinogeniculate synapses, we first quantified developmental changes in eye-specific synapse density within eye-specific territories (Figure 7.1A, also see chapter 2). We defined dominant- versus non-dominant-eye inputs based on eye-of-origin according to the pattern of adult wild-type contra/ipsilateral eye-specific projections. In the contralateral region of WT mice, the density of CTB(+) dominant-eye (contralateral) synapses increased progressively from P2-P8 (Figures 2.1D left panel and 7.1B). The density of CTB(-) non-dominant-eye (ipsilateral) synapses initially increased from P2 to P4 (Figures 2.1D left panel and 7.1B), consistent with delayed ipsilateral axon ingrowth (Godement et al., 1984). This was followed by significant synapse elimination that resulted in a ~31% reduction in CTB(-) synapse density from P4-P8 (Figures 2.1D left panel and 7.1B).

Within the ipsilateral region, the density of dominant CTB(-) ipsilateral-eye synapses also increased from P2-P4 and was stable from P4-P8 (Figures 2.1E left panel and 7.1B). In contrast, CTB(+) non-dominant contralateral-eye synapse density was stable from P2-P4 and decreased by ~72% at P8 (Figures 2.1E left panel and 7.1B). Compared to WT mice, synapse density from both eyes did not change across development in β2KO mice (Figures 2.1, D and E, right panels). To rule out the impact of the developmental expansion of the dLGN on synapse density measurements (El-Danaf et al., 2015; Grubb & Thompson, 2004), we quantified cell body density and neuropil fraction within each imaged region across ages/genotypes. We found no significant differences between WT and β2KO animals at any age (Figure 7.1C) indicating that the measured differences in synaptic densities reflect a failure of retinogeniculate synapse development in β2KO mice.

Subsection 2: Spontaneous retinal activity regulates eye-specific presynaptic vesicle organization

A previous electron microscopy study of retinogeniculate refinement in the cat found that nascent synapses formed by individual axons in the non-dominant eye-specific layer contained fewer vesicles compared to synapses formed in the future dominant-eye layer (Campbell & Shatz, 1992). To further investigate eye-specific and activity-dependent developmental differences in vesicle pool maturation, we quantified the size (volume) and protein enrichment (total signal intensity) of eye-specific VGluT2 clusters in both WT and β2KO mice from P2-P8 (Figures 2.2A and 7.2A). We focused our analysis on synaptic development within the contralateral ROI, which is reliably identified across all ages and genotypes (see Appendices A). In WT mice, presynaptic VGluT2 clusters from both eyes grew larger (Figure 2.2B) and contained more VGluT2 proteins (Figure 7.2A) over development. Across all ages, CTB(+) dominant-eye VGluT2 clusters were larger and contained more proteins than CTB(-) non-dominant-eye clusters (Figures 2.2B and 7.2A). In β2KO mice, dominant-eye VGluT2 cluster size also increased over development (Figures 2.2B and

7.2A). However, the magnitudes of eye-specific differences at P2 and P4 were reduced at each age compared with WT (Figures 2.2B and 7.2A). In WT mice, the median dominant-eye VGluT2 cluster volumes were 140% (P2) and 170% (P4) larger than non-dominant-eye VGluT2 clusters. In β2KO mice, the magnitudes of eye-specific differences in volumes were reduced to 97% (P2) and 73% (P4) (Figure 2.2B).

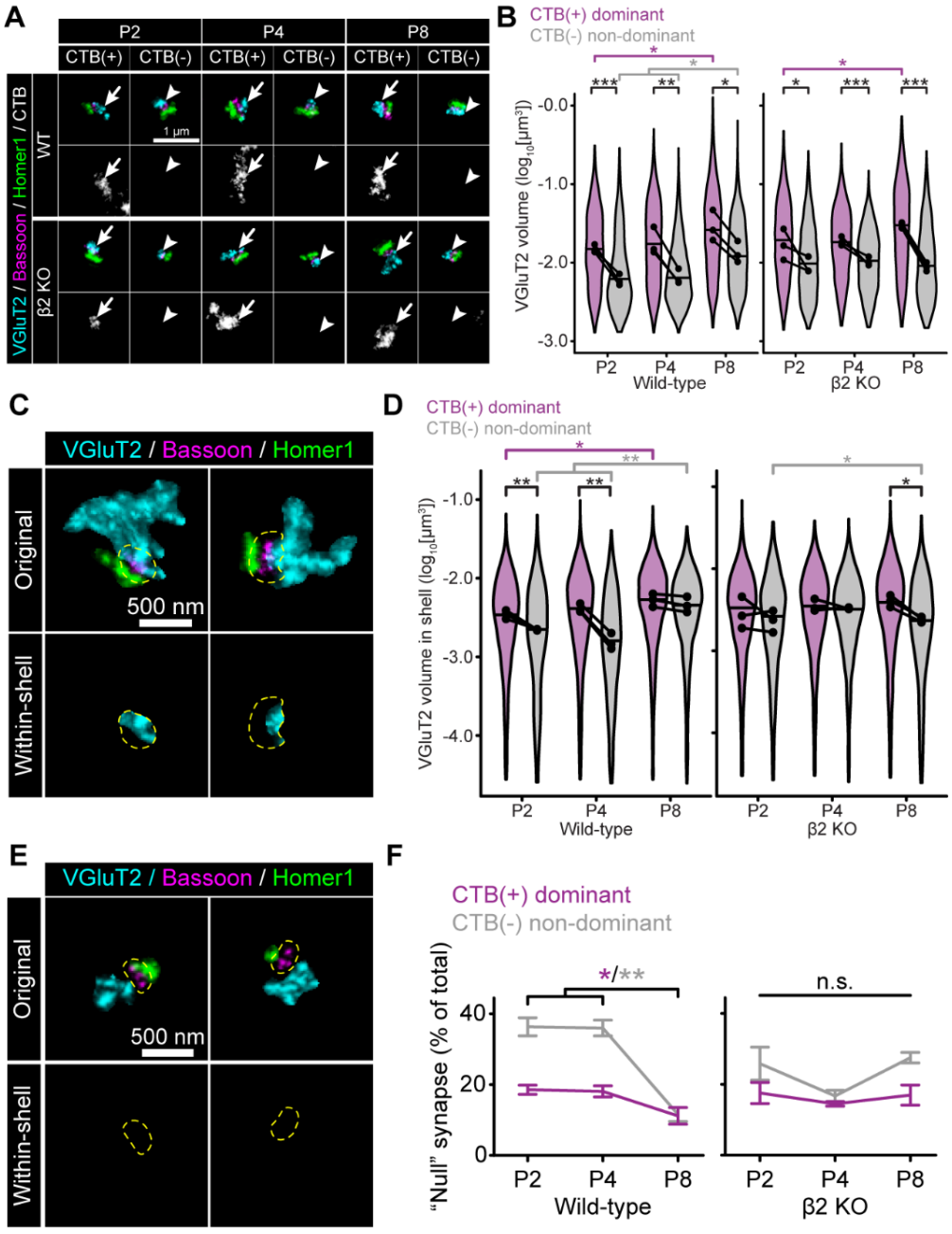


Figure 2.2 Spontaneous retinal activity regulates eye-specific presynaptic vesicle organization
(A) Representative CTB(+) (arrows) and CTB(-) (arrowheads) retinogeniculate synapses for each age and genotype. Each image is a maximum intensity Z-projection of 210-490 nm. For each age, synapses were selected based on the median value of the VGluT2 volume.
(B) Eye-specific developmental changes in VGluT2 cluster volume in WT (left panel) and β2KO mice (right panel). Violin plots show the full distribution of cluster volume from 3 biological replicates imaged in the contralateral ROI. Horizontal lines show the median values of the grouped data. Black dots reflect the individual median values for each biological replicate. Black lines between CTB(+) and CTB(-) populations represent data collected from the same biological replicate. Statistical analysis was performed using a mixed model ANOVA where the age or eye-of-origin was the fixed main factor and the biological replicate ID was a random nested factor. Pair-wise comparisons between ages were performed using a post-hoc Bonferroni's test. Black asterisks indicate statistical comparison between eye-specific CTB(+) and CTB(-) clusters. Purple asterisks indicate statistical comparisons between CTB(+) clusters across ages. Gray asterisks indicate statistical comparisons of CTB(-) clusters across ages. *$P < 0.05$, **$P < 0.01$, ***$P < 0.001$.
(C) Analysis of active-zone associated VGluT2 volume. VGluT2 signal was measured within a 48nm shell (dashed yellow line) surrounding presynaptic Bassoon clusters. Maximum-intensity Z-projection images (210-490 nm) show representative P8 WT synapses from the contralateral ROI.
(D) Eye-specific VGluT2 volume at the AZ in WT (left panel) and β2KO mice (right panel) across development. Violin plots show the grouped distribution of cluster volumes from 3 biological replicates imaged in the contralateral ROI. Horizontal lines show the median values of the grouped data. Black dots reflect the individual median values for each biological replicate. Black lines between CTB(+) and CTB(-) populations represent data collected from the same biological replicate sample. Statistical analysis was performed using a mixed model ANOVA where the age or eye-of-origin was the fixed main factor and the biological replicate ID was a random nested factor. Pair-wise comparisons between ages were performed using a post-hoc Bonferroni's test. Black asterisks indicate statistical comparison between eye-specific CTB(+) and CTB(-) clusters. Purple asterisks indicate statistical comparisons between CTB(+) clusters across ages. Gray asterisks indicate statistical comparisons between CTB(-) clusters across ages. *$P < 0.05$, **$P < 0.01$, ***$P < 0.001$.
(E) STORM images of "null" synapses with no AZ-associated vesicles. VGluT2 signal was measured within a 48nm shell (dashed yellow line) surrounding presynaptic Bassoon clusters. Maximum-intensity Z-projection images (210-490 nm) show representative P8 WT synapses from the contralateral ROI.
(F) The fraction of "null" synapses in WT (left panel) and β2KO mice (right panel) across development. Line graph showing the grouped distribution of "null" synapse fraction from 3 biological replicates imaged in the contralateral ROI. Error bars reflect means ± SEM. Statistical analysis was performed using a one-way ANOVA with a post-hoc Tukey's test. *$P < 0.05$, **$P < 0.01$. 'n.s.' indicates no significant differences were detected across developmental ages.

Because synaptic strength depends in part on the number of presynaptic release sites as well as docked vesicles (Kaeser & Regehr, 2017), we reasoned that eye-specific synapses may show differences in vesicle pool organization near the AZ. To test this, we measured VGluT2 signal volume and protein enrichment within a 48 nm shell surrounding each AZ Bassoon cluster to quantify vesicles associated with the AZ (Figure 2.2C; see Appendices A). Here again, we confined our analysis to the contralateral ROI and found that in WT mice, the volume and protein

enrichment of AZ-associated VGluT2 signal increased over development for both CTB(+) and CTB(-) synapses (Figures 2.2D and 7.2B). In WT mice from P2-P4, VGluT2 association with the AZ was significantly greater for dominant-eye inputs compared with non-dominant-eye synapses (Figures 2.2D and 7.2B). In contrast, β2KO mutants showed no early eye-specific differences in the VGluT2 signal near the AZ (Figures 2.2D and 7.2B). To rule out the possibility that the measured increase in AZ vesicle signal in WT animals was caused by differences in the Bassoon cluster area and corresponding shell volume, we normalized VGluT2 signals within the shell to the total shell volume. After normalization we again found early eye-specific differences in AZ-associated VGluT2 in WT, but not β2KO mice (Figures 7.2, C and D).

Interestingly, not all AZ Bassoon clusters contained VGluT2 signal within the shell region (Figure 2.2E). Such 'null' synapses with no AZ-associated vesicles may have reduced release probability or be functionally silent (Voronin & Cherubini, 2004). In WT mice at early stages of eye-specific synaptic refinement (P2-P4), projections from the CTB(-) non-dominant-eye showed a higher fraction of 'null' synapses compared to the CTB(+) dominant-eye projections (Figure 2.2F). This early bias in eye-specific competition was resolved by P8 when the fraction of 'null' synapses decreased and reached the same level for both CTB(+) and CTB(-) synaptic populations (Figure 2.2F). In contrast, β2KO mutants showed no differences in "null" synapse ratios across ages for either eye of origin (Figure 2.2F). Together, these results show that vesicle association with the presynaptic AZ is developmentally-regulated, activity-dependent, and eye-specific.

Subsection 3: Synapses with larger presynaptic vesicle pools are more abundant after eye-specific competition

The difference in presynaptic vesicle content between dominant-eye versus non-dominant-eye synapses (Figures 2.2, A and B) suggests that vesicle pool size could be essential for synaptic

refinement. To test this idea, we measured the presynaptic VGluT2 volume distribution across each age/genotype and found these were well-represented by a two-peak Gaussian function reflecting the presence of two distinct synaptic populations (small versus large) (Figures 7.3, A and B; R^2 >0.96 for all fits). We conservatively defined VGluT2 clusters with volumes smaller than the lower peak as a "small" synapse population and those larger than the upper peak as a "large" synapse population (Figure 7.3B). The synapse classification was consistent across ages/genotypes (Figure 7.3C) and large/small eye-specific VGluT2 clusters were morphologically similar across all conditions (Figure 2.3A).

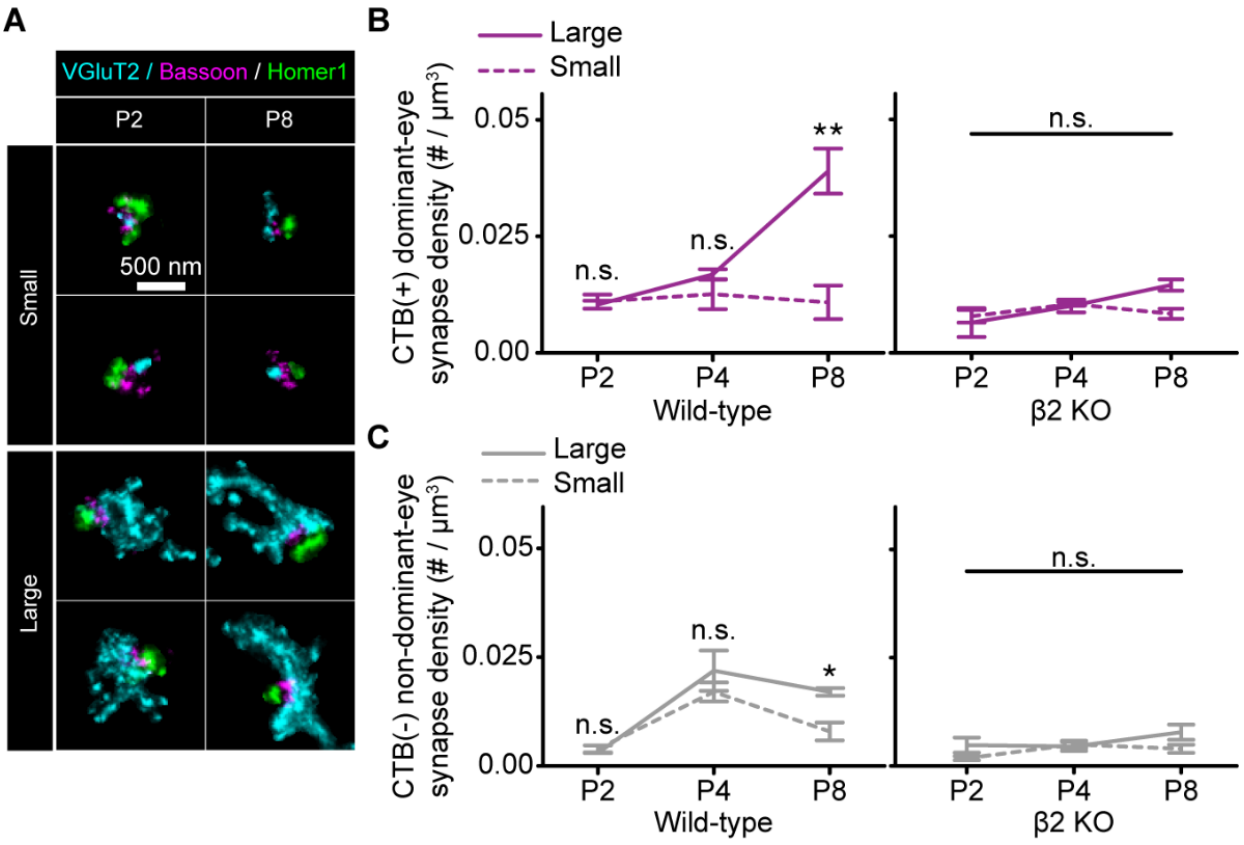


Figure 2.3 Synapses with larger presynaptic vesicle pools are maintained after eye-specific competition

(A) Representative small (top panels) and large (bottom panels) retinogeniculate synapses from WT mice at P2 (left panels) and P8 (right panels). Maximum-intensity Z-projection images (210-490 nm) show synapses from the contralateral ROI.

(B) Changes in large versus small synapse density from the CTB(+) dominant-eye during development. The line graphs show the density of large (solid purple lines) and small (dashed purple lines) synapses in WT (left panel) and β2KO mice (right panel) measured within the contralateral ROI. Error bars reflect means ± SEM from N = 3 biological replicates. Statistical analysis was performed using a one-way ANOVA. *P < 0.05, **P < 0.01., 'n.s.' indicates no significant differences were found between large and small synapses.

(C) Changes in large versus small synapse density from the CTB(-) non-dominant-eye during development. The line graphs show the density of large (solid gray lines) and small (dashed gray lines) synapses in WT (left panel) and β2KO mice (right panel) measured within the contralateral ROI. Error bars reflect means ± SEM from N = 3 biological replicates. Statistical analysis was performed using a one-way ANOVA. *P < 0.05, **P < 0.01. 'n.s.' indicates no significant differences were found between large and small synapses.

Comparing the synapse density of the two populations in WT mice (Figures 2.3B and 2.3C, left panels), we found that the overall increase in VGluT2 cluster volume in CTB(+) dominant-eye synapses (Figure 2.2B) reflected an increase in the density of large synapses while the density of small synapses did not change from P2 to P8 (Figure 2.3B, left panel). Consistent with the increase in ipsilateral-eye synapse density at P4 (Figures 2.1D and 7.1B), the density of both large and small CTB(-) non-dominant-eye synapses increased from P2-P4 (Figure 2.3C, left panel). Subsequently from P4-P8, the density of both large and small CTB(-) non-dominant-eye synapses decreased, but the loss of small synapses was more significant (~50% decrease) compared with larger synapses (~17% decrease) (Figure 2.3C, left panel). We found no developmental changes in the density of large versus small synapses of either eye of origin in β2KO mutants (Figures 2.3, B and C), demonstrating an activity-dependent failure of presynaptic vesicle pool maturation underlying eye-specific competition.

Subsection 4: Subsynaptic domain development is independent of eye-of-origin

Super-resolution imaging enables the detection of subsynaptic domains (SSDs) that coordinate the presynaptic release with postsynaptic receptors during neurotransmission (H. Chen et al., 2018; Tang et al., 2016). To investigate whether SSDs in retinogeniculate synapses show developmental or eye-specific differences, we identified pre/postsynaptic SSDs based on voxel intensity distributions in 3D-aligned STORM images (Figure 2.4A, "image-based analysis"). After separating SSDs by watershedding, we measured SSD properties within retinogeniculate Bassoon and Homer1 clusters in the contralateral ROI (see Appendices A).

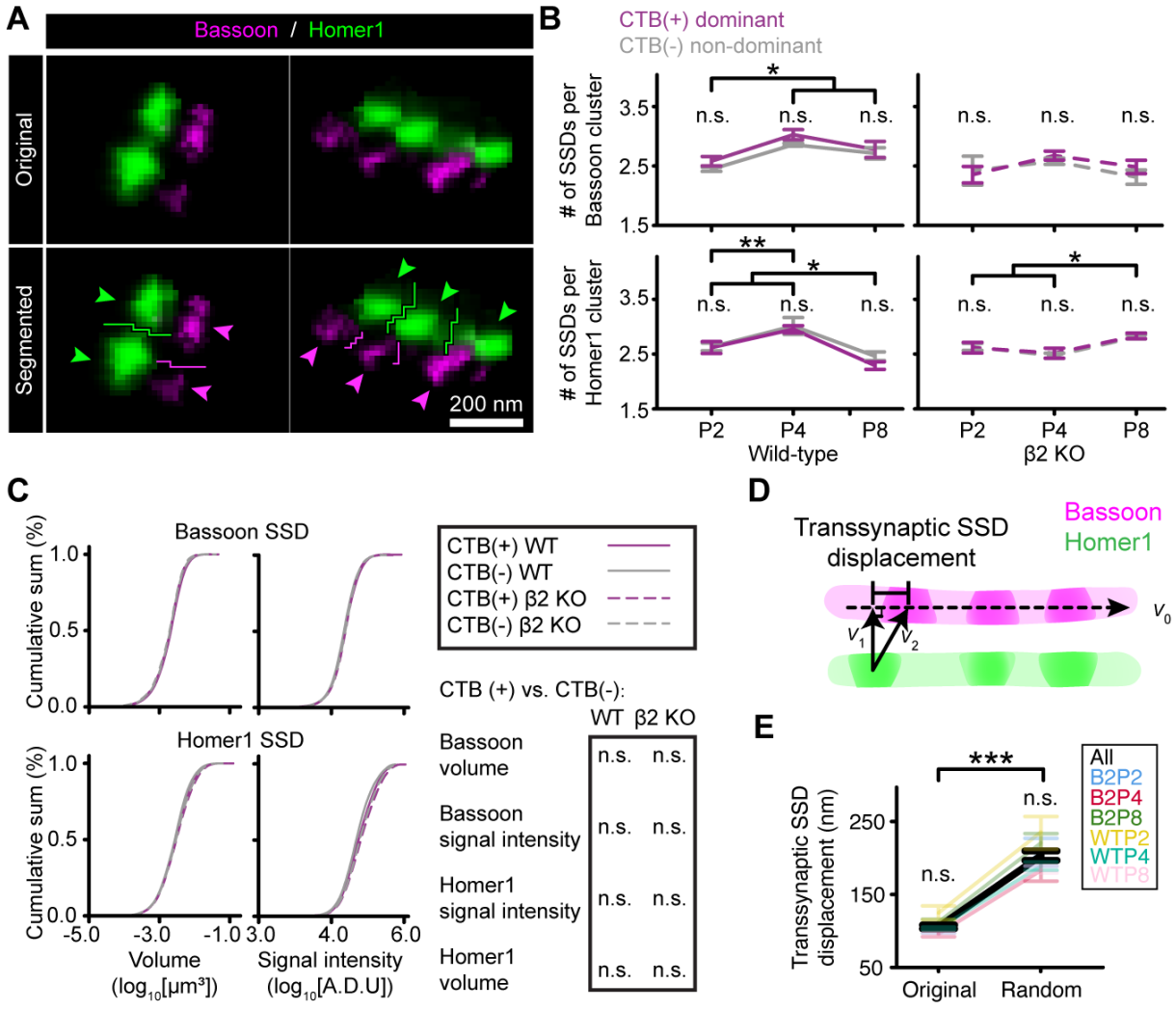


Figure 2.4 Subsynaptic domain maturation is independent of eye-of-origin
(A) Subsynaptic domain (SSD) identification in STORM images. From STORM images (top panels), Bassoon (purple arrowheads) and Homer1 (green arrowheads) SSDs were separated by watershedding at local image intensity minima (colored lines). Representative images show the middle section of each 3D cluster from a P8 WT sample in the contralateral ROI.
(B) Changes in synaptic SSD number during development. Line graphs show the change in SSD number in Bassoon (top panels) and Homer1 (bottom) panels in WT (left panels) and β2KO mice (right panels) mice over development. Purple lines reflect CTB(+) dominant-eye synapses while gray lines reflect CTB(-) non-dominant-eye synapses. Error bars show means ± SEM from N = 3 biological replicates. Statistical analysis was performed using a one-way ANOVA with a post-hoc Tukey's test. *P < 0.05, **P < 0.01. 'n.s.' = not significant.
(C) No eye-specific differences in SSD properties during retinogeniculate segregation. Cumulative histograms show SSD volume (left panels) and signal intensity (right panels) for all Bassoon (top panels) and Homer1 (bottom panels) clusters. Each histogram shows grouped data for all synapses across development (P2/P4/P8; N=3 biological replicates for each age). Statistical analysis was performed using a mixed model ANOVA where the eye-of-origin was the fixed main factor and the biological replicate ID was a random nested factor. A summary of statistical comparisons between CTB(+) and CTB(-) clusters for both WT and β2KO mice (bottom right) shows no significant differences. 'n.s.' = not significant.
(D) Illustration of transsynaptic SSD displacement measurement. The cartoon shows paired Bassoon (magenta) and Homer1 (green) SSDs (darker colored regions) within a synapse (lighter colored background). For the analysis of each individual SSD pair, v_0 is a vector through the principal plane of the Bassoon cluster. v_1 is a vector perpendicular to v_0. v_2 is a vector that runs from the centroid of the Homer1 SSD to the centroid of the nearest Bassoon SSD within the synapse. After aligning the tails of v_1 and v_2 to the same origin, the transsynaptic SSD displacement was calculated by measuring the distance between the intersections of v_1 and v_2 with v_0.
(E) No changes in transsynaptic SSD displacement across ages and genotypes. Colored lines show mean transsynaptic SSD displacement from 3 biological replicates for each age and genotype (data are grouped from both eyes, which showed no eye-specific differences). The black line shows grouped data of all ages and genotypes for both eyes. Error bars reflect means ± SEM. Statistical analysis was performed using a one-way ANOVA. 'n.s.' indicates no significant differences between genotypes, ages, or eye-of-origin within original and randomized measurements. '***' indicates a significant difference in displacement comparing original SSDs versus randomized data, P < 0.001.'n.s.' indicates no significant differences were detected across developmental ages and genotypes.

The average number of Bassoon or Homer1 SSDs per synapse was between 2-3 across our retinogeniculate synapse dataset (Figure 2.4B). The number of Bassoon SSDs in each synapse (Figure 2.4B, top panels) was largely consistent across development and showed no eye-specific differences in either WT or β2KO mice. Postsynaptically, the number of Homer1 SSDs per synapse decreased from P4-P8 in WT mice (Figure 2.4B, bottom left panel), while β2KO mice showed an opposite developmental pattern (Figure 2.4B, bottom right panel) indicating activity-dependent developmental changes in postsynaptic Homer1 distribution. However, similar to Bassoon SSDs, we found no eye-specific differences in the number of Homer1 SSDs per synapse

across ages and genotypes (Figure 2.4B, bottom panels). We next quantified the volume and signal intensity of Bassoon and Homer1 SSDs for all synapses in our dataset and found no developmental (data not shown) or eye-specific changes for either genotype (Figure 2.4C).

To further investigate SSD properties based on single molecule localization density information, we developed a machine-learning approach to reconstruct single molecule localization distributions from volumetrically aligned STORM images. We trained a convolutional neural network (CNN) model using unaligned 2D STORM images and the corresponding ground truth single molecule distributions (see Appendices A). The model was then applied to predict localization distributions from 3D-aligned STORM images and SSDs were identified using density-based spatial clustering of applications with noise (DBSCAN) analysis (Figure 7.4A). To evaluate the SSD detection accuracy within the CNN-predicted output, we compared the centroid positions of SSDs identified within ground truth 2D storm localization distributions versus their corresponding CNN-predictions (see Appendices A). We found short offsets between SSD centroid positions across the comparison (~21-29 nm) indicating that SSDs identified by the model were in good agreement with ground truth data (Figure 7.4B). Consistent with the image-based analysis, we found no eye-specific differences in SSD number (Figure 7.4C) or volume (Figure 7.4D) across ages or genotypes.

Pre/postsynaptic SSDs are aligned in "nanocolumns" that position presynaptic release sites close to postsynaptic receptors for efficient neurotransmission (Tang et al., 2016). Based on this arrangement, we reasoned that transsynaptic SSD alignment could be regulated as a mechanism for eye-specific refinement. To test this, we performed an alignment analysis to measure Bassoon and Homer1 SSD spatial relationships across our entire synaptic data set for all ages and genotypes. After determining the optimal parallel plane of pre/postsynaptic alignment, we measured the

displacement between SSD weighted centroid positions relative to a perpendicular vector across each synapse (Figure 2.4D; see chapter 2). The average SSD displacement (~100nm) was significantly smaller than the control measurements in which we randomized postsynaptic SSD positions within each individual synapse (Figure 2.4E). We found no significant differences in transsynaptic SSD alignment between age groups, genotype (Figure 2.4E), or eye-of-origin (data not shown), suggesting that transsynaptic SSD alignment is robust during activity-dependent synaptic refinement.

Section 4: Discussion

Previous work has shown significant defects in eye-specific axon refinement resulting from manipulations of spontaneous retinal activity. Such changes are expected to impact retinogeniculate microcircuit development, yet little is known about the synaptic basis of activity-dependent competition during eye-specific segregation. Here we used volumetric super-resolution imaging to measure the activity-dependent development of eye-specific synapses with molecular labeling information and subsynaptic image resolution. By analyzing tens of thousands of developing eye-specific synapses we found that 1) genetically disrupting spontaneous retinal activity causes a significant decrease in retinogeniculate synapse density underlying failed eye-specific refinement, 2) presynaptic vesicle pool maturation and subsynaptic association with the active zone (AZ) is activity-dependent and show eye-specific differences correlated with synaptic competition outcomes; 3) there are no eye-specific differences in the subsynaptic domain (SSD) organization of active zone (Bassoon) and postsynaptic density (Homer1) proteins during development; and 4) there are no developmental, eye-specific, or activity-dependent differences in transsynaptic SSD alignment in retinogeniculate synapses during eye-specific refinement.

Together, these results show that eye-specific presynaptic vesicle pool maturation underlies activity-dependent synaptic competition mechanisms in vivo.

Subsection 1: Molecular mechanisms underlying eye-specific presynaptic vesicle pool maturation

Our four-channel super-resolution images revealed significant developmental and activity-dependent differences in vesicle pool maturation and enrichment at the AZ that differentiated eye-of-origin in the developing dLGN (Figure 2.2). These findings are consistent with a previous ultrastructural study of prenatal retinogeniculate development in the cat in which more synaptic vesicles were found in dominant versus non-dominant eye-specific presynaptic terminals (Campbell & Shatz, 1992). A possible mechanism for eye-specific vesicle pool maturation is the induction of cyclic AMP/protein kinase A (cAMP-PKA) signaling by Ca^{2+}-dependent adenylyl cyclase (AC) activity (Fassier & Nicol, 2021). AC1 mutant mice (AC1 KO) show disrupted eye-specific retinogeniculate segregation (Nicol et al., 2006; Ravary et al., 2003) resulting from the enlargement of individual RGC arbors (Dhande et al., 2012). AC1 KO, β2KO, and AC1 KO :: β2KO double knockout mice show similar retinofugal refinement defects in the first postnatal week, suggesting an interaction between spontaneous retinal activity and presynaptic AC signaling (Dhande et al., 2012).

AC/PKA signaling regulates presynaptic release probability in part through the phosphorylation of presynaptic RIM1 proteins (Kohansal-Nodehi et al., 2016; Lu et al., 2006; Müller et al., 2022). RIM zinc finger domains are essential for docking vesicles adjacent to presynaptic Ca^{2+} channels (Tan et al., 2022) and genetic deletion of RIM1/2 causes eye-specific segregation defects in the dLGN (Assali et al., 2017). Similar results have been reported during somatosensory cortical development where thalamocortical synapses in AC1 mutants show defects in presynaptic RIM1

phosphorylation, reduced vesicle release, and abnormal barrel field formation (Lu et al., 2006; Suzuki et al., 2015). Because AC/PKA signaling has been shown to regulate synaptic vesicle mobility (Chenouard et al., 2020) and retention at the AZ (Rey et al., 2020), it will be of future interest to investigate eye-specific differences in vesicle pool organization in AC1 KO mutants.

In addition to reduced eye-specific vesicle pool maturation, β2KO mice fail to show an early eye-specific bias in vesicle occupancy at the AZ normally seen in WT mice (Figures 2.2, C-F). Vesicle number at the AZ is indicative of presynaptic release probability and early eye-specific differences in the presynaptic release may induce non-cell autonomous signaling mechanisms between ipsi- versus contralateral RGC axons (Assali et al., 2017; Fredj et al., 2010; Hua et al., 2005; Koch et al., 2011; Rahman et al., 2020; Yasuda et al., 2021; L. I. Zhang et al., 1998). Genetic deletion of presynaptic VGluT2 or RIM1/2 proteins within a subset of ipsilaterally-projecting retinal ganglion cells (RGCs) reduces their presynaptic release probability and prevents the retraction of contralateral fibers from the future ipsilateral termination zone (Assali et al., 2017; Koch et al., 2011). Presynaptic release from co-active inputs may activate synapse elimination signaling pathways (so-called "punishment signals") that cause the retraction of uncorrelated (non-dominant-eye) axons. Similar mechanisms have been implicated in synaptic competition between developing neuromuscular axons where a more active motor neuron synapse destabilizes weaker neighboring synapses (Balice-Gordon & Lichtman, 1994; Buffelli et al., 2003). In the visual system, JAK2 kinase signaling has been implicated as one such punishment signaling pathway and dominant-negative interference with JAK2 signaling in retinogeniculate axons allows non-dominant eye axons to evade competitive elimination (Yasuda et al., 2021). In addition to punishment signals that destabilize competing eye-specific axons, non-cell-autonomous mechanisms may also help to stabilize co-active inputs from the same eye. Downregulation of

cAMP signaling in a subset of RGC axons causes neighboring axons from the same eye to develop smaller terminal arbors than controls (Louail et al., 2020). This effect is independent of changes in retinal wave activity, suggesting that cAMP signaling mediates a non-cell-autonomous stabilization mechanism in developing retinogeniculate arbors from the same eye-of-origin.

In addition to biasing neurotransmission efficacy, eye-specific differences in presynaptic vesicle pool development may reflect the selective delivery or capture of proteins that regulate synapse formation versus pruning. Synaptogenesis requires the trafficking and recruitment of synaptic vesicle precursors and AZ proteins which coalesce along developing axons to form presynaptic terminals (Bury & Sabo, 2016; Guedes-Dias & Holzbaur, 2019; Rizalar et al., 2021). As synapses mature, they become more active and experience increased vesicle cycling, faster vesicle aging, and increased protein turnover that supports synaptic function (Denker et al., 2011; Jähne et al., 2021; Truckenbrodt et al., 2018). Eye-specific differences in the rate of vesicular release may impact the presentation of synaptic tagging molecules that regulate activity-dependent glial phagocytosis of developing synapses (Cong et al., 2020; Wilton et al., 2019). Future super-resolution imaging experiments will help to evaluate developmentally-regulated and eye-specific expression patterns of major histocompatibility complex (MHC) proteins (Datwani et al., 2009), complement factors (Schafer et al., 2012), and other immune signaling molecules with important roles in retinogeniculate development (Faust et al., 2021).

Subsection 2: Changes in SSD organization during eye-specific segregation

In contrast to early eye-specific differences in vesicle organization, we found no eye-specific differences in either active zone (Bassoon) or postsynaptic density (Homer1) SSD number, volume, or signal intensity. Similarly, we observed no eye-specific differences in the alignment of Bassoon and Homer1 SSDs across retinogeniculate synapses in both WT and β2KO mice.

Transsynaptic SSD alignment facilitates neurotransmission by bringing independent presynaptic release sites into apposition with receptors and associated PSD proteins (Tang et al., 2016). This architecture suggests that changes in SSD number or transsynaptic alignment could impact synaptic strength as a mechanism underlying synaptic competition (H. Chen et al., 2018). Our results, which are consistent with in vitro analysis showing activity-independent SSD alignment (S. Y. Sun et al., 2022), suggest that changes in transsynaptic SSD alignment or number do not underlie eye-specific synaptic competition in vivo.

While we found no evidence for eye-specific SSD differences, we did observe both developmental and activity-dependent changes in Homer1 SSD number in retinogeniculate synapses of both eyes. We found that the number of Homer1 SSDs was reduced from P2-P8 in WT mice while β2KO mice showed an opposite effect (Figures 4B and 7.4C, bottom panels). Homer1 has been shown to form a matrix at the PSD where it interacts with Shank to help stabilize AMPA and NMDA receptors (Hayashi et al., 2009). Developmental changes in Homer1 SSD organization may reflect PSD maturation that contributes to an increased AMPA/NMDA receptor ratio and the functional unsilencing of retinogeniculate synapses (Litvina & Chen, 2017). Consistent with this, functional recording experiments during eye-specific segregation in the superior colliculus (SC) have shown that WT retinocollicular synapses undergo progressive maturation that increases AMPA quantal amplitude, increases the AMPA/NMDA ratio, and decreases the fraction of silent synapses (Chandrasekaran et al., 2007; Furman et al., 2013; Furman & Crair, 2012; Shah & Crair, 2008). In contrast, β2KO mice show decreased AMPA quantal amplitude, reduced AMPA/NMDA ratio, an increased fraction of silent synapses, and more numerous synaptic connections compared with controls (Chandrasekaran et al., 2007; Shah & Crair, 2008).

In contrast to increased retinocollicular synapse density in β2KO mice (Chandrasekaran et al., 2007; Shah & Crair, 2008), we found that β2KO mice develop significantly fewer retinogeniculate synapses from both eyes compared to WT controls. Such regional differences in synaptic development could arise from the unique expression of different Ca^{2+} channel types in dLGN versus SC retinofugal terminals which may differentially impact presynaptic Ca^{2+} levels and related downstream signaling (Govindaiah et al., 2020). Region-specific differences in presynaptic AZ composition may also contribute as evidenced by the finding that genetic deletion of RIM1/2 proteins from RGC terminals disrupts eye-specific refinement in the dLGN with no impact on eye-specific segregation in the SC (Assali et al., 2017). Considering that the majority of retinal ganglion cells project to both the dLGN and SC (Ellis et al., 2016), it will be of interest to further characterize region-specific differences in the ultrastructural development of synaptic inputs from distinct RGC types (Kim et al., 2019). Additionally, future functional recording experiments during eye-specific segregation in the dLGN will be informative for comparison to previously published results in the SC.

Subsection 3: Relationship between synapse development and axon refinement

The activity-dependent defects we measured in eye-specific synaptogenesis and presynaptic terminal development offer further support for a synaptotropic hypothesis of neurite development in which the accumulation/stabilization of presynaptic proteins regulates the formation and stability of neurite branches (Vaughn, 1989). Live imaging of developing frog retinotectal axon dynamics has shown that vesicle accumulation over time stabilizes presynaptic terminals and local axon branching near synaptic sites (Ruthazer et al., 2006). Branch stabilization requires presynaptic release and experiments to genetically silence individual axons result in exuberant branching phenotypes (Fredj et al., 2010). In addition, targeted axon branching is regulated by

RGC activity following a Hebbian plasticity rule where correlated activity amongst neighboring RGCs stabilizes axon branches while uncorrelated activity increases axon branching dynamics (Munz et al., 2014; Ruthazer et al., 2003) through a non-cell-autonomous signal (Rahman et al., 2020).

In contrast to live imaging, static STORM images cannot resolve fast dynamics of synaptic turnover that may occur in the axons of both eyes during competition. However, STORM snapshots revealed developmental changes in eye-specific synapse density and presynaptic size which suggest the formation/maintenance of stable synapses in future eye-specific territories. Dominant-eye synapse density increased over development and was driven by an increase in synapses with larger presynaptic vesicle pools. In contrast, non-dominant eye synapse density decreased over development and smaller synapses were lost at a greater rate. Together, these results suggest that differences in eye-specific synapse stability underlie eye-specific branching patterns. Compared to WT, β2KO mice have disrupted cholinergic wave properties that reduce the precision of correlated RGC input to the dLGN (Stafford et al., 2009; C. Sun et al., 2008) and result in an enlargement of individual retinogeniculate axon arbors (Dhande et al., 2011). In this context, our finding that β2KO mice have significantly fewer synapses and disrupted presynaptic vesicle pool organization compared with WT is consistent with the hypothesis that synapse formation/stabilization is an important regulator of local axon branching. Future high-resolution imaging experiments combining synaptic and axonal labeling will be useful to explore relationships between synaptic turnover and neurite branching during retinogeniculate circuit development.

Section 5: Limitations of the study

The data presented in this study are snapshots of development taken from ROIs selected in the dLGN core for comparison across ages and genotypes. However, the rodent dLGN is known to exhibit regional differences in retinal input, particularly between core and shell domains, and these may undergo different patterns of synaptic refinement during development that were not captured in the current study (Kerschensteiner & Guido, 2017; Reese, 1988). Further, our synaptic images using CTB for eye-specific labeling do not provide information on the RGC type identities of individual retinogeniculate synapses. Because diverse RGC types converge to form synaptic glomeruli on individual relay neuron branches (Hammer et al., 2015; Liang et al., 2018; Morgan et al., 2016), it will be informative to use RGC type-specific transgenic labeling in future super-resolution studies to investigate the development of synaptic connections conveying unique visual representations to the brain.

The combination of single-molecule localization microscopy and sample ultrasectioning that we used to achieve volumetric STORM reconstructions requires technical skill and sacrifices imaging speed for increased spatial resolution (Vatan et al., 2021). However, because the sample preparation method is similar to serial-section electron microscopy, there is future potential to integrate super-resolution light and electron microscopy (EM) to achieve dense connectomic reconstructions together with molecular-specific information at individual synaptic connections and cellular contacts (De Boer et al., 2015; Heiligenstein & Lucas, 2022). Similar to EM, STORM images reveal static synaptic features. By comparing eye-specific synapses at different ages, we showed the association of specific subsynaptic properties (particularly vesicle organization) with the future outcome of eye-specific competition (Figures 2.2 and 2.3). A more complete understanding of how specific morphological features drive synaptic competition will require new

experiments with higher temporal resolution necessary to resolve dynamic changes in developing synapses in vivo.

We performed the current experiments using four spectrally-separate color channels, which limited our ability to interrogate a large number of known synaptic and signaling proteins with important roles in eye-specific segregation. In the future, multiplexed labeling approaches could help to increase the number of protein species imaged within individual samples and enable network analyses of synaptic remodeling during activity-dependent development (Minehart & Speer, 2021; Schueder et al., 2020). Finally, the spatial resolution of our approach is currently limited by a combination of the localization precision of the fluorophores used (~18-30 nm) (Dempsey et al., 2011), the labeling density and linkage error associated with indirect immunohistochemistry (~20 nm) (Lelek et al., 2021), and the physical thickness (Z-dimension) of our ultrathin sections (70 nm) (Vatan et al., 2021). Theoretical and technical advances that increase the spatial resolution of super-resolution microscopy (Dankovich & Rizzoli, 2021; Liu et al., 2022) will have immediate applications to the imaging of serial-section arrays, leading us closer to molecular scale analysis of synaptic protein assemblies in situ.

Section 6: Acknowledgment

The authors thank Dr. Michael C. Crair for generously sharing the β2KO mouse line used in this work. We also thank the statistical consulting program at the UMD Libraries for advice concerning statistical analyses. The research was funded by National Institutes of Health grant DP2MH125812 (CMS) and institutional startup support provided by the University of Maryland.

Section 7: Author contributions

Conceptualization: C.Z. and C.M.S.; Data Curation: C.Z., S.Y., and C.M.S.; Formal Analysis: C.Z., S.Y., and C.M.S.; Funding Acquisition: C.M.S.; Investigation: C.Z. and C.M.S.; Methodology: C.Z., S.Y., and C.M.S.; Project Administration: C.Z. and C.M.S.; Resources: C.Z. and C.M.S.; Software: C.Z., S.Y., and C.M.S.; Supervision: C.M.S.; Validation: C.Z. and C.M.S.; Visualization: C.Z. and C.M.S.; Writing – Original Draft Preparation: C.Z. and C.M.S.; Writing – Review & Editing: C.Z., S.Y., and C.M.S.

Chapter 3: Eye-specific synaptic clustering through activity-dependent stabilization and punishment mechanisms in the developing visual system

This chapter is a reprint of a manuscript in preparation for submission "Eye-specific synaptic clustering through activity-dependent stabilization and punishment mechanisms in the developing visual system" by Chenghang Zhang and Colenso M. Speer. Additional figures were added to the appendices as supplemental figures. The contribution of each author was listed in section 6.

Section 1 Abstract

Co-active synaptic connections are often spatially clustered to enable local dendritic computations underlying learning, memory, and basic sensory processing. In the mammalian visual system, retinal ganglion cell (RGC) axons converge to form clustered synaptic inputs for local signal integration in the dorsal lateral geniculate nucleus (dLGN) of the thalamus. Retinogeniculate synapse clustering is promoted by visual experience after eye-opening, but the earliest events in cluster formation and potential regulation by spontaneous retinal wave activity prior to visual experience are unknown. Here, using volumetric super-resolution single-molecule localization microscopy together with eye-specific labeling of developing retinogeniculate synapses in the mouse, we show that synaptic clustering is eye-specific and activity-dependent during the first postnatal week. We identified a subset of complex retinogeniculate synapses with larger presynaptic vesicle pools and multiple active zones that simultaneously promote the clustering of like-eye synapses (synaptic stabilization) and prohibit synapse clustering from the opposite eye (synaptic punishment). In mutant mice with disrupted spontaneous retinal wave activity, complex synapses form, but fail to drive eye-specific synaptic clustering and punishment seen in controls. These results highlight a role for spontaneous retinal activity in regulating eye-specific

stabilization and punishment signals contributing to synaptic clustering in circuits essential for visual perception and behavior.

Section 2 Introduction

A hallmark of neuronal computation is the formation of spatially clustered synaptic inputs to facilitate local computations within individual dendrites (Poirazi & Mel, 2001; Rall, 1962). Through linear and non-linear signal integration mechanisms, synaptic clusters play critical computational roles in learning, memory, and sensory processing underlying cognition and behavior (Kastellakis & Poirazi, 2019; Leighton & Lohmann, 2016; Mel et al., 2017; Winnubst & Lohmann, 2012). During circuit development, the formation of synaptic clusters is regulated by both spontaneous and sensory-driven neural activity that helps to stabilize or eliminate individual synapses to establish mature connectivity patterns (Kirchner & Gjorgjieva, 2022; Leighton & Lohmann, 2016; Winnubst & Lohmann, 2012).

A model example of activity-dependent synaptic cluster formation is the refinement of retinal inputs to the dorsal lateral geniculate nucleus (dLGN) of the thalamus (Bickford, 2019). Electron microscopy (EM) reconstructions of the mouse dLGN reveal the convergence of retinal ganglion cell (RGC) inputs to form “complex” synaptic clusters known as glomeruli (Bickford et al., 2010; Hammer et al., 2015; Monavarfeshani et al., 2018; Morgan et al., 2011). Each individual glomerulus contains multiple RGC axon terminal boutons formed onto a dendritic branch of a dLGN relay neuron. Individual bouton structures vary from small terminals with a single active zone (AZ) to large and/or perforated synapses containing multiple AZs (Bickford et al., 2010; Hammer et al., 2015; Monavarfeshani et al., 2018; Morgan et al., 2011). These ultrastructural observations are supported by additional experimental results from transsynaptic (Rompani et al., 2017) and Brainbow-based RGC labeling (Hammer et al., 2015; Monavarfeshani et al., 2018),

optogenetic stimulation of RGC axons (Bauer et al., 2021; Litvina & Chen, 2017), and calcium imaging of retinogeniculate boutons (Liang et al., 2018) confirming the clustering of RGC inputs to relay neuron dendrites in the dLGN. Because individual glomeruli often receive inputs from multiple RGCs encoding either similar or distinct visual features (Liang et al., 2018), the proper developmental wiring of RGC bouton clusters is critical for local dendritic integration functions that drive visual spike responses in the adult brain.

Previous studies have shown that synaptic cluster development in neural circuits depends upon spatiotemporally correlated synaptic activity that induces local biochemical and mechanical signaling mechanisms to regulate synaptogenesis, pruning, and plasticity (Pulikkottil et al., 2021; Winnubst & Lohmann, 2012). In the developing retinogeniculate system, there are two sources of correlated activity that could contribute to synaptic clustering: 1) visual experience that drives topographic activation of neighboring RGCs and 2) spontaneous retinal wave activity that correlates burst firing of neighboring RGCs prior to eye-opening. Consistent with experience-dependent plasticity, retinogeniculate bouton clustering increases after eye-opening (Bickford et al., 2010; Hong et al., 2014; Monavarfeshani et al., 2018) and visual deprivation reduces clustering (Hong et al., 2014). However, these experience-dependent changes occur long after the spontaneous activity-dependent segregation of eye-specific retinogeniculate axons prior to eye-opening (Godement et al., 1984; Jaubert-Miazza et al., 2005; Muir-Robinson et al., 2002). Before photoreceptor-mediated visual onset, retinal waves generate spatiotemporal correlations in RGC burst activity that are predicted to facilitate Hebbian strengthening of co-active synapses (Butts et al., 2007) and promote eye-specific synaptic clustering. Whether retinogeniculate synapse clustering begins prior to eye-opening and is regulated by spontaneous retinal activity is unknown.

To address this question, we used volumetric super-resolution microscopy together with anterograde tract tracing and immunohistochemical synaptic protein labeling to investigate the development of clustered eye-specific synapses in the dLGN prior to the onset of photoreceptor-mediated visual experience. During the first postnatal week, we identified a subpopulation of retinogeniculate synapses from both eyes-of-origin that contained larger presynaptic vesicle pools and multiple active zones (AZs). These "complex" synapses acted as loci for the clustering of synapses from the same eye (synaptic stabilization). At the same time, complex synapses of opposite eyes-of-origin showed a distance-dependent interaction that reduced synaptic clustering in an eye-specific manner during retinogeniculate competition (synaptic punishment). These patterns of synaptic stabilization and punishment were absent in a genetic mutant mouse line with disrupted stage II cholinergic retinal waves and abnormal eye-specific segregation. These results demonstrate that spontaneous retinal activity regulates retinogeniculate clustering prior to eye-opening and offers further support for the existence of non-cell-autonomous synaptic stabilization and punishment signals underlying eye-specific competition in the developing visual system.

Section 3 Results

Subsection 1 A unique set of complex synapses shows eye-specific differences during retinogeniculate segregation

To look for evidence of synaptic clustering during eye-specific segregation, we collected super-resolution imaging data in the dLGN of wild-type (WT) mice at three postnatal time points (P2, P4, and P8) (Figure 3.1A). We labeled eye-specific synapses by monocular injection of Alexa Fluor-conjugated cholera toxin subunit B tracer (CTB) together with immunostaining for presynaptic Bassoon, postsynaptic Homer1, and presynaptic vesicular glutamate transporter 2

(VGluT2) proteins (C. Zhang et al., 2023). Using volumetric STochastic Optical Reconstruction Microscopy (STORM) (Vatan et al., 2021), we collected separate image volumes (~45K μm3 each) from three biological replicates at each developmental time point. To determine whether spontaneous retinal activity impacts synaptic clustering across the same time period, we performed identical experiments in a knockout mouse line lacking the beta 2 subunit of the nicotinic acetylcholine receptor (β2KO), which disrupts spontaneous cholinergic retinal wave activity, eye-specific axonal segregation, and retinogeniculate synapse development (Bansal et al., 2000; Dhande et al., 2011; Grubb et al., 2003; Muir-Robinson et al., 2002; Rossi et al., 2001; Stafford et al., 2009; C. Sun et al., 2008; H. P. Xu et al., 2015, 2016; H. ping Xu et al., 2011; C. Zhang et al., 2023). Because eye-specific segregation is incomplete until P8 in the mouse, we limited our analysis to the future contralateral eye-specific region of the dLGN, which is reliably identified across all stages of postnatal development (Figure 3.1A, see also appendices A).

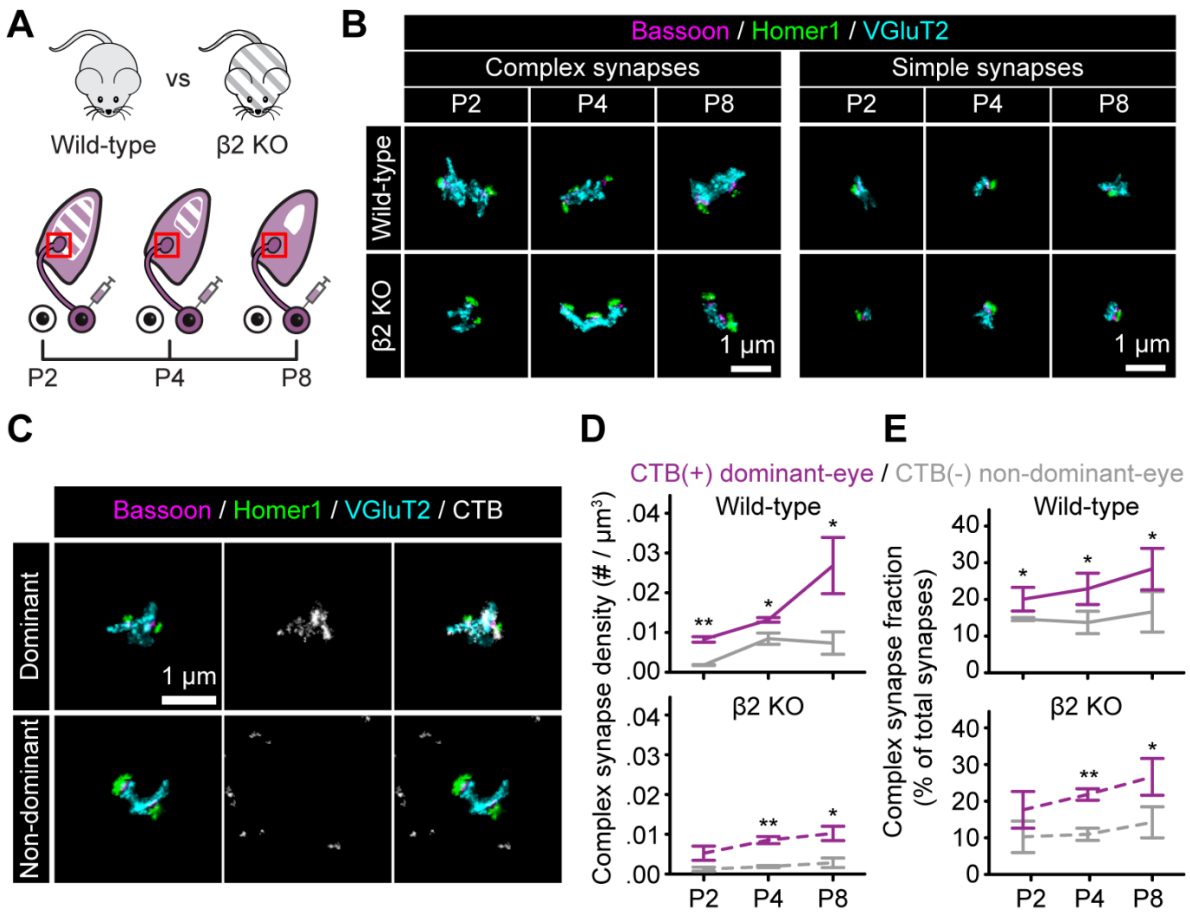


Figure 3.1 A unique set of complex synapses shows eye-specific differences during retinogeniculate segregation

(A) Experimental design: CTB-Alexa 488 was injected into the right eye of wild-type (WT) and β2KO mice. Tissue was collected from the left dLGN at P2, P4, and P8. The red squares indicate the STORM imaging regions.

(B) Representative complex (left panels) and simple synapses (right panels) in WT (top panels) and β2KO mice (bottom panels) at each age.

(C) Representative CTB(+) dominant-eye (top panels) and CTB(-) non-dominant-eye (bottom panels) complex synapses in a WT P8 sample, showing synaptic (left panels), CTB (middle panels), and merged immunolabels (right panels).

(D) Eye-specific complex synapse density across development in WT (top panel) and β2KO mice (bottom panel).

(E) Eye-specific complex synapse fraction across development in WT (top panel) and β2KO mice (bottom panel). In (D) and (E), error bars represent means ± SEMs. Statistical significance between CTB(+) and CTB(-) synapse measurements was assessed using one-way ANOVA. *: $p<0.05$, **: $p<0.01$. N=3 biological replicates for each age/genotype.

Across our dataset collected from different ages and genotypes, the enhanced resolution of STORM images revealed distinct subtypes of retinogeniculate synapses (Figure 7.5A). These included “complex” synapses characterized by the presence of multiple (2-4) Bassoon(+) active

zones (AZs) and greater VGluT2 signal, as well as “simple” retinogeniculate synapses that were smaller and contained a single AZ (Figures 3.1B and 7.5A). To determine the eye-of-origin for each retinogeniculate synapse, we measured the colocalization of the CTB signal with VGluT2 (Figure 3.1C). By imaging in the contralateral eye-specific region relative to the CTB-injected eye, we defined CTB(+) VGluT2 clusters as “dominant-eye” synapses originating from the contralateral eye. Conversely, CTB(-) VGluT2 clusters were classified as “non-dominant eye” synapses originating from the ipsilateral eye (Figure 3.1C). Our previous work using binocular CTB control injections confirmed the high efficiency of retinogeniculate synapse labeling by anterograde tracing, thereby enabling the accurate assignment of eye-specific synapses in the mouse brain (C. Zhang et al., 2023).

After assigning eye-of-origin to all retinogeniculate synapses, we measured the density of complex and simple synapses from both eyes over development. In WT mice, the density of CTB(+) dominant-eye complex synapses increased progressively from P2 to P8 (Figure 3.1D, upper panel). In contrast, the density of CTB(-) non-dominant-eye complex synapses increased from P2 to P4 and then decreased at P8 (Figure 3.1D, upper panel). The density of simple synapses followed the same pattern (Figure 7.5B, upper panel) consistent with the overall refinement of eye-specific synapses (C. Zhang et al., 2023). In β2KO mice, the density of both complex (Figure 3.1D, lower panel) and simple eye-specific synapses (Figure 7.5B, lower panel) was reduced relative to controls at P4 and P8.

To further investigate complex synapse maturation, we measured the fraction of complex synapses relative to the total synapse number over development. In WT mice, the total fraction of dominant-eye complex synapses increased from ~20% at P2 to ~29% at P8 while non-dominant-eye complex synapses remained constant between ~14-17% across the same period (Figure 3.1E, upper panel).

A similar pattern of eye-specific complex synapse maturation was found in β2KO mice (Figure 3.1E, lower panel), showing that relative proportions of complex versus simple synapses appeared normal despite an overall reduction in total synapse density when spontaneous retinal activity was disrupted (C. Zhang et al., 2023).

Subsection 2 Complex synapses undergo eye-specific vesicle pool maturation

Each complex synapse could represent an individual, larger RGC bouton with multiple active zones, or several clustered simple RGC boutons originating from one or more presynaptic RGC axons (Bickford et al., 2010; Monavarfeshani et al., 2018; Morgan et al., 2016). To distinguish these possibilities, we compared the developmental changes in VGluT2 volume and active zone number for complex versus simple synapses. In WT mice, both complex (Figure 3.2A, left panel) and simple (Figure 3.2B, left panel) synapses showed developmental increases and eye-specific differences in presynaptic VGluT2 volume. In WT complex synapses at P4, the median dominant-eye VGluT2 cluster volumes were 372% larger than non-dominant-eye VGluT2 clusters (Figure 3.2A, left panel). In contrast, β2KO mice showed a smaller magnitude difference (110%) between eye-specific complex synapse VGluT2 volume at the same time point (Figure 3.2A, right panel). In simple synapses at P4, the magnitudes of eye-specific differences in VGluT2 volume were reduced to 135% (WT, Figure 3.2B, left panel) and 41% (β2KO, Figure 3.2B, right panel). These results indicate that eye-specific differences in vesicle pool size are more significant for complex synapses versus simple synapses and that the maturation of both synapse types is regulated by spontaneous retinal activity.

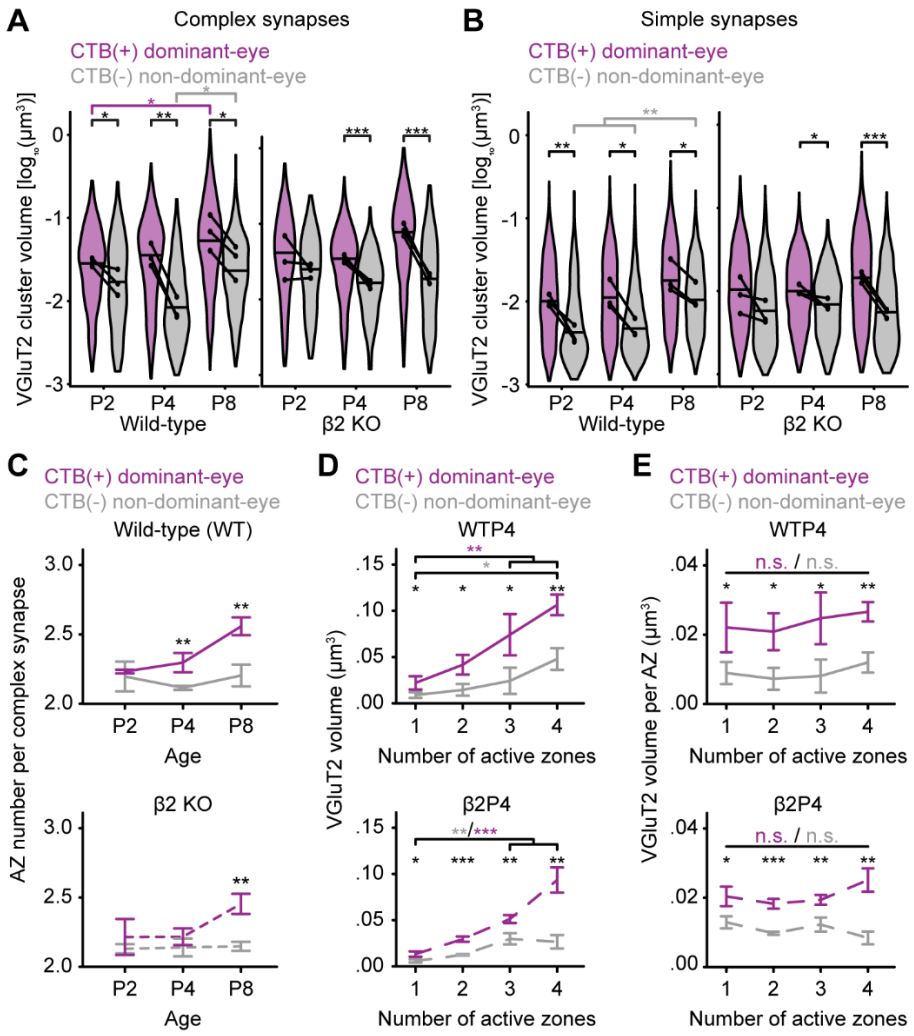


Figure 3.2 Complex synapses undergo eye-specific vesicle pool maturation
(A) Violin plots showing the distribution of VGluT2 cluster volume for complex synapses in WT and β2KO mice at each age. The black dots represent the median value of each biological replicate (N=3) and the black horizontal lines represent the median value of all synapses. Black lines connect measurements of CTB(+) and CTB(-) populations from the same biological replicate. Statistical significance was determined using a mixed model ANOVA with a post hoc Bonferroni test. Black asterisks indicate eye-specific differences and colored asterisks indicate differences across time points.
(B) Violin plots similar to (A) show the distribution of VGluT2 cluster volume for simple synapses in WT and β2KO mice at each age.
(C) Average number of active zones (AZs = individual bassoon clusters) per complex synapse in WT (top panel) and β2KO mice (bottom panel).
(D) VGluT2 cluster volume as a function of AZ number for all synapses in WT P4 samples (top panel) and β2KO P4 samples (bottom panel).
(E) Average VGluT2 cluster volume per AZ for all synapses in WT P4 samples (top panel) and β2KO P4 samples (bottom panel). In (C-E), error bars represent means ± SEMs from N=3 biological replicates. Statistical significance was assessed using one-way ANOVA with a post hoc Tukey's test. Black asterisks indicate eye-specific differences and colored asterisks indicate differences between simple (1 AZ) and complex (>1 AZ) synapses. "n.s." indicates no significance between simple and complex synapses. In all panels, *: $p<0.05$, **: $p<0.01$, ***: $p<0.001$.

We next measured the number of Bassoon clusters in each complex synapse and asked whether the corresponding VGluT2 cluster volume was consistent with a summation of VGluT2 volume from multiple simple synapses. In both WT (Figure 3.2C, top panel) and β2KO mice (Figure 3.2C, bottom panel), complex synapses were associated with an average of 2-3 Bassoon clusters in the first postnatal week. The average number of AZs in CTB(+) dominant-eye complex synapses increased from P2-P8, while CTB(-) non-dominant-eye synapses did not add AZs during this period (Figure 3.2C). For CTB(+) dominant-eye synapses in both WT and β2KO mice, the size of the vesicle pool was positively correlated with the number of AZs (Figures 3.2D and 7.6, A and B). This correlation was also present in CTB(-) non-dominant-eye synapses but with a smaller magnitude. Dividing the total presynaptic VGluT2 volume by the AZ number showed that simple and complex synapses had an equivalent presynaptic vesicle volume associated with each AZ (Figures 3.2E and 7.6, C-D). This suggests that complex synapses in the first postnatal week are comprised of several simple RGC synapses each with similar VGluT2 volume (putative nascent glomeruli). This conclusion is further supported by EM data showing that individual synaptic terminals in the P7 mouse dLGN are commonly associated with a single AZ (Bickford et al., 2010).

Subsection 3 Complex synapses are loci for synaptic clustering

Previous studies support the hypothesis that eye-specific competition is achieved through the stabilization and strengthening of co-active dominant-eye RGC inputs together with punishment and elimination of non-dominant-eye inputs (Assali et al., 2014; Fassier & Nicol, 2021; Faust et al., 2021). Within this context, complex synapses with multiple presynaptic release sites may drive strong postsynaptic responses and the induction of non-cell-autonomous stabilization and/or elimination signals that regulate synaptic cluster development (Louail et al., 2020; Rahman et al., 2020; Yasuda et al., 2021). To investigate whether complex synapses contribute to synaptic

clustering, we measured the fraction of eye-specific simple synapses located near like-eye complex synapses and compared this to a randomized simple synapse distribution (Figures 3.3, A-C). Simple synapses were considered nearby if their weighted centroids were within 1.5 μm of a complex synapse edge (Figures 3.3A and 7.7). For CTB(+) dominant-eye projections in WT mice, simple synapses showed non-random clustering near complex synapses, which increased progressively over development (Figure 3.3B, middle panel). In contrast, when searching for CTB(-) non-dominant-eye simple synapses nearby CTB(+) dominant-eye complex synapses, we found no evidence for synaptic clustering (Figure 7.7A, middle panel). These results indicate that CTB(+) dominant-eye complex synapses stabilize the local formation of like-eye-type simple synapses.

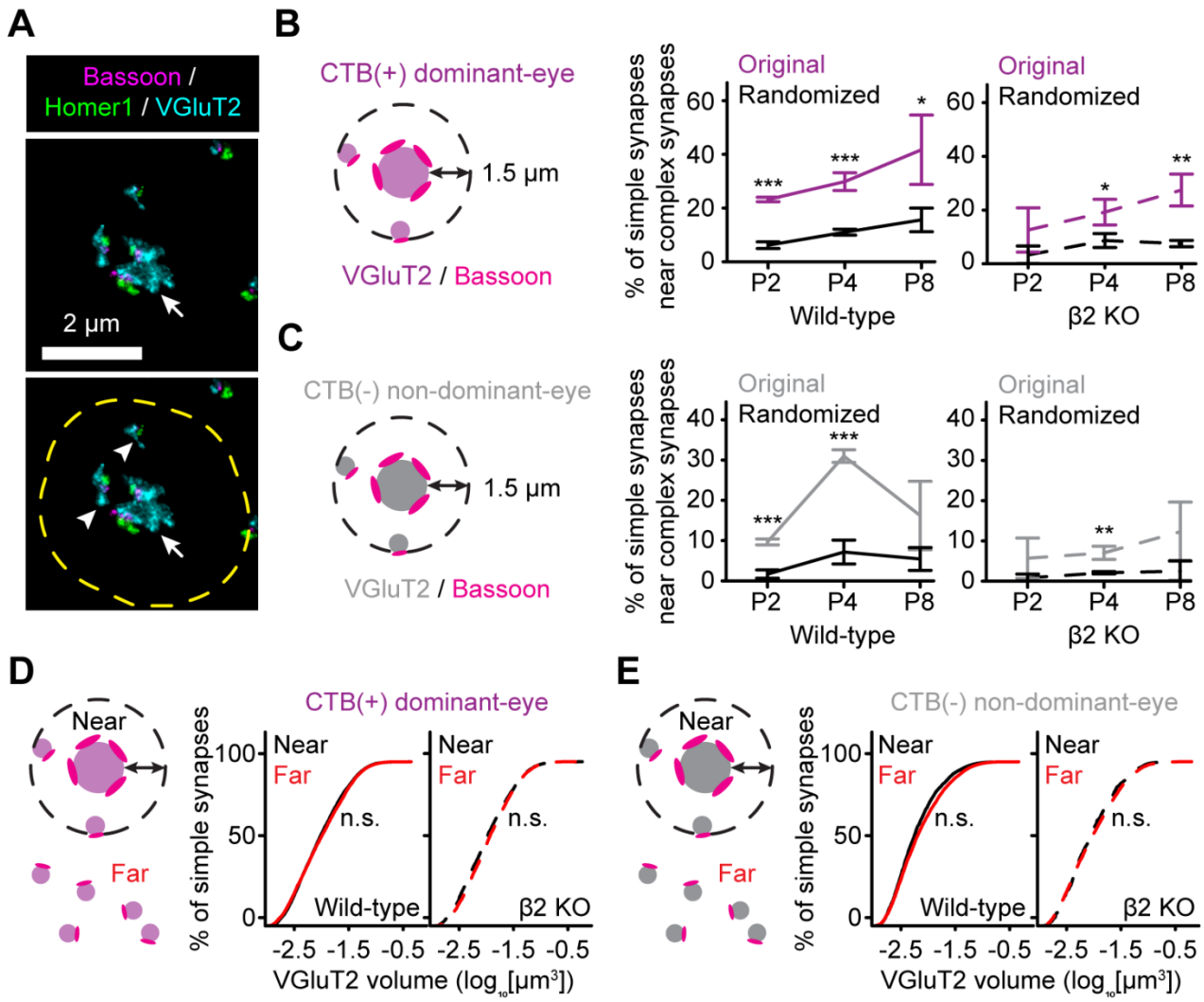


Figure 3.3 Complex synapses are loci for synaptic clustering

(A) A representative complex synapse in a WT P8 dLGN (arrow) with nearby simple synapses (arrowheads) clustered within 1.5 □m (dashed yellow ring).

(B) The fraction of CTB(+) dominant-eye simple synapses near like-eye complex synapses (cartoon) across development in WT (middle panel) and β2KO mice (right panel). Colored lines show the measured distributions and black lines show the results of a randomized simple synapse distribution within the sample imaging volume.

(C) Same as in (B) showing results for CTB(-) non-dominant-eye simple synapses near like-eye complex synapses. In B/C, a one-way ANOVA was used to test the statistical significance between original and randomized data. Error bars represent means ± SEMs. *: $p<0.05$; **: $p<0.01$; ***: $P<0.001$.

(D) Cumulative distribution of simple synapse VGluT2 volume for CTB(+) dominant-eye simple synapses near (<1.5 □m, black lines) or far from (>1.5 □m, red lines) like-eye complex synapses.

(E) Same as in (D) showing the cumulative distribution of simple synapse VGluT2 volume for CTB(-) non-dominant-eye simple synapse relative to like-eye complex synapses. The distributions in (D/E) show merged data across all developmental ages. A nonparametric Kolmogorov-Smirnov test was used for statistical analysis. “n.s.” indicates no significant difference between near and far simple synapse distributions.

Similarly, for CTB(-) non-dominant-eye complex synapses in WT mice, we observed a significant increase in the clustering of like-eye CTB(-) non-dominant-eye simple synapses nearby from P2 to P4 (Figure 3.3C, middle panel). Subsequently, the fraction of clustered simple synapses decreased from P4 to P8, reaching a level similar to randomized data (Figure 3.3C, middle panel). This increase in clustering coincides with ipsilateral RGC axon synaptogenesis (C. Zhang et al., 2023) and demonstrates that ipsilateral CTB(-) complex synapses promote local synaptogenesis despite being in the future contralateral eye-specific territory. However, after the close of eye-specific competition at P8, clustered CTB(-) simple synapses were eliminated, indicating that CTB(-) complex synapses failed to stabilize nearby simple synapses during eye-specific competition. This effect was not due to an overall loss of complex synapses as the CTB(-) complex synapse fraction was consistent across the first postnatal week (Figure 3.1E). Just as we found for CTB(+) dominant-eye complex synapses, CTB(-) non-dominant-eye complex synapses showed no selective stabilization of simple synapses from the opposite eye (Figure 7.7B, middle panel).

In β2KO mice, CTB(+) dominant-eye complex synapses also stabilized nearby like-eye simple synapses, although the effect size was reduced relative to controls (Figure 3.3B, right panel). Similarly, CTB(-) non-dominant-eye complex synapses in β2KO mice failed to stabilize like-eye simple synapses to the level seen in controls (Figure 3.3C, right panel). As we observed in control mice, complex synapses of either eye did not selectively stabilize opposite eye-synapses in β2KO mice (Figures 7.7, A and B, lower panels). Together, these results suggest that while local synapse stabilization mechanisms are at least partially maintained in β2KO mice, defects in spontaneous retinal activity reduce eye-specific synaptic clustering.

Based on our independent findings of eye-specific differences in vesicle pool volume (Figures 3.2, A and B) and non-random synapse clustering around complex synapses (Figures 3.3, A-C), we

hypothesized that complex synapses might also regulate the vesicle pool size of nearby simple synapses as a mechanism contributing to presynaptic maturation. To test this, we divided the population of simple synapses into two groups: those that were within a 1.5 μm radius of a like-eye complex synapse ('near') and those that were at any distance >1.5 μm ('far'). When comparing the vesicle pool volumes between near and far simple synapse groups across all ages and genotypes, we found no significant differences for either dominant-eye or non-dominant-eye simple synapses (Figures 3.3, D and E, displays the data merged for all time points). This result shows that activity-dependent synapse stabilization mechanisms do not impact simple synapse vesicle pool size.

Subsection 4 Complex synapses mediate distance-dependent synaptic stabilization and punishment underlying eye-specific competition

Complex synapses mediate distance-dependent synaptic stabilization and punishment underlying eye-specific competition

RGC axon refinement is a dynamic process involving branch stabilization and elimination based on the relative activity patterns among neighboring inputs (Munz et al., 2014; Rahman et al., 2020). Axonal remodeling is partially regulated by synaptic transmission (Koch et al., 2011) and the induction of non-cell-autonomous stabilization and punishment signals (Kutsarova et al., 2023; Louail et al., 2020; Yasuda et al., 2021). Although the precise mechanisms of axonal stabilization and punishment are not fully understood, it is likely that non-cell-autonomous signals operate at a local scale through direct cell-cell interactions or diffusible paracrine factors. Based on our observation that CTB(-) non-dominant-eye simple synapses initially cluster around like-eye complex synapses and were eliminated during the eye-specific competition (Figure 3.3C), we

hypothesized that CTB(-) synapses may be punished by nearby CTB(+) dominant-eye complex synapses in a distance-dependent manner.

To test this hypothesis, we first examined whether the size of CTB(-) non-dominant-eye complex synapses is affected by their spatial proximity to CTB(+) dominant-eye complex synapses (Figures 3.4, A and B). For each CTB(-) complex synapse, we measured the vesicle pool volume (Figure 3.4A, P4 data as an example) and AZ number (Figure 3.4B) as a function of each synapse's distance to the nearest CTB(+) complex synapse. We found no correlation between presynaptic properties and inter-eye complex synapse distances across all ages in both WT mice (Figures 3.4, A and B, left panels) and β2KO mice (Figures 3.4, A and B, right panels) (P2/P8 data not shown). These findings align with our earlier discovery that simple synapse vesicle pool volume is unaffected by proximity to complex synapses (Figure 3.3C), suggesting that presynaptic protein organization is not influenced by mechanisms governing synaptic clustering.

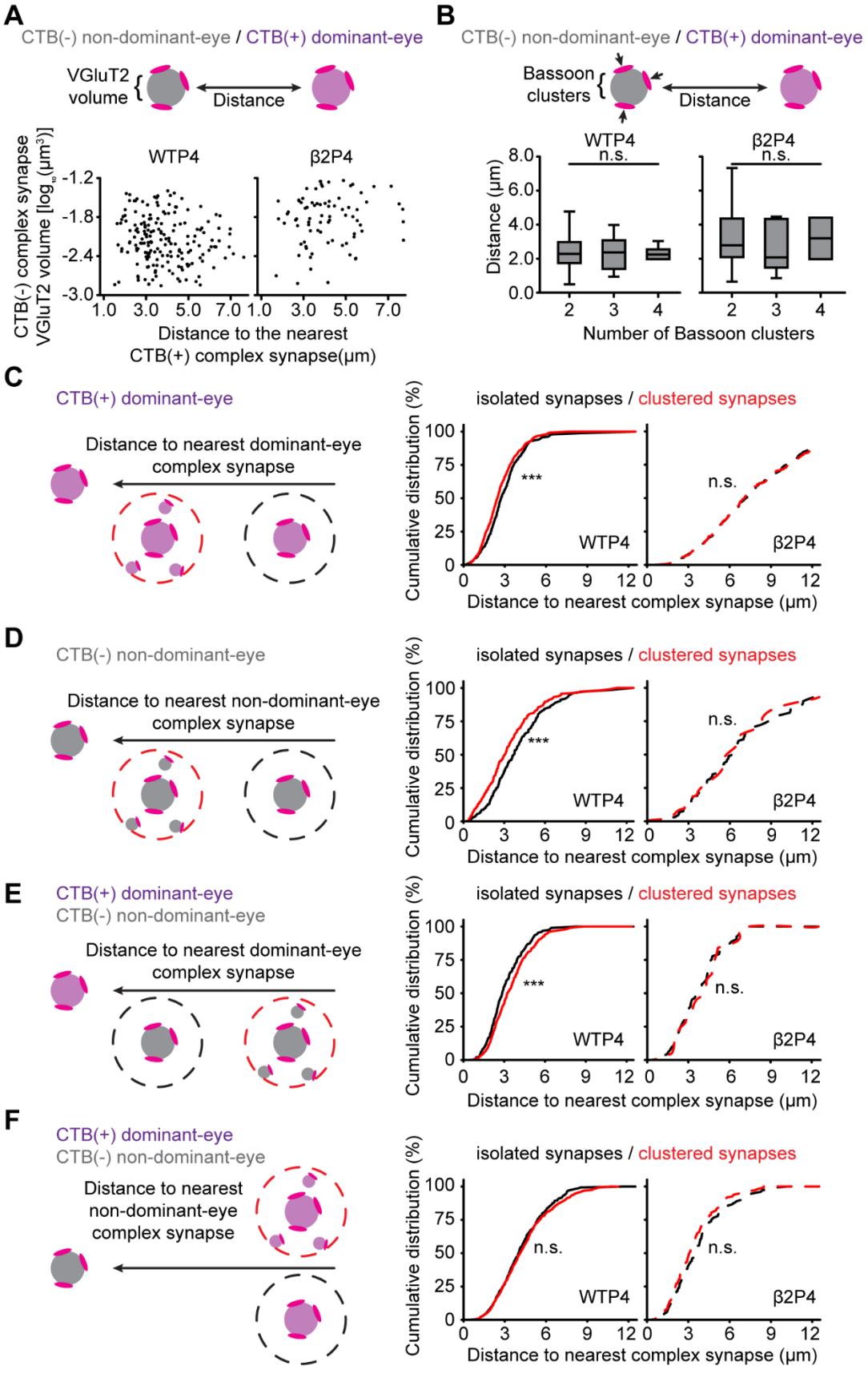

A
CTB(-) non-dominant-eye / CTB(+) dominant-eye
VGluT2 volume
Distance
WTP4
β2P4
CTB(-) complex synapse VGluT2 volume [log10(μm3)]
-1.2
-1.8
-2.4
-3.0
1.0 3.0 5.0 7.0 1.0 3.0 5.0 7.0
Distance to the nearest CTB(+) complex synapse(μm)
B
CTB(-) non-dominant-eye / CTB(+) dominant-eye
Bassoon clusters
Distance
WTP4
n.s.
β2P4
n.s.
Distance (μm)
8.0
6.0
4.0
2.0
0.0
2 3 4 2 3 4
Number of Bassoon clusters
C
CTB(+) dominant-eye
Distance to nearest dominant-eye complex synapse
isolated synapses / clustered synapses
Cumulative distribution (%)
100
75
50
25
0
***
n.s.
WTP4
β2P4
0 3 6 9 12 0 3 6 9 12
Distance to nearest complex synapse (μm)
D
CTB(-) non-dominant-eye
Distance to nearest non-dominant-eye complex synapse
isolated synapses / clustered synapses
Cumulative distribution (%)
100
75
50
25
0
***
n.s.
WTP4
β2P4
0 3 6 9 12 0 3 6 9 12
Distance to nearest complex synapse (μm)
E
CTB(+) dominant-eye
CTB(-) non-dominant-eye
Distance to nearest dominant-eye complex synapse
isolated synapses / clustered synapses
Cumulative distribution (%)
100
75
50
25
0
***
n.s.
WTP4
β2P4
0 3 6 9 12 0 3 6 9 12
Distance to nearest complex synapse (μm)
F
CTB(+) dominant-eye
CTB(-) non-dominant-eye
Distance to nearest non-dominant-eye complex synapse
isolated synapses / clustered synapses
Cumulative distribution (%)
100
75
50
25
0
n.s.
n.s.
WTP4
β2P4
0 3 6 9 12 0 3 6 9 12
Distance to nearest complex synapse (μm)

Figure 3.4 Complex synapses mediate distance-dependent synaptic stabilization and punishment underlying eye-specific competition
(A) VGluT2 volume of CTB(-) non-dominant-eye complex synapses relative to their distance to the nearest CTB(+) dominant-eye complex synapse in a WT P4 sample (left panel) and a β2KO P4 sample (right panel). Each black dot represents one synapse.
(B) Distributions of distances between CTB(-) non-dominant-eye complex synapses and their nearest CTB(+) dominant-eye complex synapse separated by the number of AZs within each CTB(-) complex synapse in WT P4 samples (left panel) and β2KO P4 samples (right panel). The median value is indicated by the horizontal line within the box, while the box boundaries represent quartile values. The whiskers represent the maximum and minimum values. A mixed model ANOVA was used to perform statistical tests. "n.s." indicates no significance differences.
(C) Cumulative distributions of distances between CTB(+) dominant-eye complex synapses and their nearest CTB(+) dominant-eye complex synapse (cartoon) in WT P4 samples (left panel) and β2KO P4 samples (right panel). Red lines indicate clustered complex synapses with nearby (<1.5 μm) simple synapses and black lines indicate isolated complex synapses with no nearby simple synapses.
(D) Same presentation as in (C), showing distances between CTB(-) complex synapses.
(E) Same presentation as in (C), showing distances between CTB(-) non-dominant-eye complex synapses and their nearest CTB(+) dominant-eye complex synapse (cartoon).
(F) Same presentation as in (C), showing distances between CTB(+) dominant-eye complex synapses and the nearest CTB(-) non-dominant-eye complex synapse. For C-F, nonparametric Kolmogorov-Smirnov tests were used for statistical comparisons. "***" indicates $p<0.001$, while "n.s." indicates no significant differences.

Next, we investigated whether complex synapses influence synaptic clustering around other nearby complex synapses in a distance-dependent manner. For this analysis, we categorized eye-specific complex synapses into two groups: complex synapses with nearby (< 1.5 μm) simple synapses from the same eye (referred to as “clustered”), and complex synapses with no nearby simple synapses (referred to as “isolated”). We then measured the distance between each complex synapse and its closest complex synapses from each eye-of-origin (Figures 3.4, C-F).

In WT mice at P4, we found that clustered CTB(+) dominant-eye complex synapses were closer to other CTB(+) complex synapses compared to isolated CTB(+) synapses, indicating a synaptic stabilization effect (Figure 3.4C, left panel). Similarly, clustered CTB(-) non-dominant-eye complex synapses were closer to the nearest CTB(-) complex synapse compared to isolated CTB(-) complex synapses (Figure 3.4D, left panel). These distance-dependent relationships were not observed when complex synapse positions of the target eye were randomized (Figures 7.8, A and

B). These findings indicate that complex synapses from both eyes are more likely to stabilize like-eye-type simple synapses when they are in closer proximity to other complex synapses from the same eye. The stabilization effect of CTB(+) complex synapse clustering persisted until P8 (Figure 7.8C, left panel). However, by P8, CTB(-) complex synapse stabilization was not observed (Figure 7.8D, right panel), consistent with synapse elimination and a loss of CTB(-) clustering by this time point (Figure 3.3C). Furthermore, distance-dependent effects on synaptic clustering at P4 were only observed in WT mice and not in β2KO mice (Figures 3.4, C and D, right panels; Figures 7.8, E and F, shows P8 β2KO data).

To look for evidence of competitive interactions between synapses from the two eyes, we next measured the distances between clustered and isolated CTB(-) non-dominant eye complex synapses and the closest CTB(+) dominant-eye complex synapses (Figure 3.4E). In WT mice at P4, we observed that isolated CTB(-) non-dominant-eye complex synapses were closer to the nearest CTB(+) dominant-eye complex synapse compared to clustered CTB(-) synapses (Figure 3.4E, left panel), consistent with an opposite-eye punishment signal. Similar to our findings on synaptic stabilization, this punishment effect was not observed in β2KO mice (Figure 3.4E, right panel) or when complex synapse positions of the target eye were randomized (Figures 7.8, A and B).

Lastly, we compared the distances between clustered versus isolated CTB(+) dominant-eye synapses with respect to CTB(-) non-dominant-eye complex synapses and we found no differences in WT mice (Figure 3.4F, left panel) or β2KO mice (Figure 3.4F, right panel). This suggests that complex synapses from the non-dominant-eye do not exert a punishment effect on synapses from the dominant-eye (Figure 3.4F). Together, these results demonstrate that complex synapses

contribute to eye-specific competition through activity-dependent stabilization and punishment mechanisms that act locally (within ~6 μm) to regulate synaptic clustering.

Section 4 Discussion

Relay neurons of the dLGN function as crucial hubs for the integration of RGC inputs within eye-specific synaptic clusters to drive spike output to the primary visual cortex. In this study, we used volumetric super-resolution microscopy together with eye-specific synaptic immunolabeling to show that 1) eye-specific synaptic clustering begins during retinogeniculate refinement prior to eye-opening, 2) synaptic clustering is regulated by a subpopulation of complex synapses with large vesicle pools and multiple AZs, 3) complex synapses regulate clustering through distance-dependent stabilization of like-eye synapses and punishment of opposite-eye synapses, and 4) eye-specific synaptic clustering relies on normal spontaneous retinal wave activity during the first postnatal week. These results advance our understanding of the developmental timeline of retinogeniculate glomerulus development and suggest that spontaneous neural activity regulates synaptic stabilization and punishment signals underlying competitive synaptic refinement in the developing visual system.

Previous anatomical studies have demonstrated the maturation of retinogeniculate glomeruli through the progressive clustering of RGC boutons following eye-opening in mice (Bickford et al., 2010; Hong et al., 2014; Monavarfeshani et al., 2018). This process is visual experience-dependent and is partly disrupted by sensory deprivation (late dark-rearing) (Hong et al., 2014). At maturity, retinogeniculate clusters are primarily eye-specific and contain very few, weak synapses from the non-dominant eye within each eye-specific region (Bauer et al., 2021; Rompani et al., 2017). Our STORM images reveal that eye-specific synaptic clustering emerges prior to eye-opening, during the period of eye-specific competition regulated by stage II cholinergic retinal

waves. This clustering is marked by the development of a subset of complex synapses that contain a greater number of synaptic vesicles and AZs (putative clustered RGC terminal boutons). These synapses differ from simple synapses (isolated RGC terminals) that have fewer vesicles and a single active zone.

Since our STORM images did not include a membrane stain, we were unable to identify the boundaries of individual RGC terminals. Therefore, it remains unclear whether complex synapses represent multiple RGC boutons or single terminals with multiple AZs. However, several lines of evidence suggest that complex synapses likely consist of two or more small RGC terminals, each with a single AZ. First, we found that the vesicle pool volume in complex synapses is proportional to the number of associated AZs, with each AZ having a comparable vesicle pool size to that of simple synapses. Second, the developmental increase in complex synapse vesicle pool volume matches that of simple synapses. Third, previous electron microscopy (EM) imaging data in the P7 mouse dLGN shows that synaptic profiles are small and mainly associated with a single AZ (Hong et al., 2014). Larger retinogeniculate terminals containing several AZs are observed later in development after eye-opening (Hong et al., 2014; Monavarfeshani et al., 2018).

Compared to mature synaptic glomeruli (~ 6 μm diameter), complex synapses formed during the first postnatal week are significantly smaller (~1 μm diameter). This suggests that further aggregation and convergence of RGC inputs are required for the maturation of complex synapses into bona fide glomeruli. Consistent with this, we found that complex synapses acted as local hubs for the clustering of additional like-eye-type simple synapses. The radius of simple synapse clustering around complex synapses was in the range of ~ 3-4 μm, indicating that these clustered simple synapses may serve as the substrate for glomerulus maturation.

In the adult dLGN, bouton clustering facilitates the convergence of RGC inputs representing similar visual features (e.g. direction of motion) and the integration of parallel visual channels carried by unique RGC mosaics (Liang et al., 2018; Morgan et al., 2016; Rompani et al., 2017). Retinal waves drive the co-activation of synaptic transmission in boutons from neighboring RGCs, which may support the development of clustered synaptic inputs to relay neurons. Consistent with this, pharmacological and genetic disruptions of cholinergic retinal wave propagation decrease direction-selective responses in postsynaptic neurons in the superior colliculus (Ge et al., 2021). Our STORM images revealed that in β2KO mice with disrupted retinal waves, complex synapses were formed and showed a development increase in vesicle pool volume and AZ number similar to WT mice (Figure 3.2). However, the clustering of simple synapses around complex synapses was reduced, though not eliminated (Figures 3.3, B and C), in β2KO mice. Since retinal waves persist in β2KO mice (Bansal et al., 2000; Stafford et al., 2009; C. Sun et al., 2008), a residual level of correlated activity between adjacent RGC synapses may be sufficient to promote synaptic clustering. In the future, it will be of interest to investigate how correlated synaptic activity impacts local clustering using pharmacological or optogenetic manipulations to reduce or enhance RGC correlations in the developing retina (Stellwagen et al., 1999; Stellwagen & Shatz, 2002; C. Sun et al., 2008; C. Zhang et al., 2011).

While studying the spatial relationships between complex synapses, we observed increased clustering of dominant-eye inputs (stabilization) and decreased clustering of non-dominant-eye inputs (punishment) depending on the distance between eye-specific complex synapses. Synaptic clustering was more likely to occur around complex synapses that were nearby other complex synapses from the same eye (within ~ 6 μm). This finding is consistent with the presence of non-cell-autonomous signals that regulate eye-specific axonal stabilization (Kutsarova et al., 2023;

Louail et al., 2020; Rahman et al., 2020). In addition to mechanisms that stabilize axon branches, eye-specific projections also undergo competitive refinement and axonal retraction mediated by punishment signals. Neurotransmission plays a crucial role in these mechanisms as shown by genetic deletions of VGluT2 or RIM1 proteins from ipsilaterally-projecting RGCs (Assali et al., 2017; Koch et al., 2011). These deletions decrease presynaptic vesicle release and prevent contralateral RGC axon retraction from the ipsilateral eye-specific territory in the dLGN (Assali et al., 2017; Koch et al., 2011). One downstream mediator of synaptic punishment is JAK2 kinase, which is phosphorylated in less active synapses (Yasuda et al., 2021). Similar to VGluT2 and RIM1 deletion phenotypes, over-expression of a dominant-negative mutant JAK2 lacking kinase activity prevents axon retraction in transfected RGCs during eye-specific competition (Yasuda et al., 2021).

Our super-resolution images show that synapse clustering is less likely to occur around non-dominant-eye complex synapses when they were located nearby dominant-eye complex synapses (a competitive punishment effect). This finding is consistent with previous studies of bulk axonal remodeling and highlights the role of synaptic punishment in axonal refinement phenotypes. In β2KO mice at P4, we did not find evidence of distance-dependent effects on synaptic clustering (either stabilization or punishment), indicating that spontaneous retinal activity regulates eye-specific synaptic clustering mechanisms at a local microcircuit scale (within ~ 6 μm). A possible mechanism underlying this effect is the activity-dependent development of functional presynaptic terminals. We previously found that β2KO mice fail to develop eye-specific differences in vesicle recruitment to the active zone, which are normally present in WT mice as early as P2 (C. Zhang et al., 2023). This effect is accompanied by an overall reduction in the number of retinogeniculate synapses in the β2KO mouse (C. Zhang et al., 2023). In the current study, we found that complex

synapses show greater eye-specific differences in presynaptic vesicle pool volume compared to simple synapses and that these eye-specific differences are significantly reduced in β2KO mice. Altogether, these results are consistent with a model in which spontaneous retinal activity regulates presynaptic development and vesicle release probability, which is required for the induction of local stabilization and punishment signals that govern eye-specific synapse clustering.

Our results in the developing retinogeniculate system bear similarities to the development of synaptic clusters in other circuits. During the refinement of the neuromuscular junction (NMJ), individual myocytes are initially innervated by multiple motor neuron axons that form intermingled synapses (Balice-Gordon et al., 1993; Gan & Lichtman, 1998). Subsequently, NMJ terminals undergo competitive refinement, where connections from a single motor axon are elaborated and strengthened while competing axons are eliminated (Sanes & Lichtman, 1999; Wyatt & Balice-Gordon, 2003). Similar to our findings on eye-specific complex synapse development, competition at the developing NMJ is also dependent on inter-synaptic distance, with motor axons losing connections that are in closer proximity to their competing synapses (Balice-Gordon et al., 1993; Gan & Lichtman, 1998). This process is activity-dependent, and blocking synaptic activity with pharmacological or genetic methods biases competition and leads to the elimination of the silenced inputs (Balice-Gordon & Lichtman, 1994; Buffelli et al., 2003). Interestingly, competing motor axon outputs show differences in presynaptic release probability at the early stages of development, suggesting that biases in presynaptic release may underlie competition (Kopp et al., 2000), possibly through the induction of local stabilization and punishment signals (Sanes & Lichtman, 1999).

While the molecular mechanisms regulating synaptic competition at the NMJ are not well understood, additional insights have been gained from studies of the developing hippocampus.

Synaptic clustering onto hippocampal pyramidal neurons is activity-dependent and is blocked by chronic application of TTX or NMDA-receptor antagonists (Kleindienst et al., 2011). Activation of NMDA receptors by co-active inputs triggers postsynaptic calcium-induced calcium-release and spreading calcium signals that regulate the maturation of clustered synapses (Lee et al., 2016). While co-active synapses are strengthened by spontaneous activity, synapses with asynchronous activity undergo synaptic depression, which is blocked by disruptions of proBDNF/P75NTR signaling (Winnubst et al., 2015). Similarly, the clustering of co-active inputs is prevented by manipulations of BDNF-TrkB signaling and matrix metalloproteinase 9 (MMP9), a proteinase that converts proBDNF to mature BDNF (Niculescu et al., 2018). Together, these findings suggest a model in which postsynaptic activation by co-active inputs drives local spreading intracellular calcium signaling, leading to proBDNF release. Extracellular proBDNF is then cleaved by MMP9 to induce BDNF-TrkB signaling, which stabilizes locally synchronized synapses and promotes cluster maturation (Niculescu et al., 2018). At the same time, proBDNF may weaken asynchronous synapses through P75NTR activation (Winnubst et al., 2015). Relating these neurotrophic mechanisms to visual system development, a computational model that incorporates BDNF-mediated synaptic refinement suggests that correlations in retinal waves are sufficient to induce local synaptic clustering contributing to orientation selectivity in cortical neurons (Kirchner & Gjorgjieva, 2021). Supporting a role for correlated spontaneous activity in synaptic refinement for the computation of directional motion, disruptions of retinal wave activity through pharmacological and genetic approaches reduce direction-selective responses in the mouse superior colliculus (Ge et al., 2021).

Although the molecular mechanisms underlying the clustering of eye-specific retinogeniculate inputs are still unknown, our STORM imaging results provide anatomical support for the existence

of local signaling factors that mediate non-cell-autonomous interactions, which underlie both synaptic stabilization and punishment. These factors may induce direct signaling between presynaptic RGC axon terminals or initiate postsynaptic responses that lead to reverse cell-cell signaling or the release of diffusible retrograde factors that stabilize and eliminate synapses based on input timing. JAK2/STAT signaling has been identified as one downstream regulator of synaptic punishment (Yasuda et al., 2021), which helps narrow the search for specific upstream induction signals in future experiments. It will also be of special interest to further investigate the eye-specific induction of glial-associated phagocytic signaling pathways that prune weak synapses during eye-specific segregation (Chung et al., 2013; Schafer et al., 2012; Stevens et al., 2007).

Section 5: Acknowledgment

The authors thank Dr. Michael C. Crair for generously sharing the β2KO mouse line used in this work. The research was funded by National Institutes of Health grant DP2MH125812 (CMS) and institutional startup support provided by the University of Maryland.

Section 6: Author contributions

Conceptualization: C.Z. and C.M.S.; Data Curation: C.Z., and C.M.S.; Formal Analysis: C.Z., and C.M.S.; Funding Acquisition: C.M.S.; Investigation: C.Z. and C.M.S.; Methodology: C.Z., and C.M.S.; Project Administration: C.Z. and C.M.S.; Resources: C.Z. and C.M.S.; Software: C.Z., and C.M.S.; Supervision: C.M.S.; Validation: C.Z. and C.M.S.; Visualization: C.Z. and C.M.S.; Writing – Original Draft Preparation: C.Z. and C.M.S.; Writing – Review & Editing: C.Z. and C.M.S.

Chapter 4: The influence of melanopsin on retinohypothalamic synapse development in the suprachiasmatic nucleus

This chapter consists of a manuscript in preparation for submission by Chenghang Zhang and Colenso M. Speer. The contribution of each author can be found in section 5.

Section 1: Abstract

The suprachiasmatic nucleus (SCN), a structure in the hypothalamus responsible for circadian rhythm regulation, receives input from intrinsic photoactive retinal ganglion cells (ipRGCs) expressing the photopigment melanopsin (OPN4). ipRGCs are important for the photoentrainment of SCN, but the role of OPN4 function in the maturation of retinohypothalamic tract (RHT) synapses is not yet understood. Using super-resolution fluorescent microscopy to investigate RHT synapse development, we found that OPN4 plays an important role in retinal synapse formation and activation in the SCN during the early developmental stage. Loss of OPN4 leads to reduced retinal synapse density and increased variability in the ratio of synapses with few or no docking vesicles but does not affect the total vesicle pool volume. Meanwhile, the subsequent maturation of RHT synapses after the first postnatal week shows diminished reliance on OPN4 function and further compensates for the early defects in the absence of OPN4. This study reveals a moderate impact of OPN4 in early RHT synapse development and sheds light on the role of photopigment in regulating SCN synapse plasticity.

Section 2: Introduction

The suprachiasmatic nucleus (SCN) is the primary circadian pacemaker in the brain. The SCN is innervated by intrinsic photoactive retinal ganglion cells (ipRGCs) that express the photopigment melanopsin (OPN4) via the retinohypothalamic tract (RHT) (for review, see Bedont & Blackshaw,

2015). Early studies suggested that OPN4 plays a crucial role in SCN circadian rhythm photoentrainment, but subsequent research has shown that its function in this process is limited. Knocking out the OPN4 gene in ipRGCs has only a mild effect on the circadian rhythm. The mutant mice show only slight defects in light-induced phase shift and period lengthening under constant light conditions (LL) (Panda et al., 2002; Ruby et al., 2002). Further study shows that rods are important for high-intensity light entrainment in the circadian rhythm, while melanopsin is required only for low-intensity light induction (Altimus et al., 2010). Despite the limited effect of OPN4, deleting ipRGCs has a significant impact on photoentrainment, indicating that the function of the rod and cone system in photoentrainment also goes through the ipRGC pathway (Aranda & Schmidt, 2021; Chew et al., 2017; Göz et al., 2008; Hatori et al., 2008). Conversely, light stimuli can restrict cone positions through ipRGCs, possibly via dopamine signaling (Tufford et al., 2018). These findings suggest that while the function of OPN4 may not be necessary, the connection from ipRGCs to SCN remains essential for photoentrainment of the circadian rhythm. Studies on the development of RHT axons suggest that ipRGC projection to the SCN is similar to adults after the first postnatal week, prior to the eye opening and functionality of rods and cones (Bedont & Blackshaw, 2015). During early development stages, OPN4 is the sole opsin capable of guiding the establishment of RHT wiring in the SCN. Research also suggests that before eye opening, OPN4 can promote glutamatergic retinal waves (Tiriac et al., 2018), potentially indicating an OPN4 activity-dependent maturation of RHT synapses in the SCN. However, the extent to which RHT synapses in the SCN during the first postnatal week depend on OPN4 activity remains unknown.

In this study, we utilized volumetric STochastic Optical Reconstruction Microscopy (STORM) to investigate the development of RHT synapses in the SCN. Our findings indicate disrupted

synaptogenesis and mild defects in the vesicle pool organization in OPN4 KO mice during early development, but these phenotypes are restored in adulthood. Our data provide insights into the early development of RHT synapses in the SCN, highlighting the role of OPN4 in early RHT circuit refinement.

Section 3: Result

Subsection 1: Deletion of OPN4 results in reduced retinal synapse density in the SCN

To investigate the impact of OPN4 on the development of RHT synapses in SCN, we performed dual eye injections of cholera toxin subunit B (CTB) conjugated with Alexa 488 and collected SCN tissue from OPN4 Het and KO mice at P8 and P60. We used CTB signals as a guide to collect tissues from N=3 biological replicates of each age and genotype (12 mice in total). The collected tissues were immunostained for presynaptic Bassoon protein and postsynaptic Homer1/2/3 protein. We also labeled the retinal input vesicle pools by using the vesicle glutamate transporter 2 (VGluT2) as a third marker (El-Danaf et al., 2015; Fujiyama et al., 2003; Hammer et al., 2014; Land et al., 2004). We used volumetric STORM imaging (Vatan et al., 2021) to obtain ~95k μm^3 super-resolution fluorescent images of the tissues, centered on the CTB labeling in the SCN. The reconstructed volume was further refined to approximately 40k μm^3 with a high and consistent density of CTB labeling. After image thresholding, fluorescent clusters were identified as RHT synapses when a Bassoon cluster was found close to a VGluT2 cluster and paired with a Homer1/2/3 cluster. The RHT synapses were identified at all ages and genotypes of the samples with the VGluT2-Bassoon-Homer1/2/3 order (Figure 4.1A). Details of the method can be found in chapter 2.

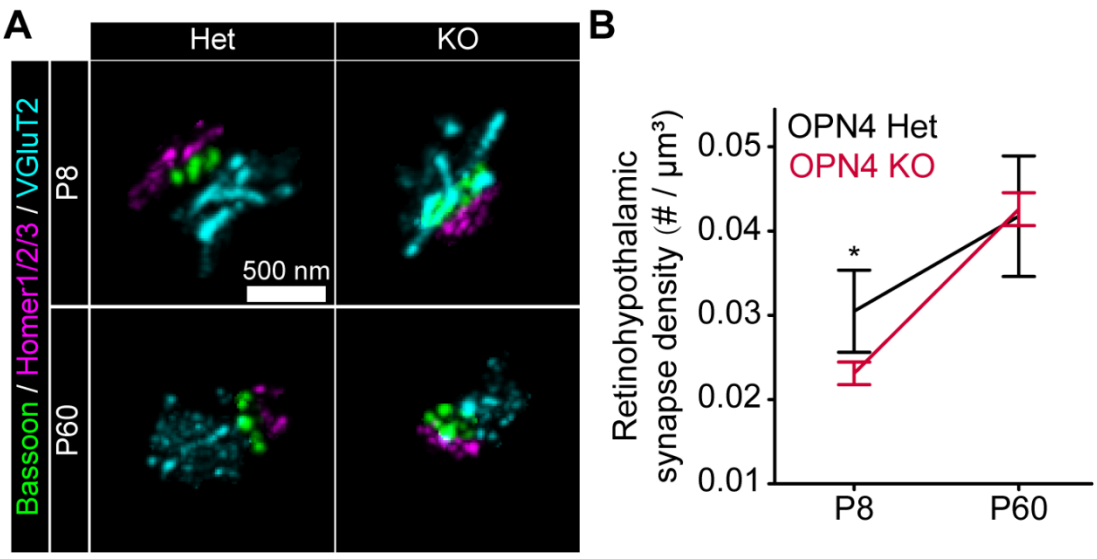


Figure 4.1: Deletion of OPN4 results in reduced retinal synapse density in the SCN
(A) Maximum Z-projections of STORM images showing representative RHT synapses at different ages (P8/P60) and genotypes (OPN4 Het/KO) in STORM images. Each image represents a stack of 210-420 nm. (B) Effect of OPN4 on retinal synapse density in the SCN. Retinal synapse density was lower in OPN4 KO mice compared to OPN4 Het mice at P8. The black line represents OPN4 Het mice, and the red line represents OPN4 KO mice. Error bars indicate means ± SEM, and statistical comparison was performed using one-way ANOVA. *: $P < 0.05$.

To investigate the effect of OPN4 KO on RHT synaptogenesis in the SCN, we measured the RHT synapse density within each refined ROI by dividing the number of VGluT2 clusters by the ROI volume. At P8, OPN4 KO mice exhibited a significantly lower synapse density than OPN4 Het mice (Figure 4.1B). When compared sample-to-sample, OPN4 mice may possess 11-32% more retinal synapses relative to OPN4 Het. From P8 to P60, both OPN4 Het and KO mice showed increased synapse density, and the increment was more significant in OPN4 KO mice. The developmental change in RHT synapse density from P8 to P60 suggests further synapse development after eye-opening, even though the overall axon occupation in the SCN is the same (Bedont & Blackshaw, 2015). Furthermore, the differences in synapse densities between genotypes were eliminated in adult mice at P60, indicating that further maturation of the RHT synapses may compensate for the loss of OPN4 function after P8.

Subsection 2: OPN4 KO has a limited effect on RHT synapse vesicle pool organization

To explore the potential impact of OPN4 on RHT synapse properties in the SCN, we measured the volume and signal intensity of VGluT2 clusters in all identified synapses across different ages and genotypes. We observed consistent VGluT2 cluster volume in both Het and KO mice from P8 to P60 (Figure 4.2A), but the VGluT2 signal intensity decreased (Figure 4.2B), leading to a reduced signal density from P8 to P60 (data not shown). Moreover, no significant differences were found in VGluT2 cluster volume or total signal intensity at any age between genotypes (Figures 4.2, A-B), suggesting that OPN4 does not affect vesicle pool development in the SCN, regardless of age.

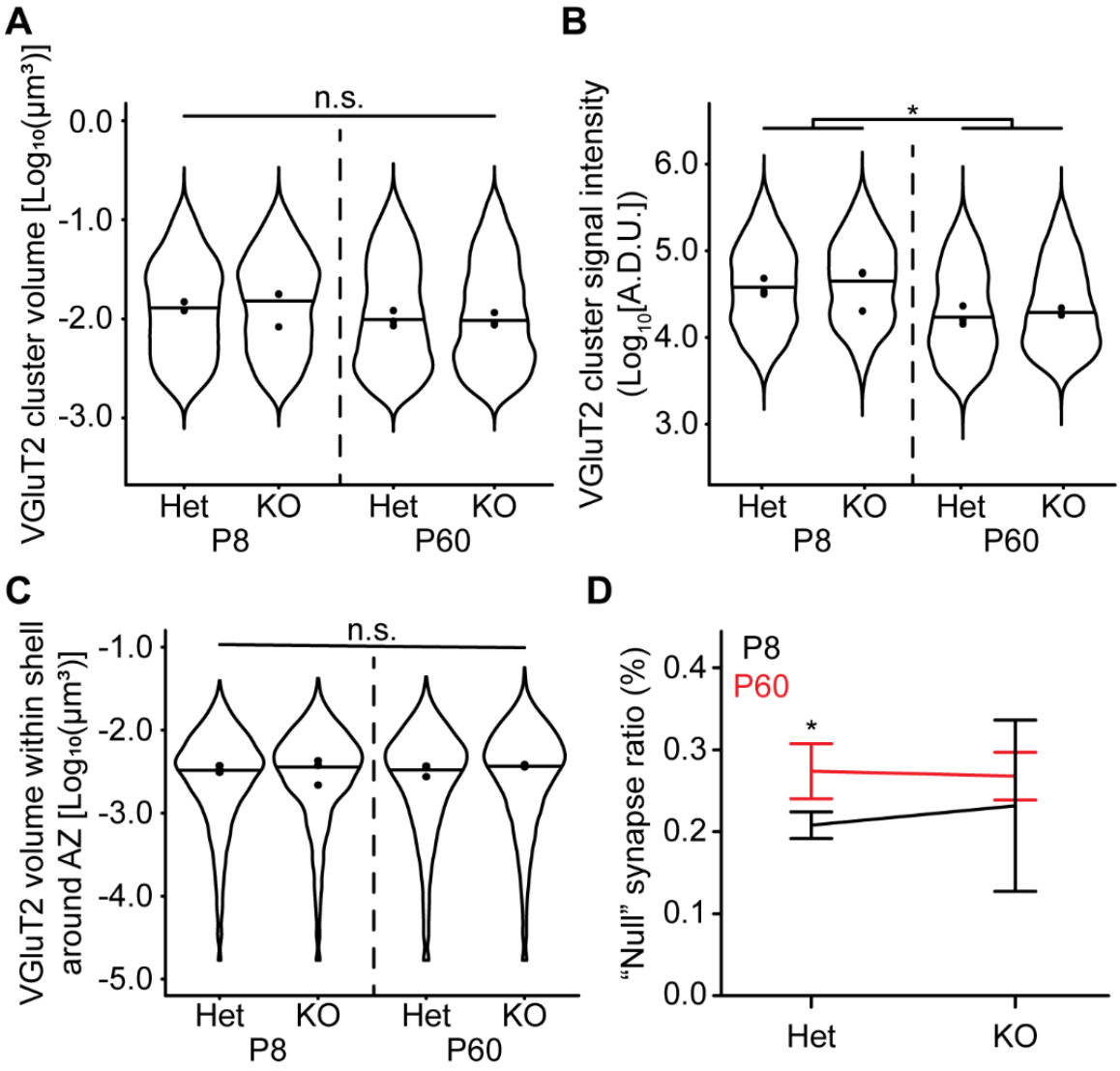


Figure 4.2 OPN4 KO has a mild effect on RHT synapse vesicle pool organization
(A) Distribution of VGluT2 cluster volumes of retinohypothalamic synapse in the SCN. The violin plot shows the distribution of all synapses across n=3 biological replicates in each age/genotype. The width of the violin plot is normalized across ages/genotypes. Black dots indicate the median value of each replicate, and the horizontal line is the median value of all quantified synapses. The statistical test was performed using mixed model ANOVA, where the genotype or age is the main factor and replicate ID is the random factor nested within the main factor. n.s.: not significant.
(B) Distribution of VGluT2 cluster total signal intensity of retinohypothalamic synapse in the SCN. Violin plot similar to (A). *: $P < 0.05$.
(C) Distribution of VGluT2 volume within 48 nm shell of associated Bassoon clusters. Violin plot similar as (A).
(D) Ratio of "null" synapses in the retinohypothalamic synapse of the SCN. Error bars represent means ± SEM. Statistical test was performed using one-way ANOVA. *: $P < 0.05$.

To investigate the impact of OPN4 on vesicle docking, we measured the VGluT2 signal volume within a 48 nm shell region surrounding Bassoon clusters to estimate the amount of vesicles associated with active zones (AZs). For non-“null” synapses that possess VGluT2 signals within the 48 nm shell, we found no differences in VGluT2 signals nearby AZs across ages and genotypes (Figure 4.2C), indicating that vesicle docking is not related to OPN4 function. Moreover, the ratio of “null” synapses that did not possess VGluT2 signals within the 48 nm shell region (also see chapter 2) was the same between OPN4 Het and KO mice. But in OPN4 Het mice, the fraction was slightly lower at P8 (Figure 4.2D). In OPN4 KO mice, although the average "null" synapse ratio was also higher at P60, the difference is not statistically significant due to the high variance in P8 data. These results suggest that OPN4 has a mild effect on regulating vesicle docking during early development, potentially underlying mechanisms to activate silent synapses.

Section 4: Discussion

Our study aimed to investigate the role of OPN4 in the development of retinohypothalamic synapses in the SCN and its relation to circadian rhythm photoentrainment. Using super-resolution fluorescent imaging, our results show that knocking out OPN4 leads to lower retinal synapse

density in the SCN at P8, but the effect was compensated by later RHT synapse maturation in adults. Moreover, loss of ONP4 has a mild effect on vesicle pool maturation. Even though the cross replicates variance of the "null" synapse ratio increased in OPN4 KO mice, the developmental tendency in vesicle pool volume and total signal intensity was intact.

The ipRGC is known to be involved in SCN circadian rhythm photoentrainment, but the role of OPN4 in this process appears to be not as essential as knocking out ipRGCs (Aranda & Schmidt, 2021). Our results indicate that OPN4 is involved in synaptogenesis during early development at P8, suggesting that OPN4 activity regulates the connectome in the retinohypothalamic pathway. However, this difference is eliminated in adult mice. It is possibly because the photoactivation of rods and cones after eye-opening guides the development of RHT synapses and compensates for defects before P8. Notably, similar to our findings, OPN4 KO disrupts synaptogenesis in multiple regions in cortices through an ipRGCs - supraoptic nucleus (SON) – paraventricular nucleus (PVN) oxytocin neuron circuit via enhancement of cerebral-spinal fluid (CSF) oxytocin level (Hu et al., 2022). It would be interesting to investigate whether similar defects in the signaling pathway occur in the SCN.

It's also unknown whether the defects we found at P8 are due to OPN4 photo activation or other OPN4-related function. OPN4 can react to light stimuli before eye opening. Light stimulation promotes glutamatergic retinal waves and the darkness condition from P8 to P14 causes reduced refinement in eye-specific segregation (Tiriac et al., 2018). In our dataset, reduced retinal synapse density in OPN4 KO mice is accompanied by a higher variance of the "null" synapse ratio across replicates, possibly indicating that failed OPN4-driven action potential disrupts vesicle docking and further lead to synapse elimination or less synaptogenesis from the retina. These suggest that ipRGCs play a role in early retinal circuit refinement through OPN4 photoactivation.

The mechanism by which ipRGC leads to photoentrainment in the SCN is not yet fully understood. One possible protein involved is Fos, which is known to be induced by photic stimuli and is related to nursing-induced entrainment of circadian rhythm in animals (González-Mariscal et al., 2016). In mice, the ability of ipRGC axons to respond to light stimuli is present in very early stages, as light pulse induces the expression of Fos around P4. KO of melanopsin leads to reduced light-induced c-fos expression (Ruby et al., 2002). During development, we observed a decrease in vesicle signal density, a phenomenon also reported in rabbits where CTB labeling revealed reduced labeling density from P9 (early developmental stage) to P19 (adult-level innervation pattern) (Juárez et al., 2013). In rabbits, light pulse induces Fos expression in the entire SCN (Juárez et al., 2013), while in adult mice, it only induces Fos in the ventrolateral region (Toledo et al., 2005). Together, these findings indicate changes in Fos expression during development and potential region-specific modulation of RHT input in the SCN.

An analysis of synapses in the core and shell regions of the SCN could be crucial to better understanding the role of OPN4 in photoentrainment. There is ample evidence suggesting that circadian rhythm is influenced by neural activity within different regions of the SCN. For instance, changes in photoperiod exposure can induce neurotransmitter switching between neuropeptide neuromedin S (NMS) neurons and vasoactive intestinal peptide (VIP) neurons in the core region (Porcu et al., 2022). Arginine vasopressin (AVP) receptor V1a deficiency in the shell region leads to a weakening of circadian locomotor rhythms (Li et al., 2009), and imaging studies have demonstrated that Bmal1 in AVP cells is essential for network synchrony within the SCN (Shan et al., 2020). Furthermore, Bmal1 deficiency in AVP leads to a lengthening of the free-running period and a weakening of coupling among SCN cells (Mieda et al., 2015). In our study, differentiating between the shell and core regions for analysis of synapse properties was

challenging due to the lack of SCN regional markers. Our data indicate that the synapse density in adults is approximately 0.04 #/μm^3, which is consistent with the core synapse density revealed by electron microscopy data (Calligaro et al., 2022). Indeed, during our CTB-guided selection of regions of interest (ROIs), we focused on regions with consistent dense CTB labeling. This suggests that our ROI primarily covers the core region of the SCN, but it cannot be ruled out that some parts of the shell may also be included. Further investigation of the spatial distribution of synapses is needed to explore the role of OPN4 in RHT synapse maturation.

To summarize, our findings provide initial insights into the influence of OPN4 on RHT connectivity during early development. OPN4 KO results in decreased synapse density and increased variability in the "null" synapse ratio. These results present an opportunity for further research on the region-specific development of RHT synapses in the SCN and the role of the rods and cones system in guiding synapse development after eye-opening.

Section 5: Author contributions

Conceptualization: C.Z. and C.M.S.; Data Curation: C.Z., and C.M.S.; Formal Analysis: C.Z., and C.M.S.; Funding Acquisition: C.M.S.; Investigation: C.Z. and C.M.S.; Methodology: C.Z., and C.M.S.; Project Administration: C.Z. and C.M.S.; Resources: C.Z. and C.M.S.; Software: C.Z., and C.M.S.; Supervision: C.M.S.; Validation: C.Z. and C.M.S.; Visualization: C.Z. and C.M.S.; Writing – Original Draft Preparation: C.Z.; Writing – Review & Editing: C.Z.

Chapter 5: Conclusion

Synapse imaging is an important method to understand the connectome in neural circuits of the brain. The diffraction limitation of light microscopy has led to the widespread use of electron microscopy (EM) for neuron processes and synapse reconstruction. However, the source of the neural process is hard to identify in EM reconstruction during early development. In EM images of the dorsal lateral geniculate nucleus (dLGN), retinal inputs are identified as terminals with large pale round mitochondria. But this phenotype is not present in mice younger than P14, making it difficult to study the retinogeniculate connectome during eye-specific segregation in the first postnatal week (Bickford et al., 2010). Similarly, identifying profiles in the suprachiasmatic nucleus (SCN) is also challenging (Calligaro et al., 2022). In this study, we employed volumetric STochastic Optical Reconstruction Microscopy (STORM) to image developing retinofugal projections in the brain (Vatan et al., 2021) and reveal the synaptic basis of eye-specific competition in the dLGN, as well as the impact of photopigment melanopsin (OPN4) function on retinohypothalamic synapse development in the SCN. Our data quantifies retinofugal synapses and reveals the developmental change in synaptic proteins, providing insight into the underlying activity-dependent mechanisms of synapse maturation.

Our investigation in the dLGN uncovers presynaptic plasticity during eye-specific competition. In the contralateral region of dLGN, dominant-eye synapses exhibit significantly larger vesicle pools and synapses from either eye with larger pools are more likely to survive competition. In addition, we observe disrupted vesicle docking to the active zone (AZ) during abnormal retinal spontaneous activity. Vesicle release probability has long been known to modulate activity-dependent synaptic strengthening and is mediated by several proteins involved in vesicle docking, release, and recycling. Studies of hippocampal neurons using EM have demonstrated that neural activity

induces vesicle docking in hippocampal neurons (Rey et al., 2020). Disrupted vesicle docking revealed in our data indicates that the release probability of retinogeniculate synapses is modulated by retinal waves. The data also suggest that normal eye-specific segregation involves transferring "null" synapses, which lack docking vesicles, to functionally active ones. This process may be crucial in establishing stable synapses that further stabilize the retinal axons, thus refining neural circuits. Overall, our date reveals significant presynaptic plasticity dependent on retinal activity that is related to eye-specific segregation. Further analysis will require investigation of specific activity-dependent presynaptic signaling pathways that drive retinogeniculate synapse maturation. Here, we labeled scaffolding proteins to identify presynaptic active zones and postsynaptic densities, which reliably report synapse position and size but offer little direct information about the process of vesicle release. Immunostaining proteins related to vesicle dockings, such as Munc13, or upstream signaling molecules, such as AC1, could provide insight into presynaptic plasticity in the retinogeniculate pathways.

Synaptic bouton clustering is a commonly observed phenomenon that facilitates signal integration and information processing (for review, see Kastellakis & Poirazi, 2019). Activity-dependent formation of bouton clustering has been demonstrated in the visual system (Binzegger et al., 2007; Kleindienst et al., 2011; Morgan et al., 2011). In the dLGN, retinogeniculate synapse bouton clustering has only been observed after eye opening at P14 (Monavarfeshani et al., 2018). Our data reveal the presence of complex synapses during the first postnatal week and show that synapse cluster around nearby like-eye complex synapses and de-cluster around nearby opposite-eye synapses. This suggests that the complex synapses drive a local competition mechanism, supporting that synaptic release generates non-cell-autonomous signals for stabilizing and eliminating nearby synapses (Fredj et al., 2010; Munz et al., 2014; Rahman et al., 2020; Ruthazer

et al., 2006). Previous studies have highlighted the roles of cAMP (Louail et al., 2020) and JAK2/STATS (Yasuda et al., 2021) signaling in local axon co-stabilization or elimination. Further testing of this hypothesis will require labeling of related proteins, manipulation of protein function, and labeling of retinal ganglion cell axons.

Intrinsic photoactive retinal ganglion cells (ipRGCs) have been reported to involve in the suprachiasmatic nucleus (SCN) circadian rhythm photoentrainment. However, the lack of techniques for retinohypothalamic synapse identification has hindered research on synapse development in this field. While ipRGCs are essential for circadian rhythm photoentrainment, the function of OPN4 had only a mild impact on circadian rhythm properties (Aranda & Schmidt, 2021). Our data reveal defects in synapse density and vesicle docking in OPN4 KO mice, suggesting the function of OPN4 in retinohypothalamic synapse maturation during the first postnatal week. Meanwhile, the later development of retinohypothalamic synapses compensates for the defects caused by OPN4 KO. However, more specific imaging and behavior experiments are needed to understand whether such further circuit wiring is caused by rods and cones. Moreover, a new technology using APEX to label the mitochondria of retinal input in the SCN has recently helped identify retinohypothalamic synapses using EM (Calligaro et al., 2022). The synapse density we reported in adults matches the synapse density in the core region in EM, suggesting that a better understanding of OPN4-dependent early synapse development requires analysis in the SCN differentiating the core and shell SCN regions.

This thesis presents the application of volumetric STORM for synapse imaging in developing thalamus and hypothalamus tissue. With appropriate protein antibodies, it can also be used to image synapse development and investigate connectome in other brain regions. In this dissertation, we report developmental changes in synapse density, synapse spatial distribution, and presynaptic

vesicle pool properties. However, the high image resolution of STORM enables the reconstruction of single molecule positions and analysis of subsynaptic domains (SSDs). Chapter 2 demonstrates a preliminary quantification of SSDs in retinogeniculate synapse development. In the future, applying the transformation matrix of volumetric STORM image processing to the raw single-molecule position distribution will allow for ground truth level reconstruction of molecules in 3D, providing an in situ study of SSD development during activity-dependent plasticity. This could significantly advance the understanding of synapse refinement at the molecular level.

Appendices A

Materials and methods

This section is mostly composed of the Star Method part of our publication "the synaptic basis of activity-dependent eye-specific competition" in Cell Reports, 2023 by Chenghang Zhang, Swapnil Yadav, and Colenso M. Speer (C. Zhang et al., 2023). It describes the methods and materials we used to conduct this dissertation. Additional details were added for complex synapse analysis (chapter 3) and suprachiasmatic nucleus (SCN) tissue processing (chapter 4). Related figures were added to the appendices as supplemental figures.

Animals

Wild-type C57BL/6J mice used in this study were purchased from the Jackson Laboratory (Stock Number 000664). β2KO mice were a generous gift from Dr. Michael C. Crair (Yale School of Medicine). All experimental procedures were performed in accordance with an animal study protocol approved by the Institutional Animal Care and Use Committee (IACUC) at the University of Maryland. Neonatal male and female mice were used interchangeably for all experiments. Tissue from biological replicates (n=3 animals) was collected for each age (P2/P4/P8 in dLGN and P8/P60 for SCN) from each genotype (18 animals total for dLGN and 12 animals for SCN).
Primers used for β2KO mice genotyping include:
Forward primer CAGGCGTTATCCACAAAGACAGA.
Reverse primer TTGAGGGGAGCAGAACAGAATC.
Mutant reverse primer ACTTGGGTTTGGGCGTGTTGAG.
Primers used for CRE include:
Forward primer TTAATCCATATTGGCAGAACGAAAACG.
Reverse primer CAGGCTAAGTGCCTTCTCTACA.

Primers used for OPN4 include:

Forward primer ATGGCCTTAGCTCCTCTGAGA.

Reverse primer GGATCCTGAGTTAAGCTTGACAAGA.

Eye injections

Intraocular eye injections were performed one day before tissue collection. Briefly, mice were anesthetized by inhalant isoflurane, and sterile surgical spring scissors were used to gently part the eyelid to expose the corneoscleral junction. A small hole was made in the eye using a sterile 34-gauge needle and ~0.5 µl of cholera toxin subunit B conjugated with Alexa Fluor 488 (CTB-488, ThermoFisher Scientific, Catalogue Number: C34775) diluted in 0.9% sterile saline was intravitreally pressure-injected into the right eye (for dorsal lateral geniculate nucleus, dLGN, tissue collection) or both eyes (for SCN tissue collection or control experiments) using a pulled-glass micropipette coupled to a Picospritzer (Parker Hannifin).

Tissue collection

Animals were deeply anesthetized with ketamine/xylazine and transcardially perfused with 5-10 mls of 37°C 0.9% sterile saline followed by 10 ml of room temperature 4% EM Grade paraformaldehyde (PFA, Electron Microscopy Sciences) in 0.9% saline. Brains were embedded in 2.5% agarose and sectioned in the coronal plane at 100 µm using a vibratome.

When collecting dLGN tissue, from the full anterior-posterior series of dLGN sections (~6-8 sections) we selected the central two sections for staining in all biological replicates. SCN tissue expands 3-4 sections and we selected the center one section for further process. The dLGN sections were morphologically consistent with Figures 134-136 (5.07-5.31 mm) of the postnatal day 6 mouse brain from Paxinos, et al., “Atlas of the developing mouse brain” Academic Press, 2020

(Figure 7.1A). Selected sections were postfixed in 4% PFA for 30 minutes at room temperature and then washed for 30-40 minutes in 1X PBS. The dLGN or SCN was identified by the presence of CTB-488 signals using a fluorescence dissecting microscope. A circular tissue punch (~500μm diameter) containing the dLGN or SCN was microdissected from each section using a blunt-end needle. A small micro-knife cut was made at the dorsal edge of the dLGN which, together with the CTB-488 signal, enabled us to identify the dLGN orientation during image acquisition (Figure 7.1A, also see "automated image acquisition").

Immunohistochemistry

We used a serial-section single-molecule localization imaging approach to prepare samples and collect super-resolution fluorescence imaging volumes as previously described (Vatan et al., 2021). dLGN or SCN tissue punches were blocked in 10% normal donkey serum (Jackson ImmunoResearch, Catalogue Number: 017-000-121) with 0.3% Triton X-100 (Sigma-Aldrich Inc.) and 0.02% sodium azide (Sigma-Aldrich Inc.) diluted in 1X PBS for 2-3 hours at room temperature and then incubated in primary antibodies for ~72 hours at 4°C. Primary antibodies used were Rabbit anti-Homer1 (for dLGN, Synaptic Systems, Catalogue Number: 160003, 1:100) or Rabbit anti-Homer1/2/3 (for SCN, Synaptic Systems, Catalogue Numebr: 160103, 1:100) to label postsynaptic densities (PSDs), mouse anti-Bassoon (Abcam, Catalogue Number AB82958, 1:100) to label presynaptic active zones (AZs), and guinea pig anti-VGluT2 (Millipore, Catalogue Number AB251-I, 1:100) to label presynaptic vesicles. Following primary antibody incubation, tissues were washed in 1X PBS for 6 x 20 minutes at room temperature and incubated in secondary antibody solution overnight for ~36 hours at 4°C. The secondary antibodies used in dLGN tissue staining were donkey anti-rabbit IgG (Jackson ImmunoResearch, Catalogue Number 711-005-152, 1:100) conjugated with Dy749P1 (Dyomics, Catalogue Number 749P1-01) and Alexa Fluor

405 (ThermoFisher, Catalogue Number: A30000), donkey anti-mouse IgG (Jackson ImmunoResearch, Catalogue Number 715-005-150, 1:100) conjugated with Alexa Fluor 647 (ThermoFisher, Catalogue Number: A20006) and Alexa Fluor 405, and donkey anti-guinea pig IgG (Jackson ImmunoResearch, Catalogue Number 706-005-148, 1:100) conjugated with Cy3b (Cytiva, Catalogue Number: PA63101). SCN tissue staining used the same secondary antibodies, but anti-mouse IgG was conjugated with Dy749P1 and anti-rabbit IgG was conjugated with Alexa Fluor 647 to improve postsynaptic labeling quality (Vatan et al., 2021). Tissues were washed 6 x 20 minutes in 1X PBS at room temperature after secondary antibody incubation.

Postfixation, dehydration, and embedding in epoxy resin

Tissue embedding was performed as previously described (Vatan et al., 2021). Tissues were postfixed with 3% PFA + 0.1% GA (Electron Microscopy Sciences) in PBS for 2 hours at room temperature and then washed in 1X PBS for 20 minutes. To plasticize the tissues for ultrasectioning, the tissues were first dehydrated in a graded dilution series of 100% ethanol (50%/70%/90%/100%/100% EtOH) for 15 minutes each at room temperature and then immersed in a series of epoxy resin/100% EtOH exchanges (Electron Microscopy Sciences) with increasing resin concentration (25% resin/75% ethanol; 50% resin/50% ethanol; 75% resin/25% ethanol; 100% resin; 100% resin) for 2 hours each. Tissues were transferred to BEEM capsules (Electron Microscopy Sciences) that were filled with 100% resin and polymerized for 16 hours at 70°C.

Ultrasectioning

Plasticized tissue sections were cut using a Leica UC7 ultramicrotome at 70 nm using a Histo Jumbo diamond knife (DiATOME). Chloroform vapor was used to reduce compression after cutting. For each sample, ~100 sections were collected on a coverslip coated with 0.5% gelatin

and 0.05% chromium potassium (Sigma-Aldrich Inc.), dried at 60 degrees for 25 minutes, and protected from light prior to imaging.

Imaging chamber preparation

Coverslips were chemically etched in 10% sodium ethoxide for 5 minutes at room temperature to remove the epoxy resin and expose the dyes to the imaging buffer for optimal photoswitching. Coverslips were then rinsed with ethanol and dH_2O. To create fiducial beads for flat-field and chromatic corrections, we mixed 715/755nm and 540/560nm, carboxylate-modified microspheres (Invitrogen, Catalogue Numbers F8799 and F8809, 1:8 ratio respectively) to create a high-density fiducial marker and then further diluted the mixture at 1:750 with Dulbecco's PBS to create a low-density bead solution. Both high- and low-density bead solutions were spotted on the coverslip (~0.7ul each) for flat-field and chromatic aberration correction respectively. Excess beads were rinsed away with dH2O for 1-2 minutes. The coverslip was attached to a glass slide with double-sided tape to form an imaging chamber. The chamber was filled with STORM imaging buffer (10% glucose, 17.5µM glucose oxidase, 708nM catalase, 10mM MEA, 10mM NaCl, and 200mM Tris) and sealed with epoxy.

Imaging setup

Imaging was performed using a custom single-molecule super-resolution imaging system. The microscope contained low (4x/10x air) and high (60x 1.4NA oil immersion) magnitude objectives mounted on a commercial frame (Nikon Ti-U) with back optics arranged for oblique incident angle illumination. We used continuous-wave lasers at 488nm (Coherent), 561nm (MPB), 647nm (MPB), and 750nm (MPB) to excite Alexa 488, Cy3B, Alexa 647, and Dy749P1 dyes respectively. A 405 nm cube laser (Coherent) was used to reactivate Dy749P1 and Alexa647 dye

photoswitching. The microscope was fitted with a custom pentaband/pentanotch dichroic filter set and a motorized emission filter wheel. The microscope also contained an IR laser-based focus lock system to maintain optimal focus during automatic image acquisition. Images were collected on a 640*640-pixel region (for dLGN) or a 896*896-pixel region (for SCN) of an sCMOS camera (ORCA-Flash4.0 V3, Hamamatsu Photonics) with a pixel size of ~155 nm.

Automated image acquisition

Fiducials and tissue sections on the coverslip were imaged using the low magnification objective (4X) to create a mosaic overview of the specimen. Beads/sections were then imaged at high-magnification (60X) to select regions of interest (ROIs) in the Cy3B and Alexa 488 channels. Before final image acquisition, laser intensities and the incident angle were adjusted to optimize photoswitching for STORM imaging and utilize the full dynamic range of the camera for conventional imaging.

Low-density bead images were taken in 16 partially overlapping ROIs. 715/755nm beads were excited using 750 nm light and images were collected through Dy749P1 and Alexa 647 emission filters. 540/560nm beads were excited using a 488 nm laser and images were collected through Alexa 647, Cy3B, and Alexa 488 emission filters. These fiducial images were later used to generate a non-linear warping transform to correct chromatic aberration. Next, ROIs within each tissue section were imaged at conventional (diffraction-limited) resolution in all four-color channels sequentially.

Following conventional image acquisition, a partially overlapping series of 9 images were collected in the high-density bead field for all 4 channels (Dy749P1, Alexa 647, Cy3B, and Alexa 488). These images were later used to perform a flat-field image correction of non-uniform laser illumination across the ROIs. Another round of bead images was taken as described above in a

different ROI of the low-density bead field. These images were later used to confirm the stability of chromatic offsets during imaging. All ROIs within physical sections were then imaged by STORM for Dy749P1 and Alexa 647 channels. Images were acquired using a custom progression of increasing 405nm laser intensity to control single-molecule switching. 8000 frames of Dy749P1 channel images were collected (60 Hz imaging) followed by 12000 frames of Alexa 647 channel images (100 Hz). In a second imaging pass, the same ROIs were imaged for Cy3B and Alexa 488 channels, each for 8000 frames (60 Hz).

We imaged the ipsilateral and contralateral ROIs separately in each physical section of the dLGN. For consistency of ROI selection across biological replicates at each age, we identified the dorsal-ventral (DV) axis of the dLGN and selected ROIs within the center (core region) at 2/5 (ipsilateral ROI) and 4/5 (contralateral ROI) of the full DV length (Figure 7.1A). In SCN tissue, imaging ROIs were positioned in the center of the CTB-stained region.

Image processing

Single-molecule localization was performed using a previously described DAOSTORM algorithm (Babcock et al., 2012). Molecule lists were rendered as 8-bit images with 15.5 nm pixel size where each molecule is plotted as an intensity distribution with an area reflecting its localization precision. Low-density fiducial images were used for chromatic aberration correction. We localized 715/755 beads in Dy749P1 and Alexa 647 channels, and 540/560 beads in Alexa 647, Cy3B, and Alexa 488 channels. A third-order polynomial transform map was generated by matching the positions of each bead in all channels to the Alexa 647 channel. The average residual error of bead matching was <15 nm for all channels. The transform maps were applied to both 4-color conventional and STORM images. Conventional images were upscaled (by 10X) to match the STORM image size. The method to align serial sections was previously described (Vatan et

al., 2021). STORM images were first aligned to their corresponding conventional images by image correlation. To generate an aligned 3D image stack from serial sections, we normalized the intensity of all Alexa 488 images and used these normalized images to generate both rigid and elastic transformation matrices for all four-color channels of both STORM and conventional data. The final image stack was then rotated and cropped to exclude incompletely imaged edge areas. Images of the dLGN ipsilateral regions were further cropped according to CTB-488 signals to exclude contralateral areas. And Images of the SCN were also further cropped to exclude regions on the edge without dense CTB labeling.

Cell body filter

The aligned STORM images had non-specific labeling of cell bodies in Dy749P1 and Alexa 647 channels. To limit synaptic cluster identification to the neuropil region we identified cell bodies based on their Dy749P1 signal and excluded these regions from further image processing. STORM images were convolved with a Gaussian function (σ=140nm) and then binarized using the lower threshold of a two-level Otsu threshold method. We located connected components in the thresholded images and generated a mask based on components larger than e^{11} voxels. Because cell body clusters were orders of magnitude larger than synaptic clusters, the cell body filter algorithm was robust to a range of size thresholds. The mask was applied to images of all channels to exclude cell body areas.

Eye-specific synapse identification and quantification

To correct for minor variance in image intensity across physical sections, we normalized the pixel intensity histogram of each section to the average histogram of all sections. Image histograms were rescaled to make full use of the 8-bit range. Using a two-level Otsu threshold method, the

conventional images were thresholded into three classes: a low-intensity background, low-intensity signals above the background representing non-synaptic labeling, and high-intensity signals representing synaptic structures. The conventional images were binarized by the lower two-level Otsu threshold, generating a mask for STORM images to filter out background signals. STORM images were convolved with a Gaussian function (σ= 77.5nm) and thresholded using the higher two-level Otsu threshold. Following thresholding, connected components were identified in three dimensions using MATLAB 'conncomp' function. A watershedding approach was applied to split large clusters that were improperly connected. Clusters were kept for further analysis only if they contained aligned image information across two or more physical sections. We also removed all edge synapses from our analysis by excluding synapses that did not have blank image data on all adjacent sides. To distinguish non-specific immunolabeling from true synaptic signals, we quantified two parameters for each cluster: cluster volume and cluster signal density calculated by the ratio of within-cluster pixels with positive signal intensity in the raw STORM images. Two separate populations were identified in 2D histograms plotted from these two parameters. We manually selected the population with higher volumes and signal densities representing synaptic structures. To test the robustness of the manual selection, we performed multiple repeated measurements of the same data and discovered a between-measurement variance of <1% (data not shown).

To identify paired pre- and postsynaptic clusters, we first measured the centroid-centroid distance of each cluster in the Dy749P1 and Alexa 647 channels to the closest cluster in the other channel. We next quantified the signal intensity of each opposing synaptic channel within a 140 nm shell surrounding each cluster. A 2D histogram was plotted based on the measured centroid-centroid distances and opposing channel signal densities of each cluster. Paired clusters with closely

positioned centroids and high intensities of apposed channel signal were identified using the OPTICS algorithm. Retinal inputs were identified by pairing Bassoon clusters with VGluT2 (Cy3B) clusters using the same method as pre/post-synaptic pairing. In total we identified 49,414 synapses from WT samples (3 samples each at P2/P4/P8, 9 total samples) and 33,478 synapses in $\beta 2^{-/-}$ mutants (3 samples each at P2/P4/P8, 9 total samples) in dLGN. In SCN, we identified 7,997 synapses from OPN4 Het mice (3 samples each at P8/P60, 6 total samples) and 9,104 synapses from OPN4 KO mice (3 samples each at P8/P60, 6 total samples). In dLGN, synapses from the right eye were identified by pairing VGluT2 clusters with CTB (Alexa 488) clusters. The volume of each cluster reflected the total voxel volume of all connected voxels, and the total signal intensity was a sum of voxel intensity within the volume of the connected voxels.

VGluT2 population analysis

To identify 'small' versus 'large' VGluT2 clusters in dLGN, we used the MATLAB 'histfit' function to smooth the VGluT2 cluster volume histogram by fitting it to the kernel density distribution. The smoothed curve was then fit to the equation:

$$f(x) = a_1 * e^{-\left(\frac{x-b_1}{c_1}\right)^2} + a_2 * e^{-\left(\frac{x-b_2}{c_2}\right)^2}$$

with the following boundary conditions:

$$a_1, a_2 > 0$$

$$b_1, b_2 < 0$$

The peak positions were determined by the fitting results of b_1 and b_2.

Analysis of vesicles associated with the AZ

In both dLGN and SCN tissues, AZ-associated vesicles were quantified by VGluT2 signal volume and signal intensity within 48 nm proximity to its paired Bassoon cluster (~ length of 3 pixels in

STORM images and slightly larger than the diameter of a synaptic vesicle). AZ-associated VGluT2 signal volume linearly increased when progressively increasing the shell size (16-32-48-64 nm; data not shown). Synapses with no VGluT2 signal inside a 48 nm AZ shell were defined as 'null' synapses.

SSD analysis based on voxel intensity distributions

In dLGN, SSDs were identified by applying a watershedding algorithm (MATLAB) on interpolated synaptic cluster images with 15.5 nm isotropic voxels. The image was convolved with a Gaussian filter (σ=24 nm for the 647 channel and 32 nm for the 750 channel) before watershedding. Watershedding parameters were initially chosen based on visual inspection of SSD segmentation output on a subset of randomly selected synaptic clusters. To further validate the output, watershedding parameters were applied to shuffled pixel intensity distributions within convex hulls of all synaptic clusters. In shuffled controls, fewer than 10% of clusters showed any SSDs (data not shown).

To quantify the transsynaptic SSD displacement, we applied principal component analysis (PCA) to each pre/postsynaptic cluster independently to find the unit vector $\overrightarrow{v_1}$ perpendicular to each cluster plane based on the first two principal components. Paired Bassoon and Homer1 clusters were included in the transsynaptic SSD displacement analysis if the offset angle between their individual $\overrightarrow{v_1}$ vectors was <30 degrees indicating parallel pre/postsynaptic alignment. We then measured a second vector $\overrightarrow{v_2}$ that connected the weighted centroid of each presynaptic (Bassoon) SSD to its closest neighboring postsynaptic (Homer1) SSD. When an individual Homer1 SSD was paired with multiple Bassoon SSDs, the pair with the smallest distance was maintained in the analysis.

The transsynaptic SSD displacement was calculated by:

$$\sqrt{\left|\overrightarrow{(v_2)}\right|^2 - \left|\overrightarrow{(v_1)} \cdot \overrightarrow{(v_2)}\right|^2}$$

The randomized transsynaptic SSD displacement was calculated from the same equation above, using shuffled SSD centroid distributions within the convex hull of each Homer1 cluster while maintaining the original presynaptic SSD positions.

SSD analysis based on single molecule localization distributions

In dLGN for each synaptic cluster identified in image-based analysis, we performed an SSD analysis based on single molecular localization distributions. After STORM image acquisition, 2D single molecule distribution (ground truth data) was determined for each individual physical section. We converted molecule distributions to image pixel intensity values (2D STORM images), which were then processed for drift correction, chromatic alignment correction, and 3D elastic registration to generate final STORM volumetric image stacks. To retrieve the single molecule distributions for SSD identification, we developed a machine learning approach to reconstruct single-molecule positions in 3D from volumetrically aligned STORM image stacks. First, to establish a relationship between image voxel intensity and single molecule distributions, we estimated the nearest-neighbor-averaged (NNA) number of single molecules present in each pixel within 2D STORM images of synaptic clusters. We sampled individual image clusters from non-volumetrically-aligned 2D STORM images, for which we have corresponding pixel intensity distributions and ground truth single molecule localizations. We used a linear function to fit the relationship between NNA pixel intensity and the NNA number of molecules for each pixel, enabling the estimation of NNA molecules per pixel based on NNA pixel intensity.

In step two, we used a Convolutional Neural Network (CNN) to refine the estimation of NNA molecules per pixel. Individual 2D STORM image clusters were centered in a fixed-size tile and

fed to the CNN as inputs. The output of the network was an ordered list of residual errors between the predicted number of molecules (from step one) and the actual number of molecules (from the ground truth STORM localization lists) present in each pixel. Within a dataset of >14,000 input-output pairs, 90% of the dataset was used for the training process and the remaining 10% was used for validation. In the training process, the CNN minimized the training error which is the sum of the mean-squared prediction error for pixels in all clusters. The training process significantly decreased the training error, indicating that the CNN improved upon the initial molecule distribution estimation from step one (data not shown). Predictions on the validation dataset also showed decreased prediction error. The trained CNN was used to predict the number of molecules inside each pixel of synaptic clusters within volumetrically-aligned STORM image stacks. For 3D reconstruction, the positions of predicted molecules in each pixel were then assigned randomly in a 15.5 x 15.5 x 70 nm voxel.

In step three, we identified SSDs based on the local density of reconstructed 3D molecular distributions for each synaptic cluster. A DBSCAN clustering algorithm was used to predict SSDs within each 3D cluster. We optimized DBSCAN parameters to produce subcluster identification with a good visual agreement with SSD analysis based on image voxel intensity distribution. To avoid false positive detection of SSDs, we applied the same DBSCAN analysis to shuffled data (randomized localization positions within each cluster convex hull) and found small SSDs with few localizations (mean 6-7 localizations/SSD). From this, we set a threshold for SSD selection in the original data 3σ above the average number of molecules in small SSDs from the shuffled analysis. We then analyzed the volumetrically aligned datasets to compute the number of SSDs within each synapse and the volume of each SSD.

To evaluate whether SSDs identified from the predicted single molecule distributions reflect ground truth SSDs, we randomly selected 50,000 clusters from 2D STORM images and applied the trained CNN model to generate predicted molecule localizations. We then applied DBSCAN analysis using the same parameters to the ground truth localizations and CNN-predicted molecule localizations. After matching the closest neighboring SSDs from the two datasets and calculating the SSD centroid offsets, we found 88% of Bassoon SSDs and 82% of Homer1 SSDs in the ground truth data were paired with an identified SSDs in the CNN predicted data with a centroid offset of < 70 nm (thickness of the physical section). We quantified the offsets between all closest paired SSDs in the two datasets to show the total error in SSD identification. These were compared to randomized data generated by assignment of each SSD centroid to a random position within the full CNN predicted single molecule distribution (see chapter 2).

Complex synapse identification and quantification

To determine whether an eye-specific VGluT2 cluster is a complex synapse or a simple synapse, we measured the number of active zones (defined by individual Bassoon clusters) associated with each VGluT2 cluster in the dataset. A 3D shell was extended 140 nm from the surface voxels of each VGluT2 cluster and any Bassoon clusters that fell within the shell were considered to be associated with the target VGluT2 cluster. The number of active zones (AZs) associated with each VGluT2 cluster was then measured. VGluT2 clusters associated with more than 1 AZ were defined as complex synapses, while those associated with only 1 AZ were defined as simple synapses. Quantification of complex and simple synapse VGluT2 cluster volume was performed using the "regionprops" function in MATLAB, which provided the voxel size and weighted centroid of each VGluT2 cluster. The search for simple synapses adjacent to complex synapses (synaptic clustering analysis) was conducted using a similar search approach as for associated Bassoon clusters, with

expansion shell sizes ranging from 1 μm to 4 μm from the surface voxels of each complex synapse. The main figures in the study utilized an expansion size of 1.5 μm. An eye-specific simple synapse was considered to be near a complex synapse if its weighted centroid fell within the expanded region.

Statistical analysis

Statistical analysis was performed using SPSS. Plots were generated by SPSS or R (ggplot2). The statistical details can be found in the figure legends.

For all measurements in this dissertation, we analyzed n = 3 biological replicates (individual mice) for each genotype (wild-type, β2KO, OPN4 Het, or OPN4 KO) at each age (P2/P4/ P8 for dLGN tissues and P8/P60 for SCN tissues). We used a linear mixed model to compare cluster/SSD volumes and total signal intensity. In each comparison, age or eye-of-origin was the fixed main factor and biological replicate IDs were nested random factors. Pairwise comparisons among main factor groups were performed by a post-hoc Bonferroni's test. Cluster densities, average SSD numbers per cluster, average transsynaptic SSD displacements, synapse complexity, and all synapse fraction measurements were presented as means ± SEM values in line plots and were compared by one-way ANOVA tests with a post-hoc Tukey's test. Non-parametric Kolmogorov-Smirnov test was used in all cumulative histogram comparisons in Chapter 3.

In violin plots, each violin showed the distribution of grouped data from all biological replicates from the same condition. Each black dot represents the median value of each biological replicate and the horizontal black line represents the group median. Black lines connect measurements of CTB (+) and CTB (-) populations from the same biological replicate. Asterisks in all figures indicate statistical significance: *P<0.05, **P<0.01, ***P<0.001.

Appendices B

Supplemental figures

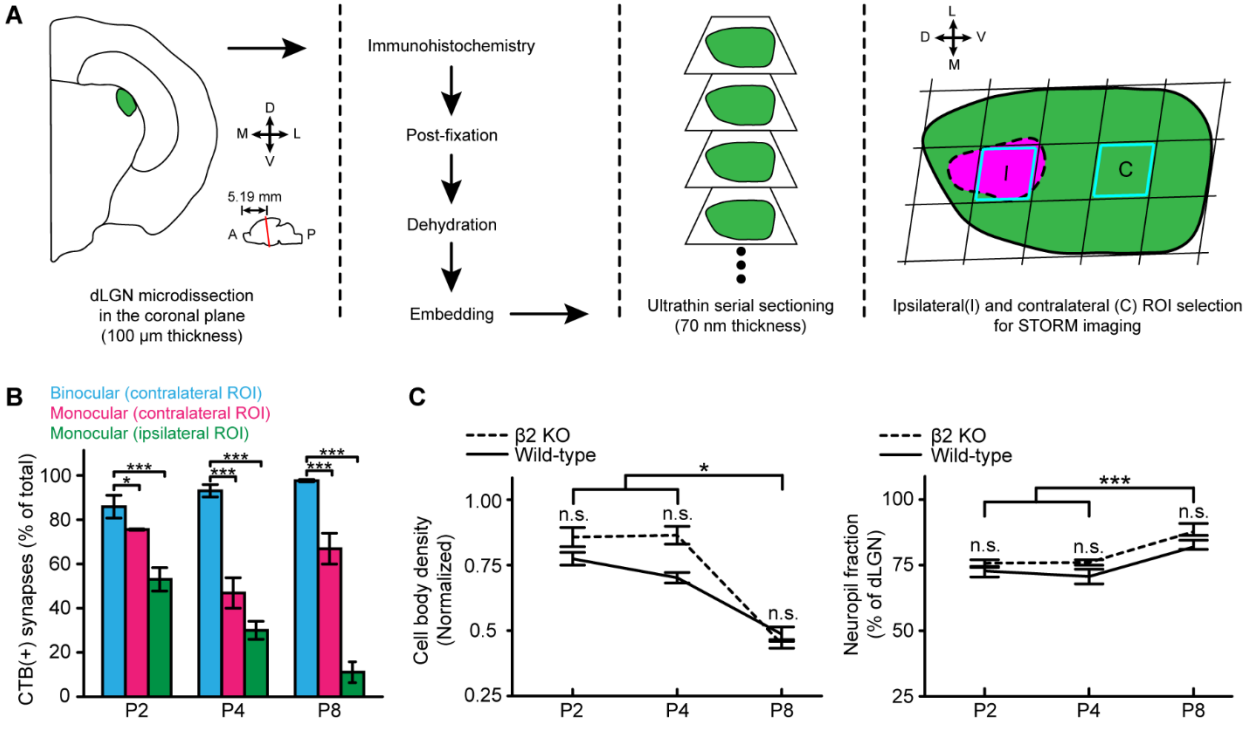


Figure 7.1 High efficiency eye-specific synapse labeling and normal dLGN cytoarchitectural development in β2KO mice, related to Figure 2.1.

(A) Overview of sample preparation and image acquisition. The mouse brain was dissected (100 µm thick coronal sections) and dLGN tissue (green) was microdissected for immunohistochemistry, post-fixation, dehydration, embedding, and serial ultrasectioning (70 nm section thickness). The right panel shows the positions of selected ipsilateral and contralateral ROIs. Magenta and green indicate eye-specific regions innervated by axons of the ipsilateral eye and contralateral eye in adult mice. The grid lines show the ipsilateral/contralateral ROI selection within the dLGN center (along the ML axis) at 2/5 and 4/5 distance respectively (along the maximal DV axis).

(B) CTB labeling efficiency in retinogeniculate synapses during development. The bar plot shows the fraction of VGluT2 clusters (retinogeniculate synapses) co-labeled with CTB signals in binocular or monocular injection experiments for WT mice over development. Error bars reflect means ± SEM from N = 3 biological replicates at each age. Statistical analysis was performed using a one-way ANOVA with a post-hoc Tukey's test. *P<0.05, ***P<0.001.

(C) Normal dLGN cytoarchitecture development in WT and β2KO mice. Line plots show the cell body density (left panel) and neuropil fraction (right panel) measurements combined from ipsilateral and contralateral ROIs. The cell body densities were normalized to the total imaging volume for each ROI. Error bars reflect means ± SEM for N = 3 biological replicates for each age and genotype. Statistical analysis was performed using a one-way ANOVA with a post-hoc Tukey's test. *P<0.05. ***P<0.001. "n.s." = not significant.

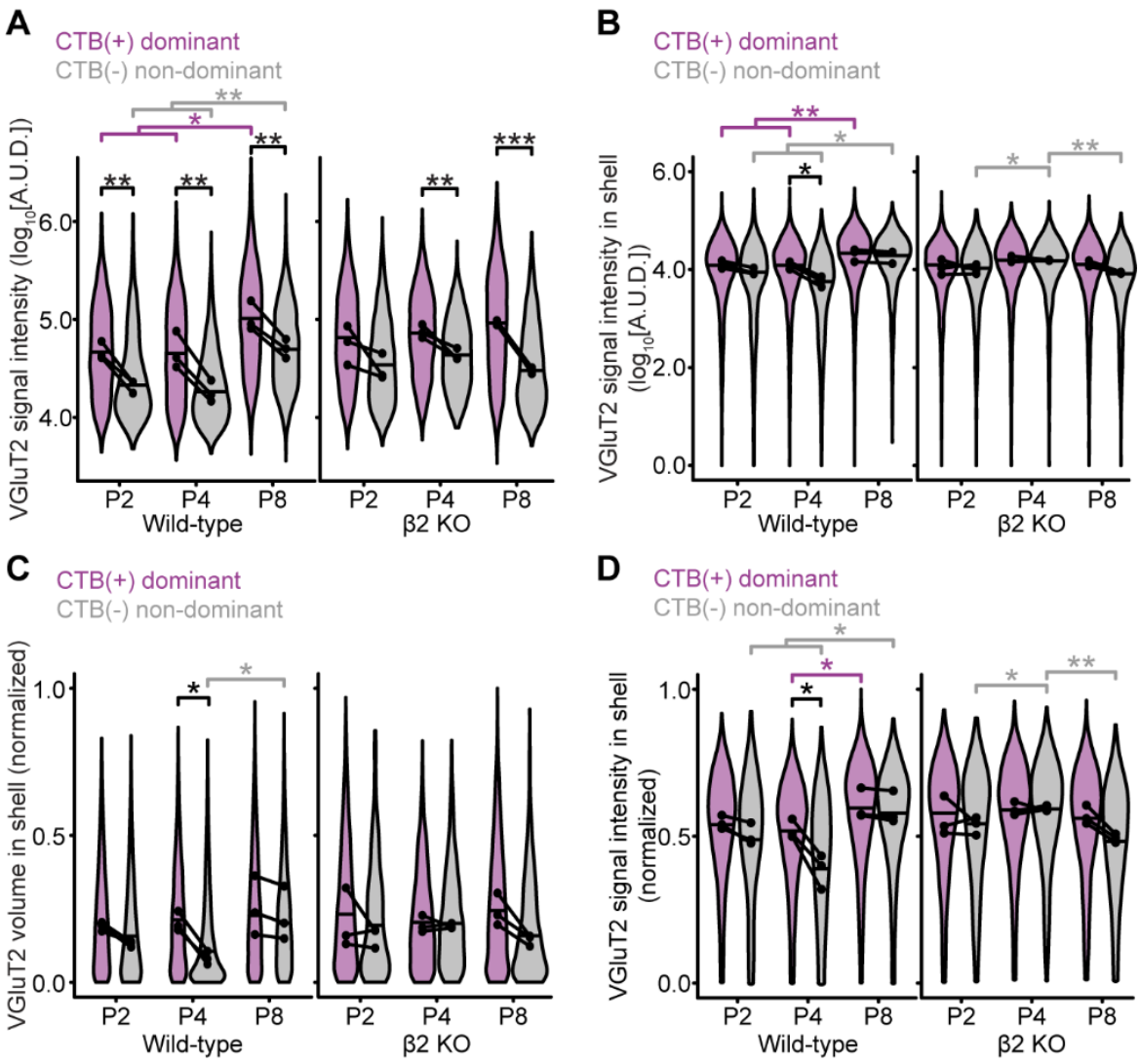


Figure 7.2 Developmental maturation of VGluT2 cluster signal intensity and within-shell VGluT2 properties during eye-specific competition, related to Figure 2.2.

(A) Eye-specific developmental changes in VGluT2 signal intensity in WT (left panel) and β2KO mice (right panel). For all results in A-D, the violin plots show the grouped distribution from 3 biological replicates imaged in the contralateral ROI. Horizontal lines show the median values of the grouped data. Black dots reflect the individual median values for each biological replicate. Black lines between CTB(+) and CTB(-) populations represent data collected from the same biological replicate sample. Statistical analysis was performed using a mixed model ANOVA

where the age or eye-of-origin was the fixed main factor, and the biological replicate ID was a random nested factor. Pair-wise comparisons between ages were performed using a post-hoc Bonferroni's test. Black asterisks indicate statistical comparison between eye-specific CTB(+) and CTB(-) clusters. Purple asterisks indicate statistical comparisons between CTB(+) clusters across ages. Gray asterisks indicate statistical comparisons between CTB(-) clusters across ages. *P < 0.05, **P < 0.01.

(B) Eye-specific VGluT2 signal intensity at the AZ in WT (left panel) and β2KO mice (right panel) across development.

(C) Eye-specific VGluT2 volume at the AZ in WT (left panel) and β2KO mice (right panel) across development normalized to the AZ volume.

(D) Eye-specific VGluT2 signal intensity at the AZ in WT (left panel) and β2KO mice (right panel) across development normalized to the AZ volume.

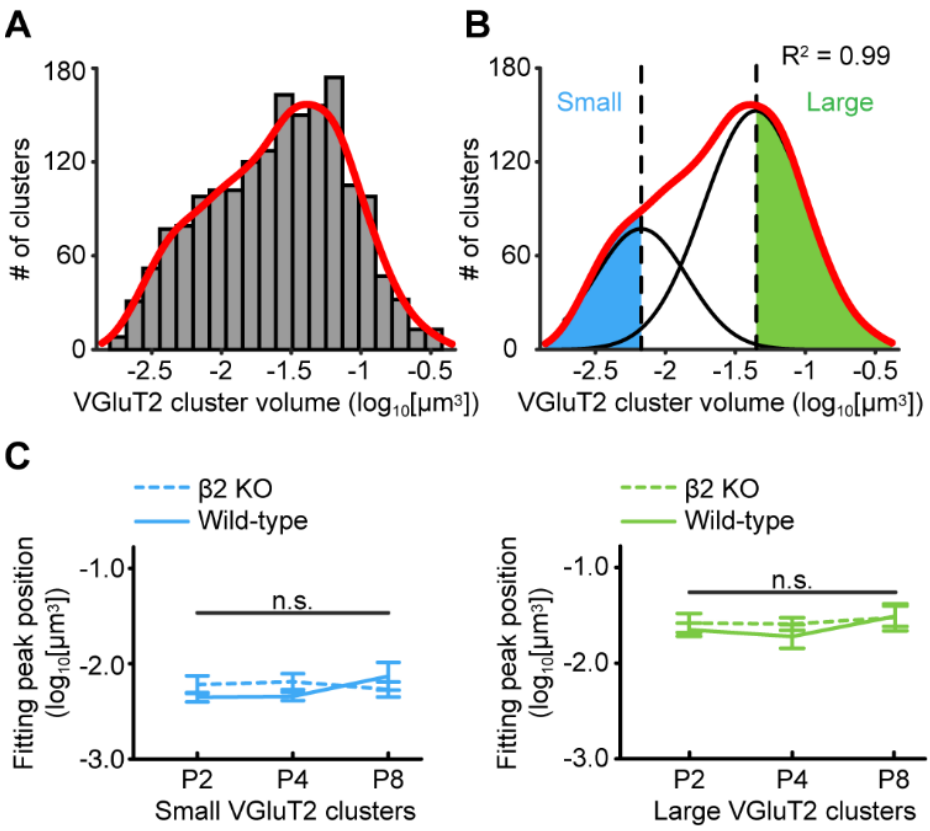


Figure 7.3 Identification of small versus large VGluT2 cluster populations during eye-specific segregation, related to Figure 2.3.

(A) Histogram of VGluT2 cluster volumes in the contralateral ROI. Gray bars show a CTB(+) VGlUT2 cluster volume histogram from a representative WT P8 sample. The histogram was fit with the kernel density estimation as a smoothed distribution (red line).

(B) Definition of small versus large VGluT2 clusters in the same sample as (A). The smoothed histogram (red line same as A) was fit by a 2-peak Gaussian function (black lines). The peak position of each Gaussian function (black dashed lines) defined small (blue) and large (green) clusters respectively. R^2 value reflects the coefficient of determination.

(C) Cluster fitting was consistent across all ages and genotypes. The line plots show the smaller Gaussian peak position (left panel) and larger Gaussian peak position (right panel) for WT (solid lines) and β2KO (dashed lines) mice. Error bars reflect means ± SEM from N = 3 biological

replicates for each age and genotype. Statistical analysis was performed using a one-way ANOVA with a post-hoc Tukey's test. "n.s" = not significant.

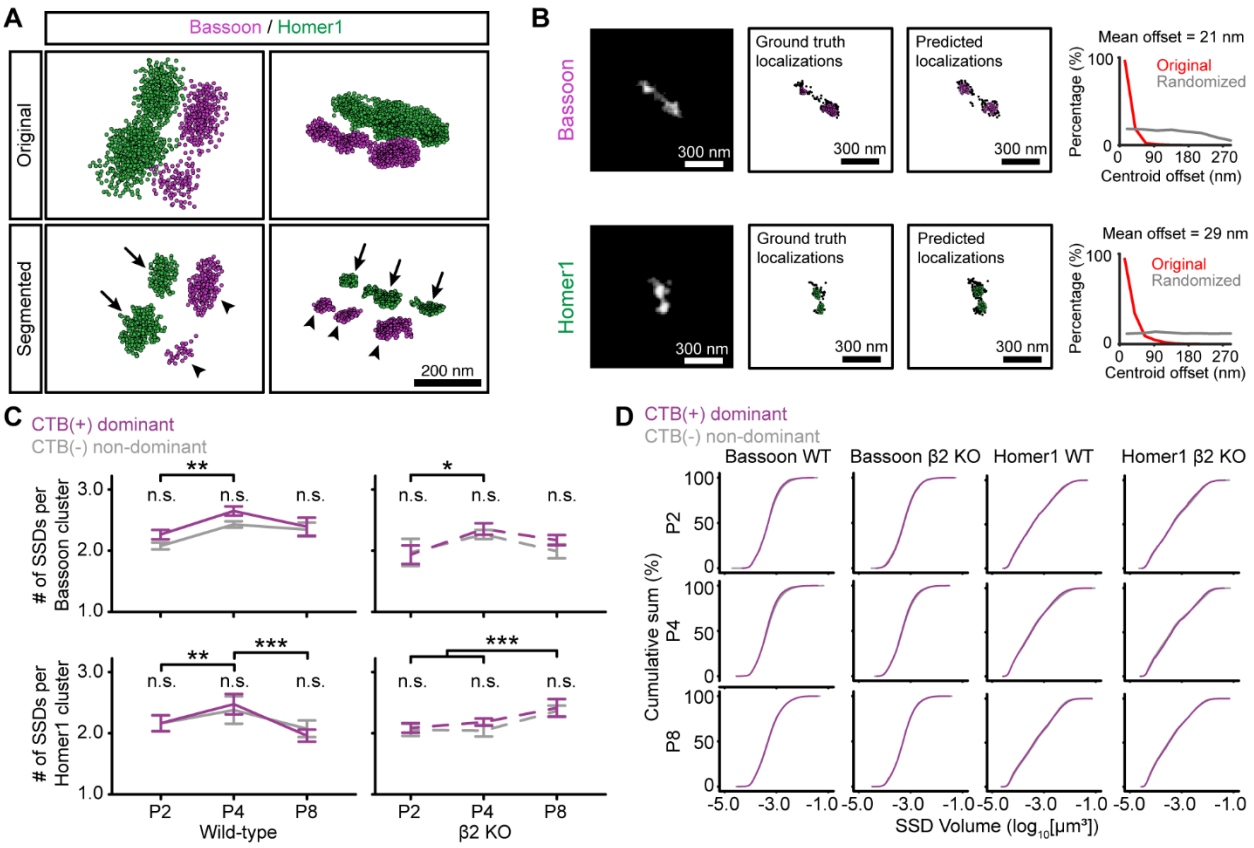


Figure 7.4 Activity-dependent SSD development from localization-based analysis, related to Figure 2.4.

(A) Subsynaptic domain (SSD) identification in the localization-based analysis. Single-molecule localizations (individual dots) within each retinogeniculate synapse were predicted using a deep learning-based method (top panels, see STAR Methods). SSDs were identified by density-based spatial clustering of applications with noise (DBSCAN) analysis of Bassoon (magenta, arrowheads) and Homer1 (green, arrows) localizations. Representative synapses are the same as those shown in Figure 2.4A.

(B) Validation of SSD identification using CNN-predicted single molecule distributions. Bassoon (top panels) and Homer1 (bottom panels) clusters were randomly selected from the WT P8 dataset. Representative 2D cluster images (single 70 nm sections) are shown in grayscale and their

corresponding ground truth and CNN-predicted localizations are shown as dots on the right of each image. Single-molecule localizations within identified SSDs are shown as colored dots. SSDs identified in ground truth localizations and predicted localizations were paired by their weighted centroid position (see chapter 2). The right panels show the distribution of paired SSD weighted centroid offsets (linear distance measurement, red lines) between the two datasets (mean offsets were ~21 and 29 nm for Bassoon/Homer1 respectively). The paired SSD offsets were significantly smaller than randomized controls in which postsynaptic SSD positions were generated by random centroid assignment within the predicted localization distribution.

(C) Changes in the average number of SSDs per synaptic cluster during development in localization-based analysis. The line graphs show the SSD number in Bassoon (top panels) and Homer1 (bottom panels) in WT (left panels) and β2KO (right panels) mice over development. Purple lines show CTB(+) dominant-eye synapses while gray lines show CTB(-) non-dominant-eye synapses. Error bars reflect means ± SEM from N = 3 biological replicates imaged in the contralateral ROI. Statistical analysis was performed using a one-way ANOVA with a post-hoc Tukey's test. *P < 0.05, **P < 0.01. ***P < 0.001. "n.s." = not significant.

(D) Eye-specific comparison of Bassoon and Homer1 SSD volume in localization-based analysis. Cumulative sum distributions are shown for CTB(+) (purple lines) and CTB(-) (gray lines) eye-specific clusters. Plots show WT Bassoon (first column), β2KO Bassoon (second column), WT Homer1 (third column), and β2KO Homer1 (fourth column) as a function of age (rows). Statistical analysis was performed using a mixed model ANOVA where the eye-of-origin was the fixed main factor, and the biological replicate ID was a random nested factor. There were no significant eye-specific differences in SSD volume for Bassoon or Homer1 as a function of age or genotype.

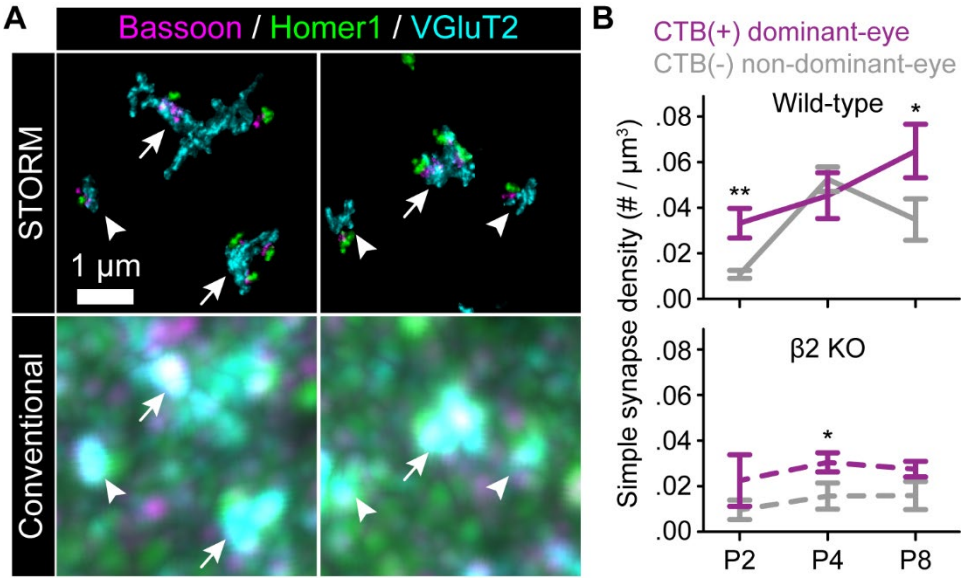


Figure 7.5 Eye-specific differences in simple synapse density in the first postnatal week, related to Figure 3.1.

(A) Volumetric STORM imaging enables the differentiation of complex (arrows) versus simple (arrowheads) synapses (top panels), which cannot be distinguished in diffraction-limited conventional images (bottom panels).

(B) The density of eye-specific simple synapses across ages in WT (top panel) and β2 KO mice (bottom panel). Error bars represent means ± SEMs (N=3 biological replicates for each age/genotype). Statistical tests were performed using a one-way ANOVA. *: P<0.05. **: p<0.01.

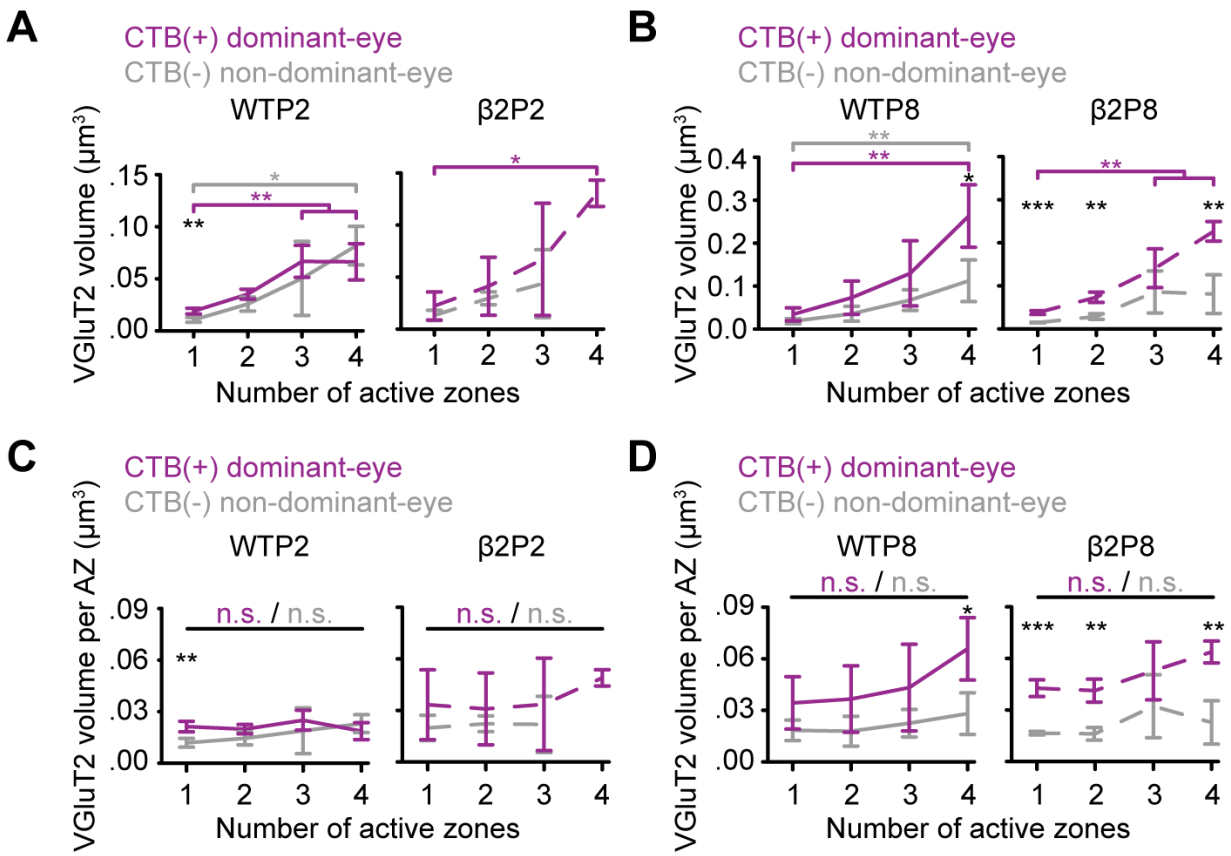


Figure 7.6 Complex synapses undergo eye-specific vesicle pool maturation, related to Figure 3.2.

(A-B) VGluT2 cluster volume relative to AZ number for each synapse in WT (left panels) and β2KO mice (right panels) at P2 (A) and P8 (B). Error bars indicate means ± SEMs (N=3 biological replicates for each age and genotype). A one-way ANOVA was used to assess statistical significance between eye-of-origin (black asterisks) and eye-specific synapses with different AZ numbers (colored asterisks). A post hoc Tukey's test was conducted for pairwise comparisons between simple (1 AZ) and complex (>1 AZ) synapses.

(C-D) VGluT2 volume per AZ (bassoon cluster) for all synapses in WT (left panels) and β2KO mice (right panels) at P2 (C) and P8 (D). Figure presentation and statistical tests were the same as shown in (A) and (B). In all panels: *: $p<0.05$; **:$p<0.01$; ***:$p<0.001$.

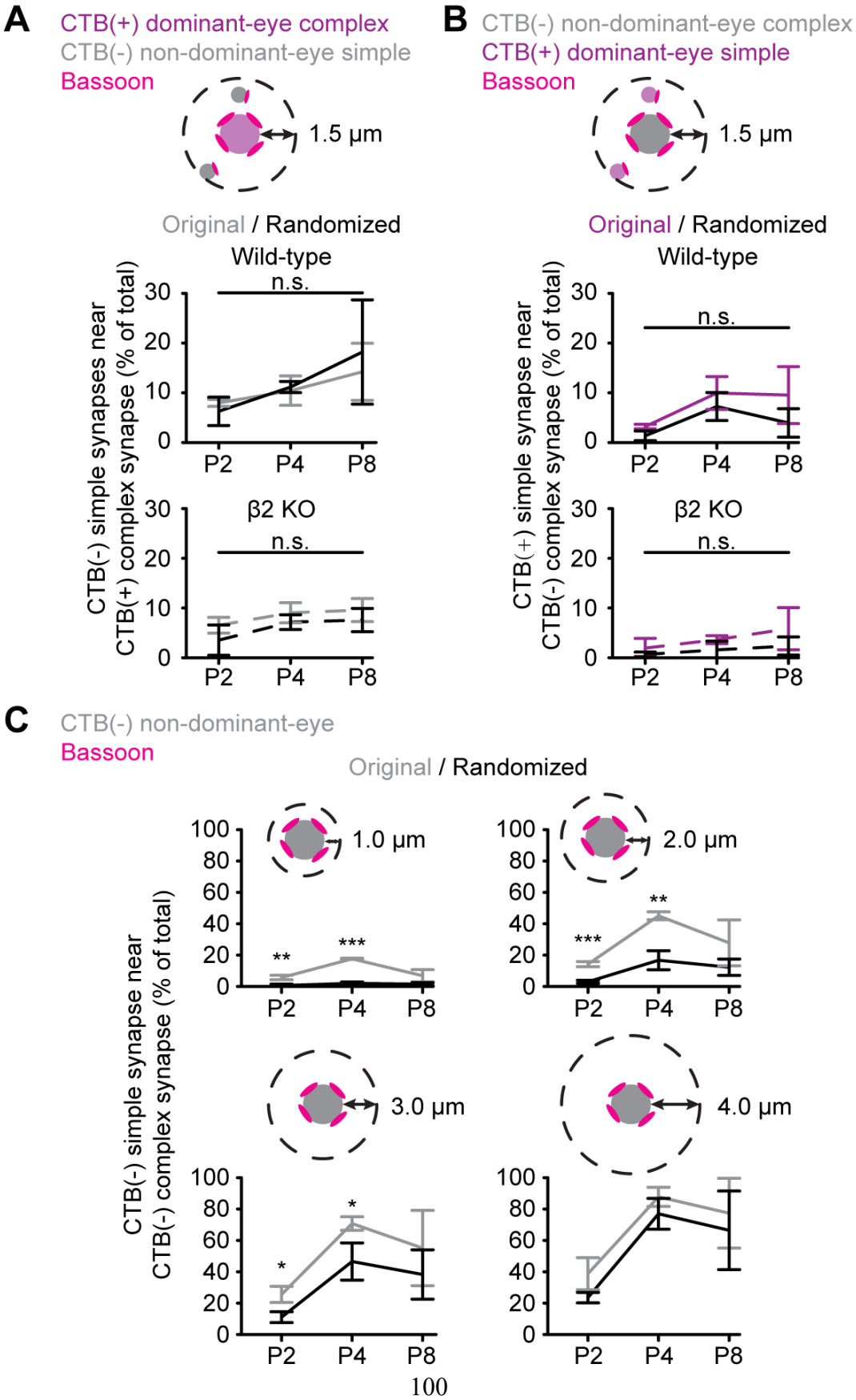

A
CTB(+) dominant-eye complex
CTB(-) non-dominant-eye simple
Bassoon
1.5 µm
Original / Randomized
Wild-type
n.s.
CTB(-) simple synapses near
CTB(+) complex synapse (% of total)
β2 KO
n.s.
P2
P4
P8
B
CTB(-) non-dominant-eye complex
CTB(+) dominant-eye simple
Bassoon
1.5 µm
Original / Randomized
Wild-type
n.s.
CTB(+) simple synapse near
CTB(-) complex synapse (% of total)
β2 KO
n.s.
C
CTB(-) non-dominant-eye
Bassoon
Original / Randomized
1.0 µm
2.0 µm
3.0 µm
4.0 µm
CTB(-) simple synapse near
CTB(-) complex synapse (% of total)

Figure 7.7 Complex synapses are loci for synaptic clustering, related to Figure 3.3.

(A) Percentage of CTB(-) non-dominant-eye simple synapses near an opposite-eye complex synapse in WT (top panel) and β2KO mice (bottom panel).

(B) Same presentation as in (A), showing the percentage of CTB(+) dominant-eye simple synapses near an opposite-eye complex synapse.

(C) To further validate our selection of a 1.5 um search radius, we performed additional control measurements with varying local search radii. For complex synapses of both eyes-of-origin, the detection of non-random clustering increased when the search radius was expanded from 1 μm to 2 μm and then decreased as the radius was further expanded to sample the average simple synapse density (3-4 μm) (example with CTB(-) non-dominant-eye synapses). The figure shows the percentage of CTB(-) non-dominant-eye simple synapses near like-type CTB(-) complex synapses across development as a function of increasing distance cutoffs from the surface of complex synapses. Distributions are shown for cutoff distances of 1.0 μm (top left panel), 2.0 μm (top right panel), 3.0 μm (bottom left panel), and 4.0 μm (bottom right panel). For all panels, grey and purple lines represent the original data, and black lines represent the results from a randomized simple synapse distribution. Error bars represent means ± SEMs (N=3 biological replicates for each age and genotype). Statistical tests between original and randomized data were performed using one-way ANOVA. *: $P<0.05$; **: $p<0.01$; ***: $p<0.001$. “n.s.” indicates no significant differences.

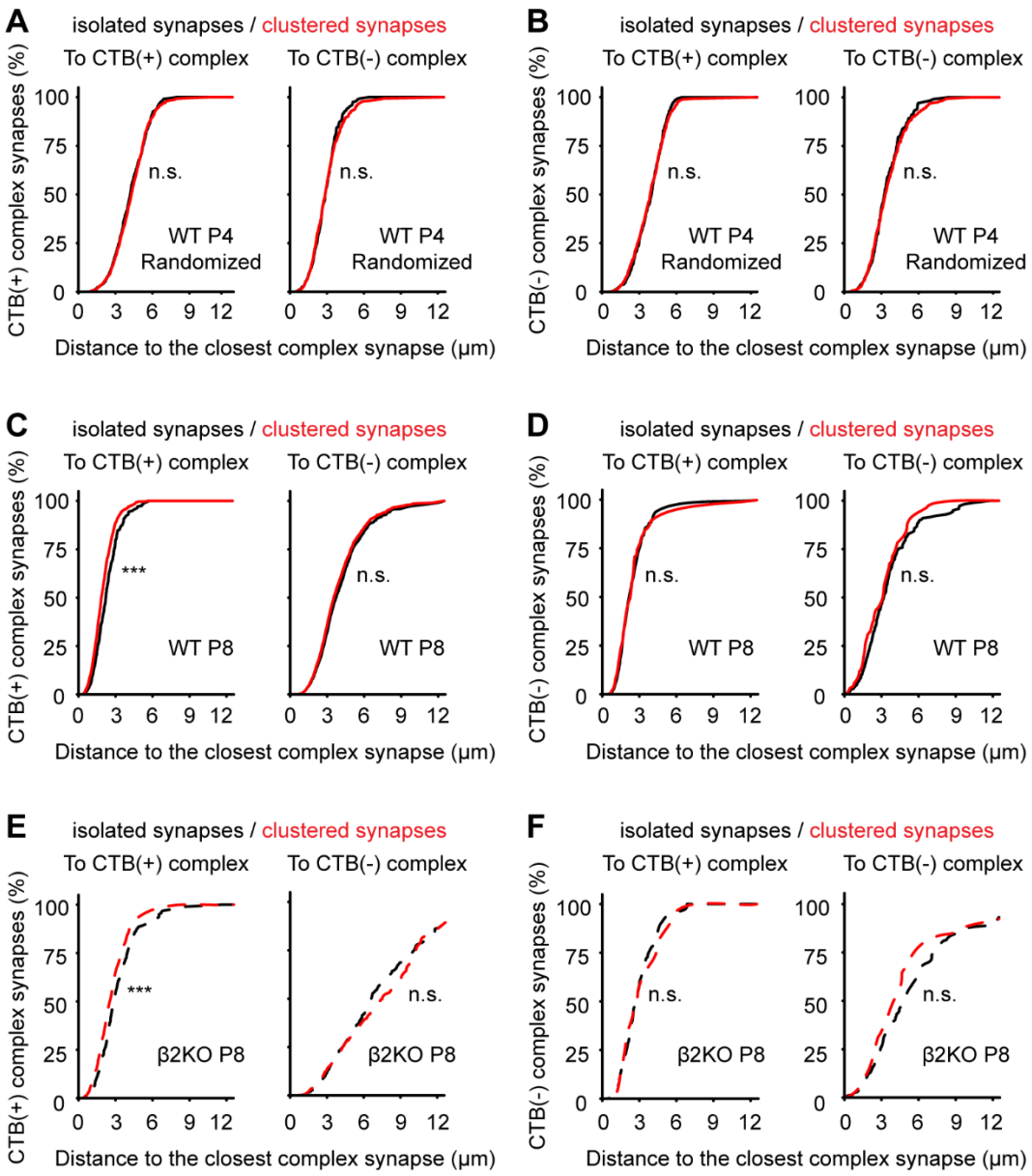


Figure 7.8 Complex synapses mediate distance-dependent synaptic stabilization and punishment underlying eye-specific competition, related to Figure 3.4.

(A) Cumulative histogram of the distances from CTB(+) complex synapses to their nearest CTB(+) (left panel) and CTB(-) (right panel) complex synapse in P4 WT data where simple synapse distributions were randomized. Black lines show distributions for isolated complex synapses with

no nearby (<1.5 μm) simple synapses and red lines show distributions for clustered complex synapses with one or more simple synapses nearby.

(B) Same presentation as in (A), showing distances from CTB(-) complex synapses to their nearest CTB(+) (left panel) and CTB(-) (right panel) complex synapse in P4 WT randomized data.

(C and D) Same presentation as in A/B, showing WT P8 original data. (E and F) Same presentation as in C/D, showing β2KO P8 original data. Nonparametric Kolmogorov-Smirnov tests were used for statistical comparisons (N=3 biological replicates for each condition). ***: $p<0.001$. "n.s." indicates no significant differences.

Bibliography

Ackman, J. B., & Crair, M. C. (2014). Role of emergent neural activity in visual map development. *Current Opinion in Neurobiology*, *24*(1), 166–175. https://doi.org/10.1016/J.CONB.2013.11.011

Altimus, C. M., Güler, A. D., Alam, N. M., Arman, A. C., Prusky, G. T., Sampath, A. P., & Hattar, S. (2010). Rod photoreceptors drive circadian photoentrainment across a wide range of light intensities. *Nature Neuroscience*, *13*(9), 1107–1112. https://doi.org/10.1038/nn.2617

Aranda, M. L., & Schmidt, T. M. (2021). Diversity of intrinsically photosensitive retinal ganglion cells : circuits and functions. *Cellular and Molecular Life Sciences*, *78*(3), 887–907. https://doi.org/10.1007/s00018-020-03641-5

Arroyo, D. A., & Feller, M. B. (2016). Spatiotemporal Features of Retinal Waves Instruct the Wiring of the Visual Circuitry. *Frontiers in Neural Circuits*, *10*(JUL2016), 54. https://doi.org/10.3389/fncir.2016.00054

Assali, A., Gaspar, P., & Rebsam, A. (2014). Activity dependent mechanisms of visual map formation - From retinal waves to molecular regulators. *Seminars in Cell and Developmental Biology*, *35*, 136–146. https://doi.org/10.1016/j.semcdb.2014.08.008

Assali, A., Le Magueresse, C., Bennis, M., Nicol, X., Gaspar, P., & Rebsam, A. (2017). RIM1/2 in retinal ganglion cells are required for the refinement of ipsilateral axons and eye-specific segregation. *Scientific Reports*, *7*(1), 1–11. https://doi.org/10.1038/s41598-017-03361-0

Babcock, H., Sigal, Y. M., & Zhuang, X. (2012). A high-density 3D localization algorithm for stochastic optical reconstruction microscopy. *Optical Nanoscopy*, *1*(1), 1–10. https://doi.org/10.1186/2192-2853-1-6

Balice-Gordon, R. J., Chua, C. K., Nelson, C. C., & Lichtman, J. W. (1993). Gradual Loss of synaptic Cartels precedes axon withdrawal at developing neuromuscular junctions. *Neuron*, *11*, 801–815. https://doi.org/10.1016/0896-6273(93)90110-D

Balice-Gordon, R. J., & Lichtman, J. W. (1994). Long-term synapse loss induced by focal blockade of postsynaptlc receptors. *Nature*, *372*(6506), 519–524. https://doi.org/10.1038/372519a0

Bansal, A., Singer, J. H., Hwang, B. J., Xu, W., Beaudet, A., & Feller, M. B. (2000). Mice lacking specific nicotinic acetylcholine receptor subunits exhibit dramatically altered spontaneous activity patterns and reveal a limited role for retinal waves in forming ON and OFF circuits in the inner retina. *Journal of Neuroscience*, *20*(20), 7672–7681. https://doi.org/10.1523/jneurosci.20-20-07672.2000

Bauer, J., Weiler, S., Fernholz, M. H. P., Laubender, D., Scheuss, V., Hübener, M., Bonhoeffer, T., & Rose, T. (2021). Limited functional convergence of eye-specific inputs in the retinogeniculate pathway of the mouse. *Neuron*, *109*(15), 2457-2468.e12. https://doi.org/10.1016/j.neuron.2021.05.036

Bedont, J. L., & Blackshaw, S. (2015). Constructing the suprachiasmatic nucleus: a watchmaker's perspective on the central clockworks. *Frontiers in Systems Neuroscience*, *9*(MAY), 1–21. https://doi.org/10.3389/fnsys.2015.00074

Bickford, M. E. (2019). Synaptic organization of the dorsal lateral geniculate nucleus. *European Journal of Neuroscience*, *49*(7), 938–947. https://doi.org/10.1111/ejn.13917

Bickford, M. E., Slusarczyk, A., Dilger, E. K., Krahe, T. E., Kucuk, C., & Guido, W. (2010). Synaptic development of the mouse dorsal lateral geniculate nucleus. *Journal of Comparative Neurology*, *518*(5), 622–635. https://doi.org/10.1002/cne.22223

Binzegger, T., Douglas, R. J., & Martin, K. A. C. (2007). Stereotypical bouton clustering of individual neurons in cat primary visual cortex. *Journal of Neuroscience*, *27*(45), 12242–12254. https://doi.org/10.1523/JNEUROSCI.3753-07.2007

Blank, H., Anwander, A., & von Kriegstein, K. (2011). Direct Structural Connections between Voice- and Face-Recognition Areas. *Journal of Neuroscience*, *31*(36), 12906–12915. https://doi.org/10.1523/JNEUROSCI.2091-11.2011

Buffelli, M., Burgess, R. W., Feng, G., Lobe, C. G., Lichtman, J. W., & Sanes, J. R. (2003). Genetic evidence that relative synaptic efficacy biases the outcome of synaptic competition. *Nature*, *424*(6947), 430–434. https://doi.org/10.1038/nature01844

Bury, L. A. D., & Sabo, S. L. (2016). Building a Terminal: Mechanisms of Presynaptic Development in the CNS. *Neuroscientist*, *22*(4), 372–391. https://doi.org/10.1177/1073858415596131

Butts, D. A., Weng, C., Jin, J., Yeh, C. I., Lesica, N. A., Alonso, J. M., & Stanley, G. B. (2007). Temporal precision in the neural code and the timescales of natural vision. *Nature*, *449*(7158), 92–95. https://doi.org/10.1038/nature06105

Calligaro, H., Shoghi, A., Xinyue, C., Keun-Young, K., Liu, Y. H., Brian, K., Benjamin, F., Hiep, L., Mark, E., & Satchidananda, P. (2022). Ultrastructure of synaptic connectivity within sub-regions of the SCN revealed by genetically encoded EM tag and SBEM. *BioRxiv*, 1–23. https://medium.com/@arifwicaksanaa/pengertian-use-case-a7e576e1b6bf

Campbell, G., & Shatz, C. J. (1992). Synapses formed by identified retinogeniculate axons during the segregation of eye input. *The Journal of Neuroscience*, *12*(5), 1847–1858. https://doi.org/10.1523/JNEUROSCI.12-05-01847.1992

Chandrasekaran, A. R., Shah, R. D., & Crair, M. C. (2007). Developmental homeostasis of mouse retinocollicular synapses. *Journal of Neuroscience*, *27*(7), 1746–1755. https://doi.org/10.1523/JNEUROSCI.4383-06.2007

Chen, C., & Regehr, W. G. (2000). Developmental remodeling of the retinogeniculate synapse. *Neuron*, *28*(3), 955–966. https://doi.org/10.1016/S0896-6273(00)00166-5

Chen, H., Tang, A.-H., & Blanpied, T. A. (2018). Subsynaptic spatial organization as a regulator of synaptic strength and plasticity. *Current Opinion in Neurobiology*, *51*, 147–153. https://doi.org/10.1016/j.conb.2018.05.004

Chenouard, N., Xuan, F., & Tsien, R. W. (2020). Synaptic vesicle traffic is supported by transient actin filaments and regulated by PKA and NO. *Nature Communications 2020 11:1*, *11*(1), 1–16. https://doi.org/10.1038/s41467-020-19120-1

Chew, K. S., Renna, J. M., McNeill, D. S., Fernandez, D. C., Keenan, W. T., Thomsen, M. B., Ecker, J. L., Loevinsohn, G. S., Vandunk, C., Vicarel, D. C., Tufford, A., Weng, S., Gray, P. A., Cayouette, M., Herzog, E. D., Zhao, H., Berson, D. M., & Hattar, S. (2017). A subset of iprgcs regulates both maturation of the circadian clock and segregation of retinogeniculate projections in mice. *ELife*, *6*. https://doi.org/10.7554/ELIFE.22861

Chung, W. S., Clarke, L. E., Wang, G. X., Stafford, B. K., Sher, A., Chakraborty, C., Joung, J., Foo, L. C., Thompson, A., Chen, C., Smith, S. J., & Barres, B. A. (2013). Astrocytes mediate synapse elimination through MEGF10 and MERTK pathways. *Nature*, *504*(7480), 394–400. https://doi.org/10.1038/nature12776

Cong, Q., Soteros, B. M., Wollet, M., Kim, J. H., & Sia, G. M. (2020). The endogenous neuronal complement inhibitor SRPX2 protects against complement-mediated synapse elimination during development. *Nature Neuroscience 2020 23:9*, *23*(9), 1067–1078. https://doi.org/10.1038/s41593-020-0672-0

Cook, P. M., Prusky, G., & Ramoa, A. S. (1999). The role of spontaneous retinal activity before eye opening in the maturation of form and function in the retinogeniculate pathway of the ferret. *Visual Neuroscience*, *16*(3), 491–501. https://doi.org/10.1017/S0952523899163107

Dankovich, T. M., & Rizzoli, S. O. (2021). Challenges facing quantitative large-scale optical super-resolution, and some simple solutions. *IScience*, *24*(3), 102134. https://doi.org/10.1016/J.ISCI.2021.102134

Datwani, A., McConnell, M. J., Kanold, P. O., Micheva, K. D., Busse, B., Shamloo, M., Smith, S. J., & Shatz, C. J. (2009). Classical MHCI Molecules Regulate Retinogeniculate Refinement and Limit Ocular Dominance Plasticity. *Neuron*, *64*(4), 463–470. https://doi.org/10.1016/j.neuron.2009.10.015

De Boer, P., Hoogenboom, J. P., & Giepmans, B. N. G. (2015). Correlated light and electron microscopy: ultrastructure lights up! *Nature Methods 2015 12:6*, *12*(6), 503–513. https://doi.org/10.1038/nmeth.3400

Demas, J., Sagdullaev, B. T., Green, E., Jaubert-Miazza, L., McCall, M. A., Gregg, R. G., Wong, R. O. L., & Guido, W. (2006). Failure to Maintain Eye-Specific Segregation in nob, a Mutant with Abnormally Patterned Retinal Activity. *Neuron*, *50*(2), 247–259. https://doi.org/10.1016/j.neuron.2006.03.033

Dempsey, G. T., Vaughan, J. C., Chen, K. H., Bates, M., & Zhuang, X. (2011). Evaluation of fluorophores for optimal performance in localization-based super-resolution imaging. *Nature Methods*, *8*(12), 1027–1040. https://doi.org/10.1038/nmeth.1768

Denker, A., Kröhnert, K., Bückers, J., Neher, E., & Rizzoli, S. O. (2011). The reserve pool of synaptic vesicles acts as a buffer for proteins involved in synaptic vesicle recycling. *Proceedings of the National Academy of Sciences of the United States of America*, *108*(41), 17183–17188. https://doi.org/10.1073/PNAS.1112690108/SUPPL_FILE/PNAS.201112690SI.PDF

Dhande, O. S., Bhatt, S., Anishchenko, A., Elstrott, J., Iwasato, T., Swindell, E. C., Xu, H. P., Jamrich, M., Itohara, S., Feller, M. B., & Crair, M. C. (2012). Role of adenylate cyclase 1 in retinofugal map development. *Journal of Comparative Neurology*, *520*(7), 1562–1583. https://doi.org/10.1002/cne.23000

Dhande, O. S., Hua, E. W., Guh, E., Yeh, J., Bhatt, S., Zhang, Y., Ruthazer, E. S., Feller, M. B., & Crair, M. C. (2011). Development of single retinofugal axon arbors in normal and β2 knock-out mice. *Journal of Neuroscience*, *31*(9), 3384–3399. https://doi.org/10.1523/JNEUROSCI.4899-10.2011

Dilger, E. K., Krahe, T. E., Morhardt, D. R., Seabrook, T. A., Shin, H. S., & Guido, W. (2015). Absence of plateau potentials in dLGN cells leads to a breakdown in retinogeniculate refinement. *Journal of Neuroscience*, *35*(8), 3652–3662. https://doi.org/10.1523/JNEUROSCI.2343-14.2015

El-Danaf, R. N., Krahe, T. E., Dilger, E. K., Bickford, M. E., Fox, M. A., & Guido, W. (2015). Developmental remodeling of relay cells in the dorsal lateral geniculate nucleus in the absence of retinal input. *Neural Development*, *10*(1), 1–17. https://doi.org/10.1186/s13064-015-0046-6

Ellis, E. M., Gauvain, G., Sivyer, B., & Murphy, G. J. (2016). Shared and distinct retinal input to the mouse superior colliculus and dorsal lateral geniculate nucleus. *Journal of Neurophysiology*, *116*(2), 602–610. https://doi.org/10.1152/jn.00227.2016

Failor, S., Chapman, B., & Cheng, H. J. (2015). Retinal waves regulate afferent terminal targeting in the early visual pathway. *Proceedings of the National Academy of Sciences of the United States of America*, *112*(22), E2957–E2966. https://doi.org/10.1073/pnas.1506458112

Fassier, C., & Nicol, X. (2021). Retinal Axon Interplay for Binocular Mapping. *Frontiers in Neural Circuits*, *15*, 49. https://doi.org/10.3389/fncir.2021.679440

Faust, T. E., Gunner, G., & Schafer, D. P. (2021). Mechanisms governing activity-dependent synaptic pruning in the developing mammalian CNS. *Nature Reviews Neuroscience 2021 22:11*, *22*(11), 657–673. https://doi.org/10.1038/s41583-021-00507-y

Feldman, D. E. (2012). The Spike-Timing Dependence of Plasticity. *Neuron*, *75*(4), 556–571. https://doi.org/10.1016/j.neuron.2012.08.001

Fredj, N. Ben, Hammond, S., Otsuna, H., Chien, C. Bin, Burrone, J., & Meyer, M. P. (2010). Synaptic activity and activity-dependent competition regulates axon arbor maturation, growth arrest, and territory in the retinotectal projection. *Journal of Neuroscience*, *30*(32), 10939–10951. https://doi.org/10.1523/JNEUROSCI.1556-10.2010

Fu, M., Yu, X., Lu, J., & Zuo, Y. (2012). Repetitive motor learning induces coordinated formation of clustered dendritic spines in vivo. *Nature*, *483*(7387), 92–96. https://doi.org/10.1038/nature10844

Fujiyama, F., Hioki, H., Tomioka, R., Taki, K., Tamamaki, N., Nomura, S., Okamoto, K., & Kaneko, T. (2003). Changes of immunocytochemical localization of vesicular glutamate transporters in the rat visual system after the retinofugal denervation. *The Journal of Comparative Neurology*, *465*(2), 234–249. https://doi.org/10.1002/CNE.10848

Furman, M., & Crair, M. C. (2012). Synapse maturation is enhanced in the binocular region of the retinocollicular map prior to eye opening. *Journal of Neurophysiology*, *107*(11), 3200–3216. https://doi.org/10.1152/jn.00943.2011

Furman, M., Xu, H. P., & Crair, M. C. (2013). Competition driven by retinal waves promotes morphological and functional synaptic development of neurons in the superior colliculus. *Journal of Neurophysiology*, *110*(6), 1441–1454. https://doi.org/10.1152/jn.01066.2012

Gan, W. B., & Lichtman, J. W. (1998). Synaptic segregation at the developing neuromuscular junction. *Science*, *282*(5393), 1508–1511. https://doi.org/10.1126/science.282.5393.1508

García-Frigola, C., & Herrera, E. (2010). Zic2 regulates the expression of Sert to modulate eye-specific refinement at the visual targets. *The EMBO Journal*, *29*(18), 3170–3183. https://doi.org/10.1038/emboj.2010.172

Ge, X., Zhang, K., Gribizis, A., Hamodi, A. S., Sabino, A. M., & Crair, M. C. (2021). Retinal waves prime visual motion detection by simulating future optic flow. *Science*, *373*(6553). https://doi.org/10.1126/science.abd0830

Godement, P., Salaün, J., & Imbert, M. (1984). Prenatal and postnatal development of retinogeniculate and retinocollicular projections in the mouse. *Journal of Comparative Neurology*, *230*(4), 552–575. https://doi.org/10.1002/cne.902300406

González-Mariscal, G., Caba, M., Martínez-Gómez, M., Bautista, A., & Hudson, R. (2016). Mothers and offspring: The rabbit as a model system in the study of mammalian maternal behavior and sibling interactions. *Hormones and Behavior*, *77*, 30–41. https://doi.org/10.1016/j.yhbeh.2015.05.011

Govindaiah, G., Campbell, P. W., & Guido, W. (2020). Differential Distribution of Ca2+ Channel Subtypes at Retinofugal Synapses. *ENeuro*, *7*(6), 1–8. https://doi.org/10.1523/ENEURO.0293-20.2020

Göz, D., Studholme, K., Lappi, D. A., Rollag, M. D., Provencio, I., & Morin, L. P. (2008). Targeted destruction of photosensitive retinal ganglion cells with a saporin conjugate alters the effects of light on mouse circadian rhythms. *PLoS ONE*, *3*(9). https://doi.org/10.1371/journal.pone.0003153

Grubb, M. S., Rossi, F. M., Changeux, J. P., & Thompson, I. D. (2003). Abnormal functional organization in the dorsal lateral geniculate nucleus of mice lacking the β2 subunit of the nicotinic acetylcholine receptor. *Neuron*, *40*(6), 1161–1172. https://doi.org/10.1016/S0896-6273(03)00789-X

Grubb, M. S., & Thompson, I. D. (2004). The influence of early experience on the development of sensory systems. In *Current Opinion in Neurobiology* (Vol. 14, Issue 4, pp. 503–512). Elsevier Current Trends. https://doi.org/10.1016/j.conb.2004.06.006

Guedes-Dias, P., & Holzbaur, E. L. F. (2019). Axonal transport: Driving synaptic function. *Science*, *366*(6462). https://doi.org/10.1126/science.aaw9997

Guido, W. (2018). Development, form, and function of the mouse visual thalamus. *Journal of Neurophysiology*, *120*(1), 211–225. https://doi.org/10.1152/JN.00651.2017

Hammer, S., Carrillo, G. L., Govindaiah, G., Monavarfeshani, A., Bircher, J. S., Su, J., Guido, W., & Fox, M. A. (2014). Nuclei-specific differences in nerve terminal distribution, morphology, and development in mouse visual thalamus. *Neural Development*, *9*(1), 1–21. https://doi.org/10.1186/1749-8104-9-16

Hammer, S., Monavarfeshani, A., Lemon, T., Su, J., & Fox, M. A. (2015). Multiple Retinal Axons Converge onto Relay Cells in the Adult Mouse Thalamus. *Cell Reports*, *12*(10), 1575–1583. https://doi.org/10.1016/j.celrep.2015.08.003

Han, Y., Kaeser, P. S., Südhof, T. C., & Schneggenburger, R. (2011). RIM determines Ca2+ channel density and vesicle docking at the presynaptic active zone. *Neuron*, *69*(2), 304–316. https://doi.org/10.1016/j.neuron.2010.12.014

Hatori, M., Le, H., Vollmers, C., Keding, S. R., Tanaka, N., Schmedt, C., Jegla, T., & Panda, S. (2008). Inducible ablation of melanopsin-expressing retinal ganglion cells reveals their central role in non-image forming visual responses. *PLoS ONE*, *3*(6). https://doi.org/10.1371/journal.pone.0002451

Hayashi, M. K., Tang, C., Verpelli, C., Narayanan, R., Stearns, M. H., Xu, R. M., Li, H., Sala, C., & Hayashi, Y. (2009). The postsynaptic density proteins Homer and Shank form a polymeric network structure. *Cell*, *137*(1), 159. https://doi.org/10.1016/J.CELL.2009.01.050

Hedrick, N. G., Lu, Z., Bushong, E., Singhi, S., Nguyen, P., Magaña, Y., Jilani, S., Lim, B. K., Ellisman, M., & Komiyama, T. (2022). Learning binds new inputs into functional synaptic clusters via spinogenesis. *Nature Neuroscience*, *25*(6), 726–737. https://doi.org/10.1038/s41593-022-01086-6

Heiligenstein, X., & Lucas, M. S. (2022). One for All, All for One: A Close Look at In-Resin Fluorescence Protocols for CLEM. *Frontiers in Cell and Developmental Biology*, *10*, 1369. https://doi.org/10.3389/FCELL.2022.866472/BIBTEX

Hetsch, F., Wang, D., Chen, X., Zhang, J., Aslam, M., Kegel, M., Tonner, H., Grus, F., & von Engelhardt, J. (2022). CKAMP44 controls synaptic function and strength of relay neurons during early development of the dorsal lateral geniculate nucleus. *Journal of Physiology*, *600*(15), 3549–3565. https://doi.org/10.1113/JP283172

Hong, Y. K., Park, S. H., Litvina, E. Y., Morales, J., Sanes, J. R., & Chen, C. (2014). Refinement of the Retinogeniculate Synapse by Bouton Clustering. *Neuron*, *84*(2), 332–339. https://doi.org/10.1016/j.neuron.2014.08.059

Hu, J., Shi, Y., Zhang, J., Huang, X., Wang, Q., Zhao, H., Shen, J., Chen, Z., Song, W., Zheng, P., Zhan, S., Sun, Y., Cai, P., An, K., Ouyang, C., Zhao, B., Zhou, Q., Xu, L., Xiong, W., … Xue, T. (2022). Melanopsin retinal ganglion cells mediate light-promoted brain development. *Cell*, *185*(17), 3124-3137.e15. https://doi.org/10.1016/j.cell.2022.07.009

Hua, J. Y., Smear, M. C., Baier, H., & Smith, S. J. (2005). Regulation of axon growth in vivo by activity-based competition. *Nature*, *434*(7036), 1022–1025. https://doi.org/10.1038/nature03409

Huberman, A. D., Stellwagen, D., & Chapman, B. (2002). Decoupling Eye-Specific Segregation from Lamination in the Lateral Geniculate Nucleus. *Journal of Neuroscience*, *22*(21), 9419–9429. https://doi.org/10.1523/JNEUROSCI.22-21-09419.2002

Huberman, A. D., Wang, G. Y., Liets, L. C., Collins, O. A., Chapman, B., & Chalupa, L. M. (2003). Eye-specific retinogenicu late segregation independent of normal neuronal activity. *Science*, *300*(5621), 994–998. https://doi.org/10.1126/SCIENCE.1080694/SUPPL_FILE/HUBERMAN.SOM.PDF

Jähne, S., Mikulasch, F., Heuer, H. G. H., Truckenbrodt, S., Agüi-Gonzalez, P., Grewe, K., Vogts, A., Rizzoli, S. O., & Priesemann, V. (2021). Presynaptic activity and protein turnover are correlated at the single-synapse level. *Cell Reports*, *34*(11), 108841. https://doi.org/10.1016/J.CELREP.2021.108841

Jaubert-Miazza, L., Green, E., Lo, F. S., Bui, K., Mills, J., & Guido, W. (2005). Structural and functional composition of the developing retinogeniculate pathway in the mouse. *Visual Neuroscience*, *22*(5), 661–676. https://doi.org/10.1017/S0952523805225154

Juárez, C., Morgado, E., Meza, E., Waliszewski, S. M., Aguilar-Roblero, R., & Caba, M. (2013). Development of retinal projections and response to photic input in the suprachiasmatic nucleus of New Zealand White Rabbits. *Brain Research*, *1499*, 21–28. https://doi.org/10.1016/j.brainres.2013.01.010

Kaeser, P. S., & Regehr, W. G. (2017). The readily releasable pool of synaptic vesicles. In *Current Opinion in Neurobiology* (Vol. 43, pp. 63–70). Elsevier Current Trends. https://doi.org/10.1016/j.conb.2016.12.012

Kastellakis, G., & Poirazi, P. (2019). Synaptic Clustering and Memory Formation. *Frontiers in Molecular Neuroscience*, *12*(December), 1–13. https://doi.org/10.3389/fnmol.2019.00300

Kerschensteiner, D. (2016). Glutamatergic Retinal Waves. *Frontiers in Neural Circuits*, *10*(MAY), 1–7. https://doi.org/10.3389/fncir.2016.00038

KERSCHENSTEINER, D., & GUIDO, W. (2017). Organization of the dorsal lateral geniculate nucleus in the mouse. *Visual Neuroscience*, *34*, E008. https://doi.org/10.1017/S0952523817000062

Kim, K. Y., Rios, L. C., Le, H., Perez, A. J., Phan, S., Bushong, E. A., Deerinck, T. J., Liu, Y. H., Ellisman, M. A., Lev-Ram, V., Ju, S., Panda, S. A., Yoon, S., Hirayama, M., Mure, L. S., Hatori, M., Ellisman, M. H., & Panda, S. (2019). Synaptic Specializations of Melanopsin-Retinal Ganglion Cells in Multiple Brain Regions Revealed by Genetic Label for Light and Electron Microscopy. *Cell Reports*, *29*(3), 628-644.e6. https://doi.org/10.1016/j.celrep.2019.09.006

Kirchner, J. H., & Gjorgjieva, J. (2021). Emergence of local and global synaptic organization on cortical dendrites. *Nature Communications*, *12*(1). https://doi.org/10.1038/s41467-021-23557-3

Kirchner, J. H., & Gjorgjieva, J. (2022). Emergence of synaptic organization and computation in dendrites. *Neuroforum*, *28*(1), 21–30. https://doi.org/10.1515/nf-2021-0031

Kirkby, L. A., Sack, G. S., Firl, A., & Feller, M. B. (2013). A role for correlated spontaneous activity in the assembly of neural circuits. *Neuron*, *80*(5), 1129–1144. https://doi.org/10.1016/J.NEURON.2013.10.030

Kleindienst, T., Winnubst, J., Roth-Alpermann, C., Bonhoeffer, T., & Lohmann, C. (2011). Activity-dependent clustering of functional synaptic inputs on developing hippocampal dendrites. *Neuron*, *72*(6), 1012–1024. https://doi.org/10.1016/j.neuron.2011.10.015

Koch, S. M., Dela Cruz, C. G., Hnasko, T. S., Edwards, R. H., Huberman, A. D., & Ullian, E. M. (2011). Pathway-Specific Genetic Attenuation of Glutamate Release Alters Select Features of Competition-Based Visual Circuit Refinement. *Neuron*, *71*(2), 235–242. https://doi.org/10.1016/j.neuron.2011.05.045

Kohansal-Nodehi, M., Chua, J. J. E., Urlaub, H., Jahn, R., & Czernik, D. (2016). Analysis of protein phosphorylation in nerve terminal reveals extensive changes in active zone proteins upon exocytosis. *ELife*, *5*(April2016), 1–25. https://doi.org/10.7554/eLife.14530

Kopp, D. M., Perkel, D. J., & Balice-Gordon, R. J. (2000). Disparity in neurotransmitter release probability among competing inputs during neuromuscular synapse elimination. *Journal of Neuroscience*, *20*(23), 8771–8779. https://doi.org/10.1523/jneurosci.20-23-08771.2000

Krahe, T. E., Seabrook, T. A., Chen, C. K. J., Fox, M. A., & Guido, W. (2012). Modulation of CREB in the dorsal lateral geniculate nucleus of dark-reared mice. *Neural Plasticity*, *2012*. https://doi.org/10.1155/2012/426437

Kutsarova, E., Schohl, A., Munz, M., Wang, A., Zhang, Y. Y., Bilash, O. M., & Ruthazer, E. S. (2023). BDNF signaling in correlation-dependent structural plasticity in the developing visual system. *PLoS Biology*, *21*(4), 1–24. https://doi.org/10.1371/journal.pbio.3002070

Land, P. W., Kyonka, E., & Shamalla-Hannah, L. (2004). Vesicular glutamate transporters in the lateral geniculate nucleus: expression of VGLUT2 by retinal terminals. *Brain Research*, *996*(2), 251–254. https://doi.org/10.1016/J.BRAINRES.2003.10.032

Lee, K. F. H., Soares, C., Thivierge, J. P., & Béïque, J. C. (2016). Correlated Synaptic Inputs Drive Dendritic Calcium Amplification and Cooperative Plasticity during Clustered Synapse Development. *Neuron*, *89*(4), 784–799. https://doi.org/10.1016/j.neuron.2016.01.012

Leighton, A. H., & Lohmann, C. (2016). The wiring of developing sensory circuits—From patterned spontaneous activity to synaptic plasticity mechanisms. *Frontiers in Neural Circuits*, *10*(SEP), 1–13. https://doi.org/10.3389/fncir.2016.00071

Lelek, M., Gyparaki, M. T., Beliu, G., Schueder, F., Griffié, J., Manley, S., Jungmann, R., Sauer, M., Lakadamyali, M., & Zimmer, C. (2021). Single-molecule localization microscopy. *Nature Reviews Methods Primers 2021 1:1*, *1*(1), 1–27. https://doi.org/10.1038/s43586-021-00038-x

Li, J.-D., Burton, K. J., Zhang, C., Hu, S.-B., & Zhou, Q.-Y. (2009). Vasopressin receptor V1a regulates circadian rhythms of locomotor activity and expression of clock-controlled genes in the suprachiasmatic nuclei. *American Journal of Physiology - Regulatory, Integrative and Comparative Physiology*, *296*(3), R824. https://doi.org/10.1152/AJPREGU.90463.2008

Liang, L., Fratzl, A., Goldey, G., Ramesh, R. N., Sugden, A. U., Morgan, J. L., Chen, C., & Andermann, M. L. (2018). A Fine-Scale Functional Logic to Convergence from Retina to Thalamus. *Cell*, *173*(6), 1343-1355.e24. https://doi.org/10.1016/J.CELL.2018.04.041

Lichter, K., Paul, M. M., Pauli, M., Schoch, S., Kollmannsberger, P., Stigloher, C., Heckmann, M., & Sirén, A. L. (2022). Ultrastructural analysis of wild-type and RIM1α knockout active zones in a large cortical synapse. *Cell Reports*, *40*(12). https://doi.org/10.1016/j.celrep.2022.111382

Lin, S. L., Setya, S., Johnson-Farley, N. N., & Cowen, D. S. (2002). Differential coupling of 5-HT 1 receptors to G proteins of the G i family. *British Journal of Pharmacology*, *136*(7), 1072–1078. https://doi.org/10.1038/sj.bjp.0704809

Ling, C., Schneider, G. E., & Jhaveri, S. (1998). Target-specific morphology of retinal axon arbors in the adult hamster. *Visual Neuroscience*, *15*(3), 559–579. https://doi.org/10.1017/S0952523898153178

Litvina, E. Y., & Chen, C. (2017). Functional Convergence at the Retinogeniculate Synapse. *Neuron*, *96*(2), 330-338.e5. https://doi.org/10.1016/j.neuron.2017.09.037

Liu, S., Hoess, P., & Ries, J. (2022). Super-Resolution Microscopy for Structural Cell Biology. *Annual Review of Biophysics*, *51*(1), 301–326. https://doi.org/10.1146/annurev-biophys-102521-112912

Louail, A., Sierksma, M. C., Chaffiol, A., Baudet, S., Assali, A., Couvet, S., Nedjam, M., Roche, F., Zagar, Y., Duebel, J., & Nicol, X. (2020). cAMP-Dependent Co-stabilization of Axonal Arbors from Adjacent Developing Neurons. *Cell Reports*, *33*(1), 108220. https://doi.org/10.1016/J.CELREP.2020.108220

Lu, H. C., Butts, D. A., Kaeser, P. S., She, W. C., Janz, R., & Crair, M. C. (2006). Role of Efficient Neurotransmitter Release in Barrel Map Development. *Journal of Neuroscience*, *26*(10), 2692–2703. https://doi.org/10.1523/JNEUROSCI.3956-05.2006

Mel, B. W., Schiller, J., & Poirazi, P. (2017). Synaptic plasticity in dendrites: complications and coping strategies. *Current Opinion in Neurobiology*, *43*, 177–186. https://doi.org/10.1016/j.conb.2017.03.012

Mieda, M., Ono, D., Hasegawa, E., Okamoto, H., Honma, K. ichi, Honma, S., & Sakurai, T. (2015). Cellular Clocks in AVP Neurons of the SCN Are Critical for Interneuronal Coupling Regulating Circadian Behavior Rhythm. *Neuron*, *85*(5), 1103–1116. https://doi.org/10.1016/J.NEURON.2015.02.005

Miller, K. D., Abbott, L. F., & Song, S. (2000). Competitive Hebbian learning through spike-timing-dependent synaptic plasticity. *Nature Neuroscience*, *3*, 919–926. http://neurosci.nature.com

Minehart, J. A., & Speer, C. M. (2021). A Picture Worth a Thousand Molecules—Integrative Technologies for Mapping Subcellular Molecular Organization and Plasticity in Developing Circuits. *Frontiers in Synaptic Neuroscience*, *12*(January), 1–29. https://doi.org/10.3389/fnsyn.2020.615059

Monavarfeshani, A., Stanton, G., Van Name, J., Su, K., Mills, W. A., Swilling, K., Kerr, A., Huebschman, N. A., Su, J., & Fox, M. A. (2018). LRRTM1 underlies synaptic convergence in visual thalamus. *ELife*, *7*. https://doi.org/10.7554/eLife.33498

Mooney, R. D., Shi, M. Y., & Rhoades, R. W. (1994). Modulation of retinotectal transmission by presynaptic 5-HT(1B) receptors in the superior colliculus of the adult hamster. *Journal of Neurophysiology*, *72*(1), 3–13. https://doi.org/10.1152/jn.1994.72.1.3

Morgan, J. L., Berger, D. R., Wetzel, A. W., & Lichtman, J. W. (2016). The Fuzzy Logic of Network Connectivity in Mouse Visual Thalamus. *Cell*, *165*(1), 192–206. https://doi.org/10.1016/j.cell.2016.02.033

Morgan, J. L., Soto, F., Wong, R. O. L., & Kerschensteiner, D. (2011). Development of Cell Type-Specific Connectivity Patterns of Converging Excitatory Axons in the Retina. *Neuron*, *71*(6), 1014–1021. https://doi.org/10.1016/j.neuron.2011.08.025

Muir-Robinson, G., Hwang, B. J., & Feller, M. B. (2002). Retinogeniculate axons undergo eye-specific segregation in the absence of eye-specific layers. *Journal of Neuroscience*, *22*(13), 5259–5264. https://doi.org/10.1523/jneurosci.22-13-05259.2002

Müller, J. A., Betzin, J., Santos-Tejedor, J., Mayer, A., Oprişoreanu, A. M., Engholm-Keller, K., Paulußen, I., Gulakova, P., McGovern, T. D., Gschossman, L. J., Schönhense, E., Wark, J. R., Lamprecht, A., Becker, A. J., Waardenberg, A. J., Graham, M. E., Dietrich, D., & Schoch, S. (2022). A presynaptic phosphosignaling hub for lasting homeostatic plasticity. *Cell Reports*, *39*(3). https://doi.org/10.1016/j.celrep.2022.110696

Munz, M., Gobert, D., Schohl, A., Poquerusse, J., Podgorski, K., Spratt, P., & Ruthazer, E. S. (2014). Rapid hebbian axonal remodeling mediated by visual stimulation. *Science*, *344*(6186), 904–909. https://doi.org/10.1126/science.1251593

Nicol, X., Muzerelle, A., Rio, J. P., Métin, C., & Gaspar, P. (2006). Requirement of Adenylate Cyclase 1 for the Ephrin-A5-Dependent Retraction of Exuberant Retinal Axons. *Journal of Neuroscience*, *26*(3), 862–872. https://doi.org/10.1523/JNEUROSCI.3385-05.2006

Niculescu, D., Michaelsen-Preusse, K., Güner, Ü., van Dorland, R., Wierenga, C. J., & Lohmann, C. (2018). A BDNF-Mediated Push-Pull Plasticity Mechanism for Synaptic Clustering. *Cell Reports*, *24*(8), 2063–2074. https://doi.org/10.1016/j.celrep.2018.07.073

Panda, S., Sato, T. K., Castrucci, A. M., Rollag, M. D., DeGrip, W. J., Hogenesch, J. B., Provencio, I., & Kay, S. A. (2002). Melanopsin (Opn4) requirement for normal light-induced circadian phase shifting. *Science*, *298*(5601), 2213–2216. https://doi.org/10.1126/science.1076848

Penn, A. A., Riquelme, P. A., Feller, M. B., & Shatz, C. J. (1998). Competition in retinogeniculate patterning driven by spontaneous activity. *Science*, *279*(5359), 2108–2112. https://doi.org/10.1126/science.279.5359.2108

Pfeiffenberger, C., Cutforth, T., Woods, G., Yamada, J., Rentería, R. C., Copenhagen, D. R., Flanagan, J. G., & Feldheim, D. A. (2005). Ephrin-As and neural activity are required for eye-specific patterning during retinogeniculate mapping. *Nature Neuroscience*, *8*(8), 1022–1027. https://doi.org/10.1038/nn1508

Pham, T. A., Rubenstein, J. L. R., Silva, A. J., Storm, D. R., & Stryker, M. P. (2001). The CRE/CREB pathway is transiently expressed in thalamic circuit development and contributes to refinement of retinogeniculate axons. *Neuron*, *31*(3), 409–420. https://doi.org/10.1016/S0896-6273(01)00381-6

Poirazi, P., & Mel, B. W. (2001). Impact of active dendrites and structural plasticity on the memory capacity of neural tissue. *Neuron*, *29*(3), 779–796. http://www.ncbi.nlm.nih.gov/pubmed/11301036

Porcu, A., Nilsson, A., Booreddy, S., Barnes, S. A., Welsh, D. K., & Dulcis, D. (2022). Seasonal changes in day length induce multisynaptic neurotransmitter switching to regulate hypothalamic network activity and behavior. *Science Advances*, *8*(35). https://doi.org/10.1126/sciadv.abn9867

Pulikkottil, V. V., Somashekar, B. P., & Bhalla, U. S. (2021). Computation, wiring, and plasticity in synaptic clusters. *Current Opinion in Neurobiology*, *70*, 101–112. https://doi.org/10.1016/j.conb.2021.08.001

Rahman, T. N., Munz, M., Kutsarova, E., Bilash, O. M., & Ruthazer, E. S. (2020). Stentian structural plasticity in the developing visual system. *Proceedings of the National Academy of Sciences*, *117*(20), 10636–10638. https://doi.org/10.1073/pnas.2001107117

Rall, W. (1962). Electrophysiology of a Dendritic Neuron Model. *Biophysical Journal*, *2*(2), 145–167. https://doi.org/10.1016/S0006-3495(62)86953-7

Ravary, A., Muzerelle, A., Hervé, D., Pascoli, V., Ba-Charvet, K. N., Girault, J. A., Welker, E., & Gaspar, P. (2003). Adenylate Cyclase 1 as a Key Actor in the Refinement of Retinal Projection Maps. *Journal of Neuroscience*, *23*(6), 2228–2238. https://doi.org/10.1523/JNEUROSCI.23-06-02228.2003

Rebsam, A., Bhansali, P., & Mason, C. A. (2012). Eye-Specific Projections of Retinogeniculate Axons Are Altered in Albino Mice. *Journal of Neuroscience*, *32*(14), 4821–4826. https://doi.org/10.1523/JNEUROSCI.5050-11.2012

Rebsam, A., Petros, T. J., & Mason, C. A. (2009). Switching retinogeniculate axon laterality leads to normal targeting but abnormal eye-specific segregation that is activity dependent. *Journal of Neuroscience*, *29*(47), 14855–14863. https://doi.org/10.1523/JNEUROSCI.3462-09.2009

Reese, B. E. (1988). "Hidden lamination" in the dorsal lateral geniculate nucleus: the functional organization of this thalamic region in the rat. *Brain Research*, *472*(2), 119–137. https://doi.org/10.1016/0165-0173(88)90017-3

Rey, S., Marra, V., Smith, C., & Staras, K. (2020). Nanoscale Remodeling of Functional Synaptic Vesicle Pools in Hebbian Plasticity. *Cell Reports*, *30*(6), 2006-2017.e3. https://doi.org/10.1016/J.CELREP.2020.01.051

Rizalar, F. S., Roosen, D. A., & Haucke, V. (2021). A Presynaptic Perspective on Transport and Assembly Mechanisms for Synapse Formation. *Neuron*, *109*(1), 27–41. https://doi.org/10.1016/J.NEURON.2020.09.038

Rompani, S. B., Müllner, F. E., Wanner, A., Zhang, C., Roth, C. N., Yonehara, K., & Roska, B. (2017). Different Modes of Visual Integration in the Lateral Geniculate Nucleus Revealed by Single-Cell-Initiated Transsynaptic Tracing. *Neuron*, *93*(4), 767-776.e6. https://doi.org/10.1016/j.neuron.2017.01.028

Rossi, F. M., Pizzorusso, T., Porciatti, V., Marubio, L. M., Maffei, L., & Changeux, J. P. (2001). Requirement of the nicotinic acetylcholine receptor β2 subunit for the anatomical and functional development of the visual system. *Proceedings of the National Academy of Sciences of the United States of America*, *98*(11), 6453–6458. https://doi.org/10.1073/pnas.101120998

Ruby, N. F., Brennan, T. J., Xie, X., Cao, V., Franken, P., Heller, H. C., & O'Hara, B. F. (2002). Role of melanopsin in circadian responses to light. *Science*, *298*(5601), 2211–2213. https://doi.org/10.1126/science.1076701

Ruthazer, E. S., Akerman, C. J., & Cline, H. T. (2003). Control of axon branch dynamics by correlated activity in vivo. *Science*, *301*(5629), 66–70. https://doi.org/10.1126/science.1082545

Ruthazer, E. S., Li, J., & Cline, H. T. (2006). Stabilization of axon branch dynamics by synaptic maturation. *Journal of Neuroscience*, *26*(13), 3594–3603. https://doi.org/10.1523/JNEUROSCI.0069-06.2006

Salichon, N., Gaspar, P., Upton, A. L., Picaud, S., Hanoun, N., Hamon, M., De Maeyer, E., Murphy, D. L., Mössner, R., Lesch, K. P., Hen, R., & Seif, I. (2001). Excessive activation of serotonin (5-HT) 1B receptors disrupts the formation of sensory maps in monoamine oxidase A and 5-HT transporter knock-out mice. *Journal of Neuroscience*, *21*(3), 884–896. https://doi.org/10.1523/jneurosci.21-03-00884.2001

Sanes, J. R., & Lichtman, J. W. (1999). DEVELOPMENT OF THE VERTEBRATE NEUROMUSCULAR JUNCTION. *Annual Review of Neuroscience*, *22*(1), 389–442. https://doi.org/10.1146/annurev.neuro.22.1.389

Schafer, D. P., Lehrman, E. K., Kautzman, A. G., Koyama, R., Mardinly, A. R., Yamasaki, R., Ransohoff, R. M., Greenberg, M. E., Barres, B. A., & Stevens, B. (2012). Microglia Sculpt Postnatal Neural Circuits in an Activity and Complement-Dependent Manner. *Neuron*, *74*(4), 691–705. https://doi.org/10.1016/j.neuron.2012.03.026

Schueder, F., Unterauer, E. M., Ganji, M., & Jungmann, R. (2020). DNA-Barcoded Fluorescence Microscopy for Spatial Omics. *PROTEOMICS*, *20*(23), 1900368. https://doi.org/10.1002/pmic.201900368

Shah, R. D., & Crair, M. C. (2008). Retinocollicular synapse maturation and plasticity are regulated by correlated retinal waves. *Journal of Neuroscience*, *28*(1), 292–303. https://doi.org/10.1523/JNEUROSCI.4276-07.2008

Shan, Y., Abel, J. H., Li, Y., Izumo, M., Cox, K. H., Jeong, B., Yoo, S.-H., Olson, D. P., Doyle, F. J., & Takahashi, J. S. (2020). Dual-Color Single-Cell Imaging of the Suprachiasmatic Nucleus Reveals a Circadian Role in Network Synchrony. *Neuron*, *108*(1), 164-179.e7. https://doi.org/10.1016/j.neuron.2020.07.012

Shatz, C. J. (1990). Competitive interactions between retinal ganglion cells during prenatal development. *Journal of Neurobiology*, *21*(1), 197–211. https://doi.org/10.1002/NEU.480210113

Shatz, C. J., & Stryker, M. P. (1988). Prenatal tetrodotoxin infusion blocks segregation of retinogeniculate afferents. *Science*, *242*(4875), 87–89. https://doi.org/10.1126/science.3175636

Sigal, Y. M., Speer, C. M., Babcock, H. P., & Zhuang, X. (2015). Mapping Synaptic Input Fields of Neurons with Super-Resolution Imaging. *Cell*, *163*(2), 493–505. https://doi.org/10.1016/J.CELL.2015.08.033

Speer, C. M., Sun, C., Liets, L. C., Stafford, B. K., Chapman, B., & Cheng, H. J. (2014). Eye-specific retinogeniculate segregation proceeds normally following disruption of patterned spontaneous retinal activity. *Neural Development*, *9*(1), 1–19. https://doi.org/10.1186/1749-8104-9-25

Sretavan, D., & Shatz, C. J. (1984). Prenatal development of individual retinogeniculate axons during the period of segregation. *Nature*, *308*(5962), 845–848. https://doi.org/10.1038/308845a0

Sretavan, D. W., & Shatz, C. J. (1986a). Prenatal development of cat retinogeniculate axon arbors in the absence of binocular interactions. *Journal of Neuroscience*, *6*(4), 990–1003. https://doi.org/10.1523/jneurosci.06-04-00990.1986

Sretavan, D. W., & Shatz, C. J. (1986b). Prenatal development of retinal ganglion cell axons: Segregation into eye-specific layers within the cat's lateral geniculate nucleus. *Journal of Neuroscience*, *6*(1), 234–251. https://doi.org/10.1523/jneurosci.06-01-00234.1986

Sretavan, D. W., & Shatz, C. J. (1987). Axon trajectories and pattern of terminal arborization during the prenatal development of the cat's retinogeniculate pathway. *Journal of Comparative Neurology*, *255*(3), 386–400. https://doi.org/10.1002/cne.902550306

Stafford, B. K., Sher, A., Litke, A. M., & Feldheim, D. A. (2009). Spatial-Temporal Patterns of Retinal Waves Underlying Activity-Dependent Refinement of Retinofugal Projections. *Neuron*, *64*(2), 200–212. https://doi.org/10.1016/J.NEURON.2009.09.021

Stellwagen, D., & Shatz, C. J. (2002). An instructive role for retinal waves in the development of retinogeniculate connectivity. *Neuron*, *33*(3), 357–367. https://doi.org/10.1016/S0896-6273(02)00577-9

Stellwagen, D., Shatz, C. J., & Fellert, M. B. (1999). Dynamics of retinal waves are controlled by cyclic AMP. *Neuron*, *24*(3), 673–685. https://doi.org/10.1016/S0896-6273(00)81121-6

Stevens, B., Allen, N. J., Vazquez, L. E., Howell, G. R., Christopherson, K. S., Nouri, N., Micheva, K. D., Mehalow, A. K., Huberman, A. D., Stafford, B., Sher, A., Litke, A. M. M., Lambris, J. D., Smith, S. J., John, S. W. M., & Barres, B. A. (2007). The Classical Complement Cascade Mediates CNS Synapse Elimination. *Cell*, *131*(6), 1164–1178. https://doi.org/10.1016/j.cell.2007.10.036

Sun, C., Warland, D. K., Ballesteros, J. M., Van Der List, D., & Chalupa, L. M. (2008). Retinal waves in mice lacking the β2 subunit of the nicotinic acetylcholine receptor. *Proceedings of the National Academy of Sciences of the United States of America*, *105*(36), 13638–13643. https://doi.org/10.1073/PNAS.0807178105/SUPPL_FILE/0807178105SI.PDF

Sun, S. Y., Li, X. W., Cao, R., Zhao, Y., Sheng, N., & Tang, A. H. (2022). Correlative Assembly of Subsynaptic Nanoscale Organizations During Development. *Frontiers in Synaptic Neuroscience*, *14*, 16. https://doi.org/10.3389/FNSYN.2022.748184/BIBTEX

Suzuki, A., Lee, L. J., Hayashi, Y., Muglia, L., Itohara, S., Erzurumlu, R. S., & Iwasato, T. (2015). Thalamic adenylyl cyclase 1 is required for barrel formation in the somatosensory cortex. *Neuroscience*, *290*, 518–529. https://doi.org/10.1016/J.NEUROSCIENCE.2015.01.043

Tan, C., Wang, S. S. H., de Nola, G., & Kaeser, P. S. (2022). Rebuilding essential active zone functions within a synapse. *Neuron*, *110*(9), 1498-1515.e8. https://doi.org/10.1016/J.NEURON.2022.01.026

Tang, A. H., Chen, H., Li, T. P., Metzbower, S. R., MacGillavry, H. D., & Blanpied, T. A. (2016). A trans-synaptic nanocolumn aligns neurotransmitter release to receptors. *Nature*, *536*(7615), 210–214. https://doi.org/10.1038/nature19058

Tiriac, A., Smith, B. E., & Feller, M. B. (2018). Light Prior to Eye Opening Promotes Retinal Waves and Eye-Specific Segregation. *Neuron*, *100*(5), 1059-1065.e4. https://doi.org/10.1016/j.neuron.2018.10.011

Toledo, R., Aguilar-Roblero, R., Canchola, E., & Caba, M. (2005). Circadian and photic-induced expression of Fos protein in the suprachiasmatic nucleus of the rabbit. *Biological Rhythm Research*, *36*(1–2), 47–55. https://doi.org/10.1080/09291010400028542

Truckenbrodt, S., Viplav, A., Jähne, S., Vogts, A., Denker, A., Wildhagen, H., Fornasiero, E. F., & Rizzoli, S. O. (2018). Newly produced synaptic vesicle proteins are preferentially used in synaptic transmission. *The EMBO Journal*, *37*(15). https://doi.org/10.15252/EMBJ.201798044

Tufford, A. R., Onyak, J. R., Sondereker, K. B., Lucas, J. A., Earley, A. M., Mattar, P., Hattar, S., Schmidt, T. M., Renna, J. M., & Cayouette, M. (2018). Melanopsin Retinal Ganglion

Cells Regulate Cone Photoreceptor Lamination in the Mouse Retina. *Cell Reports*, *23*(8), 2416–2428. https://doi.org/10.1016/j.celrep.2018.04.086

Upton, A. L., Salichon, N., Lebrand, C., Ravary, A., Blakely, R., Seif, I., & Gaspar, P. (1999). Excess of serotonin (5-HT) alters the segregation of ispilateral and contralateral retinal projections in monoamine oxidase a knockout mice: Possible role of 5-HT uptake in retinal ganglion cells during development. *Journal of Neuroscience*, *19*(16), 7007–7024. https://doi.org/10.1523/jneurosci.19-16-07007.1999

Vatan, T., Minehart, J. A., Zhang, C., Agarwal, V., Yang, J., & Speer, C. M. (2021). Volumetric super-resolution imaging by serial ultrasectioning and stochastic optical reconstruction microscopy in mouse neural tissue. *STAR Protocols*, *2*(4), 100971. https://doi.org/10.1016/j.xpro.2021.100971

Vaughn, J. E. (1989). Fine structure of synaptogenesis in the vertebrate central nervous system. *Synapse*, *3*(3), 255–285. https://doi.org/10.1002/SYN.890030312

Voronin, L. L., & Cherubini, E. (2004). "Deaf, mute and whispering" silent synapses: Their role in synaptic plasticity. In *Journal of Physiology* (Vol. 557, Issue 1, pp. 3–12). John Wiley & Sons, Ltd. https://doi.org/10.1113/jphysiol.2003.058966

Wilton, D. K., Dissing-Olesen, L., & Stevens, B. (2019). Neuron-Glia Signaling in Synapse Elimination. *Annual Review of Neuroscience*, *42*, 107–127. https://doi.org/10.1146/annurev-neuro-070918-050306

Winnubst, J., Cheyne, J. E., Niculescu, D., & Lohmann, C. (2015). Spontaneous Activity Drives Local Synaptic Plasticity InVivo. *Neuron*, *87*(2), 399–410. https://doi.org/10.1016/j.neuron.2015.06.029

Winnubst, J., & Lohmann, C. (2012). Synaptic clustering during development and learning: The why, when, and how. *Frontiers in Molecular Neuroscience*, *5*(MAY 2012), 1–9. https://doi.org/10.3389/fnmol.2012.00070

Wu, G. Y., Deisseroth, K., & Tsien, R. W. (2001). Spaced stimuli stabilize MAPK pathway activation and its effects on dendritic morphology. *Nature Neuroscience*, *4*(2), 151–158. https://doi.org/10.1038/83976

Wyatt, R. M., & Balice-Gordon, R. J. (2003). Activity-dependent elimination of neuromuscular synapses. *Journal of Neurocytology*, *32*(5–8), 777–794. https://doi.org/10.1023/B:NEUR.0000020623.62043.33

Xu, H. P., Burbridge, T. J., Chen, M. G., Ge, X., Zhang, Y., Zhou, Z. J., & Crair, M. C. (2015). Spatial pattern of spontaneous retinal waves instructs retinotopic map refinement more than activity frequency. *Developmental Neurobiology*, *75*(6), 621–640. https://doi.org/10.1002/dneu.22288

Xu, H. P., Burbridge, T. J., Ye, M., Chen, M., Ge, X., Zhou, Z. J., & Crair, M. C. (2016). Retinal wave patterns are governed by mutual excitation among starburst amacrine cells and drive the refinement and maintenance of visual circuits. *Journal of Neuroscience*, *36*(13), 3871–3886. https://doi.org/10.1523/JNEUROSCI.3549-15.2016

Xu, H. ping, Furman, M., Mineur, Y. S., Chen, H., King, S. L., Zenisek, D., Zhou, Z. J., Butts, D. A., Tian, N., Picciotto, M. R., & Crair, M. C. (2011). An Instructive Role for Patterned Spontaneous Retinal Activity in Mouse Visual Map Development. *Neuron*, *70*(6), 1115–1127. https://doi.org/10.1016/j.neuron.2011.04.028

Yasuda, M., Nagappan-Chettiar, S., Johnson-Venkatesh, E. M., & Umemori, H. (2021). An activity-dependent determinant of synapse elimination in the mammalian brain. *Neuron*, *109*(8), 1333-1349.e6. https://doi.org/10.1016/j.neuron.2021.03.006

Zhang, C., Atasoy, D., Arac, D., Yang, X., Fucillo, M. V, Robinson, A. J., Ko, J., Brunger, A. T., & C, S. T. (2011). Neurexins physically and functionally interact with GABA-A receptors. *Neuron*. https://doi.org/10.1016/j.neuron.2010.04.008.Neurexins

Zhang, C., Yadav, S., & Speer, C. M. (2023). The synaptic basis of activity-dependent eye-specific competition. *Cell Reports*, *42*(2), 112085. https://doi.org/10.1016/j.celrep.2023.112085

Zhang, J., Ackman, J. B., Xu, H. P., & Crair, M. C. (2012). Visual map development depends on the temporal pattern of binocular activity in mice. *Nature Neuroscience*, *15*(2), 298–307. https://doi.org/10.1038/nn.3007

Zhang, L. I., Tao, H. W., Holt, C. E., Harris, W. A., & Poo, M. M. (1998). A critical window for cooperation and competition among developing retinotectal synapses. *Nature*, *395*(6697), 37–44. https://doi.org/10.1038/25665